McGill University

Doctoral Thesis

Sifting molecular noise with image correlation methods to measure transport and photophysical dynamics

---

Author:
Simon Sehayek

Supervisor:
Prof. Paul W. Wiseman

August 2021

A thesis submitted to McGill University in partial fulfillment of the requirements of the degree of Doctor of Philosophy

Department of Physics

This page was almost intentionally left blank.

Acknowledgements

I would like to sincerely thank Paul Wiseman for supervising me during my graduate studies. His kindness, patience, passion and knowledge of the field made the experience a true pleasure. I especially appreciated the freedom he granted me to explore my ideas and pursue more theoretical projects. Paul has always known how to let the good times roll and that is just what I needed throughout these dire straits. So long, and thanks for all the fish, Paul.

I would also like to thank all the wonderful members in the Wiseman lab who temporally coincided with my studies (yes, there are many). I am particularly grateful to Hugo Brandão for showing me the ropes when I first joined the lab. His initial guidance has been invaluable throughout my studies.

More thanks go out to the coworkers in my office, who couldn't stand me any more and moved to British Columbia. I would specifically like to thank Cindy Shaheen and Daniel Berard for all the useful research discussions. I will miss all the good times we shared along with the rest of the office.

I am also thankful to Prof. Paul François for guiding me when I was stuck with my research. Moreover, I greatly appreciate him and Jack Sankey for being on my PhD advisory committee and for offering excellent suggestions for advancing the project presented in Chapter 2.

I would further like to extend my thanks to Yasser Gidi, Viktorija Glembockyte, Hugo Brandão, Prof. Paul François and Gonzalo Cosa for their contributions to the project presented in Chapter 2, and Xiyu Yi and Shimon Weiss for their contributions to the project presented in Chapter 3. Many thanks again to Paul Wiseman for his contributions, as well.

Furthermore, I am grateful for the close friends I made throughout my studies at McGill. Simon, Pericles, Alessandro and Carlos, I'm glad we shared this experience together. Special thanks also to my longtime friends Jesse, Jon and Ben.

Lastly, I would like to express my infinite gratitude to my parents, Aaron and Rachel, and brother, Daniel, for always supporting me. This work would not have been possible without you and I am very lucky to have you. I love you all so much.

—In memory of my grandmother, Mama, great grandfather, Shimon, and grandfathers, Shimon and Judah

Statement of Originality

I, Simon Sehayek, claim that the following elements of this thesis are distinct contributions to original knowledge and are considered to be original scholarship:

- An image correlation method for simultaneously measuring photophysical emission blinking and bleaching rates of immobile fluorophores. The method is also capable of measuring these rates faster than the camera detector integration time. [Published: Sehayek, S. *et al. ACS Nano*, **13**, 10, 11955–11966, Manuscript]
- An image correlation method for simultaneously measuring diffusion rate, photophysical emission blinking rates, and fraction of diffusing particles. [Published: Sehayek, S. *et al. Biophys. Rep.*, **1**, 2, 100015, Manuscript]

Contribution of Co-authors

This is a manuscript based thesis with two published works.
Chapter 2 is based on the following published manuscript:[1]

A High-Throughput Image Correlation Method for Rapid Analysis of Fluorophore Photoblinking and Photobleaching Rates Sehayek, S., Gidi, Y., Glembockyte, V., Brandão, H.B., François, P., Cosa, G., and Wiseman, P.W. *ACS Nano*, **13**, 10, 11955–11966 (2019)

I developed the theory and simulations for this manuscript (except those generated by TestSTORM[2]). I also did the autocorrelation and the MLE analyses. Y. Gidi provided the STORM data and V. Glembockyte provided the Cy5-DNA with nickel-ion data. Y. Gidi also performed the single-molecule analysis. Y. Gidi, V. Glembockyte and G. Cosa provided insight into the photophysical mechanisms of Cy5. H.B. Brandão and P. François provided insight for the theory and reviewed the paper. G. Cosa and P.W. Wiseman assisted in writing the manuscript and supervised the project.

Chapter 3 is based on the following published manuscript:[3]

Rapid Ensemble Measurement of Protein Diffusion and Probe Blinking Dynamics in Cells Sehayek, S., Yi, X., Weiss, S., and Wiseman, P.W. *Biophys. Rep.*, **1**, 2, 100015 (2021)

I developed the theory and simulations for this manuscript. I also did the autocorrelation analyses. X. Yi provided the experimental data. X. Yi also performed the SOFI analysis and provided insight for the theory. X. Yi and S. Weiss reviewed the paper. P.W. Wiseman assisted in writing the manuscript and supervised the project.

Abstract

Fluorescence microscopy is the most frequently used microscopy tool for studying live cells. Furthermore, with the recent advent of super-resolution microscopy (SRM), one can now circumvent the diffraction barrier imposed by traditional optical microscopes and achieve resolutions of $\sim$ 10 nm. One class of SRM techniques, dubbed single-molecule localization microscopy (SMLM), takes advantage of the photoblinking of fluorescent probes. Photoblinking effectively switches probes between fluorescent "on"- and "off"-states. Many different SRM methods exist, but so far, they need to be adapted on a case-by-case basis to be properly applied, for example, by choosing different fluorescent labels. It is, therefore, important to develop optimal probes and measurement conditions to tune the photoblinking to achieve the highest spatial resolutions. Furthermore, most SRM studies have so far focused on obtaining static information from biological systems through extracting super-resolved images, but have not complemented those results with measurements of the dynamics.

In this thesis, we present two image correlation methods we developed to address these issues. Fluorescence and image correlation techniques are rapid to implement and widely used for measuring dynamics and other parameters of interest in the field of biophysics.

We begin by introducing the basic concepts of fluorescence microscopy and then discuss various SRM methods, followed by a basic overview of fluorescence correlation spectroscopy (FCS) and image correlation spectroscopy (ICS). In Chapter 2, we present an image correlation method capable of rapidly measuring photoblinking rates of fluorescent probes, including rates that are faster than the camera detector exposure time. We further show that attempting to employ the standard single-molecule approach for measuring these faster rates leads to aliasing. We confirm this through analysis of simulations and DNA-Cy5 duplexes immobilized on glass coverslips. The high-throughput nature of our technique can allow for future optimal probe screening for SMLM application.

In Chapter 3, we introduce another image correlation technique for measuring diffusion coefficients, photoblinking rates and fraction of diffusing particles. Unlike other image correlation techniques, this method can be applied in regions of non-uniformly distributed immobile particles in space that are subject to photoblinking. This can be especially useful for measuring the dynamics in complex cellular structures that are studied by

SMLM methods. We demonstrate our method on simulations and Dronpa-C12 labeled beta-actin in live 3T3/NIH and HeLa cells. Our measured diffusion coefficients were consistent with previously reported values of G-actin in the cytoplasm. The measured photoblinking rates also followed the expected trend with varying excitation power in the HeLa cell data.

Résumé

La microscopie à fluorescence est l'outil de microscopie le plus fréquemment utilisé pour étudier les cellules vivantes. De plus, avec l'avènement récent de la microscopie à super-résolution (SRM), il est désormais possible de contourner la barrière de diffraction imposée par les microscopes optiques traditionnels et d'atteindre des résolutions de ~ 10 nm. Une classe de techniques SRM, appelée «single-molecule localization microscopy» (SMLM), tire parti du photoclignotement des sondes fluorescentes, ce qui les fait basculer efficacement entre les états fluorescents «actifs» et «inactifs». De nombreuses méthodes SRM différentes existent, mais jusqu'à présent, elles doivent être adaptées au cas par cas pour être correctement appliquées, par exemple en choisissant différents marqueurs fluorescents. Il est donc important de développer des sondes et des conditions de mesure optimales pour régler le photoclignotement afin d'atteindre les résolutions spatiales les plus élevées. En outre, la plupart des études SRM se sont jusqu'à présent concentrées sur l'obtention d'informations statiques à partir de systèmes biologiques en extrayant des images super-résolues, mais n'ont pas complété ces résultats par des mesures de la dynamique.

Dans cette thèse, nous présentons deux méthodes de corrélation d'images que nous avons développées pour résoudre ces problèmes. Les techniques de fluorescence et de corrélation d'images sont rapides à mettre en œuvre et largement utilisées pour mesurer la dynamique et d'autres paramètres d'intérêt dans le domaine de la biophysique.

Nous commençons par introduire les concepts de base de la microscopie à fluorescence, puis discutons de diverses méthodes SRM, suivies d'un aperçu de base de la spectroscopie de corrélation de fluorescence (FCS) et de la spectroscopie de corrélation d'images (ICS). Dans le chapitre 2, nous présentons une méthode de corrélation d'images capable de mesurer rapidement les taux de photoclignotement des sondes fluorescentes, y compris les taux qui sont plus rapides que le temps d'exposition du détecteur de la caméra. Nous montrons en outre que tenter d'employer l'approche standard à molécule unique pour mesurer ces taux plus rapides conduit au repliement de spectre, et l'avons confirmé par l'analyse de simulations et de duplex ADN-Cy5 immobilisés sur des lamelles de verre. La nature à haut débit de notre technique peut permettre un futur criblage de sonde optimal pour l'application SMLM.

Dans le chapitre 3, nous introduisons une autre technique de corrélation d'images pour mesurer les coefficients de diffusion, les taux de photoclignotement et la fraction de particules diffusantes. Contrairement à d'autres techniques de corrélation d'images, cette méthode peut être appliquée dans des régions de particules immobiles réparties de manière non uniforme dans l'espace qui sont sujettes au photoclignotement. Cela peut être particulièrement utile pour mesurer la dynamique dans les structures cellulaires complexes qui sont étudiées par les méthodes SMLM. Nous démontrons notre méthode sur des simulations et la bêta-actine marquée par Dronpa-C12 dans des cellules vivantes 3T3/NIH et HeLa. Nos coefficients de diffusion mesurés sont cohérents avec les valeurs précédemment rapportées de la G-actine dans le cytoplasme. Nous montrons également que les taux de photoclignotement mesurés suivent la tendance attendue avec une puissance d'excitation variable dans les données de la cellule HeLa.

Contents

List of Figures

List of Tables

List of Commonly Used Abbreviations

ACF	**A**uto**C**orrelation **F**unction
(EM)CCD	(**E**lectron **M**ultiplication) **C**harge-**C**oupled **D**evices
(s)CMOS	(**s**cientific) **C**omplementary **M**etal **O**xide **S**emiconductor
(S)FCS	(**S**canning) **F**luorescence **C**orrelation **S**pectroscopy
FRET	**F**örster **R**esonance **E**nergy **T**ransfer
(k/R/[S]T)I{C}CS	(***k***-space/**R**aster/[**S**patio]**T**emporal) **I**mage {**C**ross-}**C**orrelation **S**pectroscopy
LS(C)M	**L**aser-**S**canning (**C**onfocal) **M**icroscope
MLE	**M**aximum **L**ikelihood **E**stimation
(f)PALM	(**f**luorescent) **P**hoto**A**ctivation **L**ocalization **M**icroscopy
PSF	**P**oint **S**pread **F**unction
ROI	**R**egion **O**f **I**nterest
SMLM	**S**ingle-**M**olecule **L**ocalization **M**icroscopy
SNR	**S**ignal-to-**N**oise **R**atio
(b)SOFI	(**b**alanced) **S**uper-resolution **O**ptical **F**luctuation **I**maging
SPT	**S**ingle-**P**article **T**racking
SRM	**S**uper-**R**esolution **M**icroscopy
STED	**ST**imulated **E**mission-**D**epletion
(d)STORM	(**d**irect) **S**tochastic **O**ptical **R**econstruction **M**icroscopy
TIRFM	**T**otal **I**nternal **R**eflection **F**luorescence **M**icroscope
TOI	**T**ime **O**f **I**nterest

Chapter 1

Introduction

Fluorescence microscopy is the most commonly used microscopy tool for studying live cells. Optical super-resolution microscopy (SRM), the development of which was recently awarded the 2014 Nobel prize in chemistry, has allowed researchers to study these systems using fluorescence microscopy at spatial resolutions exceeding those imposed by the light diffraction limit on traditional optical microscopes (see [4, 5]). This has led to many advances in the study of cell biology, cellular biophysics, neuroscience and other fields (see [6–11]).

There is additional molecular information inherent in fluorescence microscopy images and a plethora of analysis techniques have been developed to analyze such images. Fluorescence fluctuation/correlation methods are one family of techniques that usually involve computing the correlation function of fluorescence fluctuations to measure quantities of interest using ensemble statistics. The first technique of its kind was fluorescence correlation spectroscopy (FCS),[12–14] which measures the fluorescence fluctuations in time excited within a laser beam focal volume of a femtoliter or smaller. FCS is well-known for measuring particle densities, transport parameters, and chemical kinetics.

Assuming the system measured is ergodic, an analogous technique known as image correlation spectroscopy (ICS)[15] was later developed that measured the fluorescence fluctuations in space rather than time and computed particle density information from the correlation of these spatial fluctuations. Other ICS techniques were later developed that considered fluorescence fluctuations in both space and time, albeit with lower temporal resolution than associated with FCS (see [16]).

Another group of techniques used for analyzing fluorescence microscopy data relies on single-particle tracking (SPT). SPT usually consists of localizing single molecules and then following them over time to determine parameters of interest, such as diffusion (see [17, 18]). Since SPT methods analyze particles individually, it can be seen as being more accurate than correlation techniques. However, SPT, being a single-molecule method, is limited to measuring low densities of labeled molecules and can be hindered by other

factors, such as photophysical effects, which can intermittently or permanently prevent a fluorescent label from emitting photons.

In this chapter, we begin by introducing the basics of fluorescence microscopy, followed by a discussion of SRM and fluorescence/image correlation microscopy methods.

1.1 Basics of fluorescence

Fluorescence is one form of a more general molecular emission called luminescence. Fluorescent molecules have the property that their absorption and emission spectra are shifted in wavelength. The physical reason for this shift is the Stokes shift. To illustrate this phenomenon, we make reference to the Jablonski energy diagram depicted in Fig. 1.1. To understand this diagram, consider a fluorophore in its ground singlet electronic state, S_0 (*i.e.* all electrons are paired so that they have antiparallel intrinsic spins). A photon with a suitable wavelength can be absorbed by the fluorophore, which is then usually excited to a higher vibrational level of an excited singlet state. This absorption occurs in around a femtosecond.[19] Before the molecule can relax back down to the ground excited singlet state, it typically undergoes a radiationless energy loss process known as internal conversion, which occurs on the picosecond timescale.[19, 20] Through this process, the excited electron relaxes to the lowest vibrational level of the first excited singlet state, S_1. Conversely, the absorption-fluorescence emission cycle for the excited electron typically occurs on a timescale on the order of 1–10 nanoseconds.[19] Therefore, internal conversion accounts for the typical higher frequency of the absorbed photon, when compared to the emitted one (see Figure 1.1). The red-shifted wavelength of the fluorescence emission is known as the Stokes shift. In practice, larger Stokes shifts are desirable properties of fluorescent labels, so that the incident light on a sample can be easily filtered without affecting the output fluorescence. Fluorescence emission occurs when a photon is emitted in the process of returning to the ground state, which often occurs from the lowest vibrational level of S_1 (Kasha's law).[19] Note that non-radiative processes, such as collisions, can also relax a fluorophore back to S_0 through non-emissive pathways.

A fluorophore in the excited S_1 state can also enter the energetically lower first excited triplet state, T_1, through a spin-flip of the excited electron. This transition is known as an intersystem crossing. Photon emission due to relaxation from T_1 to S_0 is known as phosphorescence. The time taken to decay back to S_0 from T_1 is relatively long (milliseconds to seconds)[19] because the transition is spin-forbidden by selection rules.[21] This effectively causes the fluorophore to stochastically enter a non-emissive "dark-state". Fluorophore switching between on and off emissive states gives rise to a phenomenon

known as photoblinking, which is one of the central topics we examine in this work. Other mechanisms that cause fluorophore blinking also exist and depend on the fluorophore.[22] The energy levels and transitions discussed above are summarized in Figure 1.1.

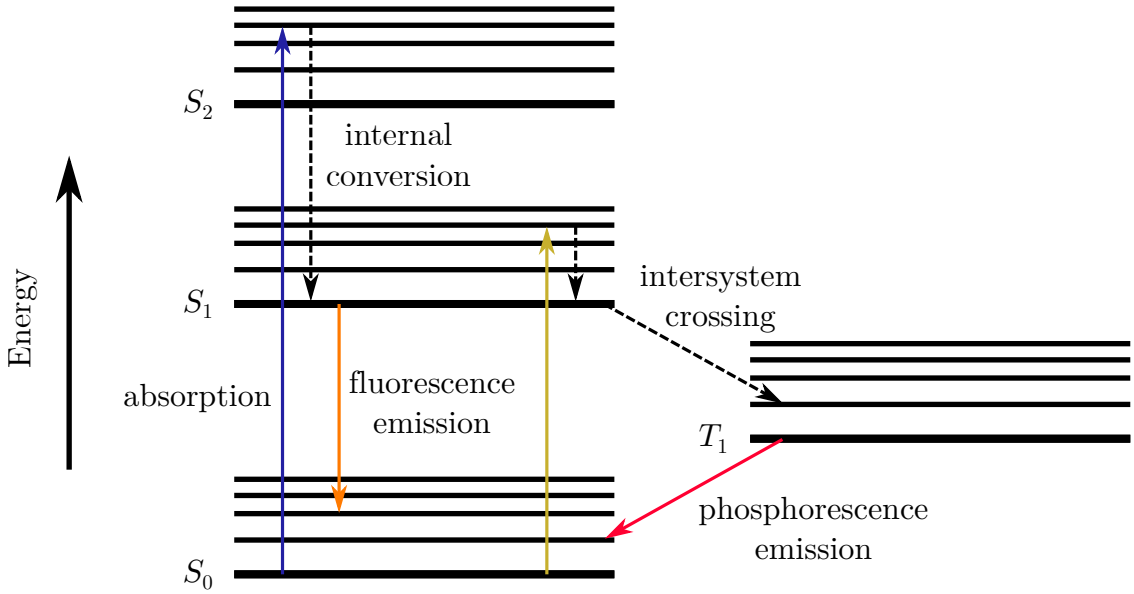

FIGURE 1.1: Simplified Jablonski diagram of a typical fluorophore. Singlet states (thick lines) and their excited vibrational states (thin lines) are shown. Solid arrows represent transitions that involve a photon, while dashed arrows represent non-radiative relaxations. A fluorophore first absorbs a photon of appropriate energy from S_0, which typically causes it to enter a higher vibrational state of an excited singlet state. The excited electron then quickly relaxes to S_1 *via* internal conversion. A photon can then be emitted from $S_1 \rightarrow S_0$, resulting in fluorescence emission. An excited fluorophore in S_1 can also enter T_1 through intersystem crossing. Relaxation back to S_0 is long due to the spin-forbidden nature of the transition, causing the fluorophore to remain in a non-emissive state. Photon emission from $T_1 \rightarrow S_0$ results in phosphorescence.

Fluorophores may also cease to emit *via* a photochemical conversion to a nonfluorescent molecular form known as photobleaching, which is generally considered to be permanent. There are many mechanisms responsible for photobleaching, which usually depend on the fluorophore being used. One principal mechanism involves interactions between a fluorophore in the triplet state and singlet oxygen.[22, 23] Singlet oxygen can be formed when an energy transfer occurs between oxygen and the fluorophore, both occupying the triplet state, resulting in the quenching of the fluorophore (*i.e.* radiationless de-excitation) and excitation of the oxygen to the excited singlet state.[22, 24] Fluorophores are susceptible to such reactions in the triplet state due to its higher energy and longer lifetime. Removing oxygen from a sample can mitigate this effect, but results in longer lived triplet states. This happens because oxygen also quenches fluorophores in

the triplet state.[22] Other triplet quenchers are, however, available for reducing triplet dwell times and, consequently, photobleaching.[22] Photobleaching is also increased when higher excitation intensities are used. This can happen through two-step photolysis, whereby an excited fluorophore in either the singlet or triplet state absorbs a photon to enter a corresponding excited state of a higher order (*i.e.* S_n or T_n for $n > 1$) and then photobleaches.[25] Higher excitation intensities also increase the rate at which a fluorophore enters the triplet state, which can accelerate photobleaching due to interactions with oxygen. Other reaction mechanisms have also been attributed to fluorophore photobleaching.[26]

1.1.1 Fluorescence lifetime and quantum yield

The proportion of emitted fluorescence relative to absorbed photons is known as the quantum yield of a fluorophore, Q_{fl}. This quantity can be characterized by the fluorescence decay rate, k_{fl}, and the sum of the non-radiative decay rates, $\sum_i k^i_{\text{nr}}$, such that,

$$Q_{\text{fl}} \equiv \frac{k_{\text{fl}}}{k_{\text{fl}} + \sum_i k^i_{\text{nr}}}. \tag{1.1}$$

The fluorescence lifetime of a fluorophore is a measure of the mean time it spends in the excited state before it returns to the ground state and is given by:

$$\tau_{\text{fl}} \equiv \frac{1}{k_{\text{fl}} + \sum_i k^i_{\text{nr}}}. \tag{1.2}$$

Note that absorption occurs on a femtosecond timescale, and consequently, is negligible when considering lifetimes. The lifetime is an important quantity in determining the amount of time a fluorophore can react with another molecule (*e.g.* oxygen) in its more reactive excited state. Although in this work we consider the analysis of microscopy images from emitted fluorescence photons, one can also construct images using measured lifetimes as a function of position in the sample. This modality, known as fluorescence lifetime imaging (FLIM), has the advantage of being independent of fluorophore density, brightness and photobleaching (see [27, 28]).

1.2 Fluorescence microscopy

1.2.1 Widefield epi-fluorescence microscope

Biomolecules labeled with fluorescent tags are widely studied using fluorescence microscopy. A schematic of a basic setup for a widefield epi-fluorescence microscope is provided in Figure 1.2. At first, excitation light (laser, LED, or lamp) is filtered by an excitation filter, which transmits the desired wavelength for absorption by a fluorescently labeled sample of interest. The filtered light is subsequently directed toward a dichroic mirror angled at 45 degrees. The dichroic mirror is chosen to reflect the excitation light and transmit fluorescence from the sample. Therefore, the incoming excitation light is reflected off the mirror towards an objective lens, which focuses the light onto the sample of interest.

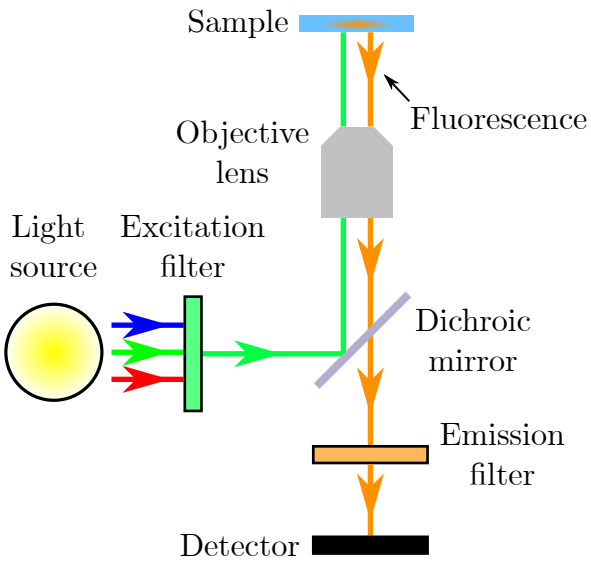

FIGURE 1.2: Basic widefield epi-fluorescence microscope schematic. Filtered excitation light is first reflected by a dichroic mirror and focused onto the sample of interest through an objective lens. Emitted fluorescence is collected back through the objective and transmitted through the dichroic and an emission filter in order to be collected by a detector. Excitation light is filtered out by the dichroic and emission filter.

Fluorescence from the sample is back collected through the same objective lens and transmitted through the dichroic mirror. The transmitted fluorescence is passed through a wavelength specific emission filter and is, finally, collected by an area camera detector. Any excitation light scattered or reflected from the sample back through the objective should not be able to pass through the dichroic mirror; however, any residual excitation light that is transmitted by the mirror is filtered out by an emission filter. The light

source and excitation filter in Figure 1.2 can be replaced with an excitation laser and beam expander to expand the laser light and a tube lens before the detector to focus the collected fluorescence onto it. The configuration where excitation light and fluorescence from the sample are both passed through the objective is known as epi-fluorescence. The epi-fluorescence setup is widely used as it allows for easy separation of fluorescence and excitation light, which can help in enhancing the signal to background ratio.

1.2.2 Spatial resolution: the diffraction limit

In optical microscopy, the diffraction of light from a point source results in a diffraction pattern known as an Airy disk in the focal plane. Particularly, in a fluorescence microscope, the objective lens allows for interference of the emitted fluorescence from the sample, and consequently, leads to the effective blurring of the imaged fluorophores. The intensity of this pattern as a function of space is referred to as the point spread function (PSF) for the microscope or optical imaging system. Therefore, the inherent lateral resolution of a fluorescence microscope, ρ_{Airy}, is limited by the width of the PSF, which can be characterized by the wavelength of the collected light, λ, and the numerical aperture of the objective lens, NA, as:[29]

$$\rho_{\text{Airy}} \simeq 0.61 \times \frac{\lambda}{\text{NA}}. \tag{1.3}$$

Here, we can also write $\text{NA} \equiv n \sin \alpha$, where n is the refractive index of the imaging medium and α is the half-angle that light can be collected from the objective. ρ_{Airy} is also the radius to the first zero of the Airy disk and is also known as the Rayleigh resolution criterion. According to this criterion, if two point sources of light are separated by a distance smaller than ρ_{Airy}, they cannot be resolved as separate fluorescent emitters in the image. Several other resolution criteria are also used when discussing resolution, but they only differ by a scaling factor. The axial resolution is also limited by diffraction, with the axial distance between the center maximum and the first minimum given by:[29]

$$\zeta_{\text{min}} = \frac{2\lambda}{\text{NA}^2}. \tag{1.4}$$

Efforts to decrease ρ_{Airy} and ζ_{min} to obtain better resolutions are rather restrictive. Standard microscope setups with modern liquid-immersion objectives can attain an NA of up to 1.49, although this can be further increased to 1.7 in specific setups.[30] Furthermore, using shorter than visible wavelengths is unfeasible as this would be damaging to live cells. Consequently, a lateral resolution of about 190 nm is the theoretical upper

bound for the resolution limit for visible light (with NA = 1.45), but in practice, fluorescence microscopes have even poorer resolutions.[10, 31] Optimal axial resolutions in a widefield microscope are typically $\sim$ 800 nm. Most biolmolecules of interest in the cell, however, have sizes on the order of 1–10 nm. Recent advances in fluorescence microscopy have allowed one to push past the limits imposed by Eqs. (1.3) and (1.4) to achieve improvements in the resolution by a factor of about 10. We will discuss some of these super-resolution techniques later in Chapter 1.3.

1.2.3 Comparing widefield and confocal microscopy

In widefield microscopy, fluorescence from the entire sample is ultimately collected by the detector. This includes light from out-of-focus planes, so that the signal-to-noise ratio (SNR) is often poorer when considering thicker fluorescently labeled specimens. This loss of resolution in the axial dimension can be mitigated by using a confocal microscope. Although the configuration is slightly more complex than that of a conventional widefield microscope, the main addition is a pinhole in front of the detector. This pinhole has the effect of rejecting out-of-focus light, or light outside the confocal spot. Consequently, confocal microscopes have improved axial resolutions of $\sim$ 500 nm,[32] while their lateral resolution is also improved by a factor of $\sqrt{2}$ for small pinholes (diameter of $\lesssim \rho_{\text{Airy}}/2$).[33] Whereas the fluorescence intensity values in a widefield microscope are recorded in pixels, thus forming an image, a confocal microscope only records the integrated fluorescence intensity in the confocal volume.

Laser-scanning confocal microscopes (LSCM) are used to scan the sample spatially to form a complete image. This can be achieved by utilizing two oscillating mirrors (for horizontal and vertical scanning, typically driven by galvanometers), but several adaptations for faster scanning have also been developed.[32, 33] Since much less light reaches the detector in a LSCM, the excitation intensity needs to be increased, which can lead to more photobleaching, which is detrimental as was previously discussed. The time taken to scan the sample also limits the image acquisition rates in the LSCM when compared to widefield microscopes. These limitations are addressed in the spinning disk confocal microscope, which has its own inherent limitations.[32–35]

1.2.4 Total internal reflection fluorescence microscopy

Total internal reflection fluorescence microscopy (TIRFM) offers a way to improve axial resolution, while still employing widefield imaging. In a TIRFM, as the name suggests, total internal reflection from light passing through the objective and the coverslip to the

sample is utilized. Total internal reflection occurs at the interface between the coverslip and the sample, with the evanescent field decaying exponentially with distance away from the coverslip. Since cell cytosol has a refractive index of ~ 1.38,[32, 36] an objective of higher NA must be used to make this possible. The sample is excited by the evanescent field with penetration depths that can go lower than 100 nm,[32, 36] which is an improvement to the axial resolution in confocal microscopy. One limitation, however, is that this technique only enables the user to image the sample near the interface of the coverslip.

1.2.5 Detectors used in fluorescence microscopy

Widefield microscopes mainly utilize area photodetectors known as charge-coupled devices (CCDs); however, complementary metal oxide semiconductor (CMOS) detectors are becoming more common in widefield fluorescence microscopy. Specifically, the electron multiplication CCD (EMCCD) and more recently developed scientific CMOS (sCMOS) detectors are favored because of their low-light sensitivities. While EMCCDs outperform sCMOS in very low-light conditions (important for mitigating photobleaching) in terms of SNR,[37, 38] sCMOS offers improved temporal and spatial resolutions, as well as greater fields of view (FOV) and dynamic ranges.[37] Note, however, that lower excitation powers are necessary in live-cell imaging, so that higher temporal resolutions require very low light sensitivities.[37] Furthermore, a wider dynamic range is unnecessary under such conditions.[37] The low-light detection capabilities of EMCCDs make them the current gold standard for TIRFM.

Unlike widefield microscopes, confocal microscopes use single-point detectors, such as photomultiplier tubes (PMT) and avalanche photodiodes (APD). Spinning disk confocal microscopes, however, do employ pixel array detectors, such as those previously mentioned.

1.3 Super-resolution microscopy

In the previous section, we compared several optical microscopy techniques in terms of their resolution capabilities. In recent years, super-resolution fluorescence microscopy (SRM) has garnered considerable attention in the biophysics field after the Nobel prize in chemistry was awarded in 2014 for its development. Here we outline some of the popular far-field SRM techniques.

Some SRM methods are theoretically limited by the improvement in resolution they are able to offer. One such technique is (standard) structured illumination microscopy

(SIM),[39] which can increase the resolution by a maximum factor of 2. The basic idea in this method is to shift the high spatial frequencies (*i.e.* structures below the resolution limit of the microscope) to lower frequencies. This can be accomplished by passing the excitation laser light through a diffraction grating that forms a stripe pattern with minimum distance close to the resolution limit. The interference with the sample forms a Moiré pattern that encodes high frequency information at lower frequencies. A super-resolved image can be constructed by repeating these measurements at several different grid rotations and then post-processing the Moiré patterns to reconstruct a super-resolved image. Typical lateral resolutions achieved with SIM are 100–130 nm and 300–400 nm axially.[5] Despite its limited resolution improvement, SIM is sometimes favored because it can be applied to a wide range of fluorophores, in contrast to other SRM techniques, and is minimally perturbing for live-cell imaging.

SRM methods that theoretically offer unlimited resolution improvements (but not in practice) are classified as either deterministic or stochastic approaches. Deterministic approaches effectively reduce the diffraction-limited focal spot size in a LSCM by targeting the outer region of the focal spot to inhibit fluorescence. On the other hand, stochastic approaches use widefield microscopy and the stochasticity of fluorescence emission, in processes such as photoblinking, to temporally separate fluorophores that are closely spaced and localize their diffraction centroids sequentially in time.

The most commonly used deterministic approach is stimulated emission-depletion (STED) microscopy.[40] In this method, the excitation laser is coaligned with a lower wavelength STED laser, which has a "doughnut" focal intensity distribution with a (near) zero-intensity central point. In the typical implementation, an excitation pulse is sent to excite the sample followed by a pulse from the STED laser that is used to deplete the excited fluorophores in the outer part of the focal spot through stimulated emission (SE). Consequently, the remaining fluorescence is then restricted to the center of the diffraction-limited focal spot. Since the STED pulse needs to compete with the decay of the fluorophores back to the singlet ground state through spontaneous emission, it must have a width of a few hundred picoseconds. The width of the outer region affected by the STED beam increases with intensity of the STED laser, which in turn improves the spatial resolution. Practically, limitations such as photobleaching restrict the user from increasing the intensity indefinitely. Lateral and axial resolutions of 30–80 nm and $\sim$ 100 nm have been achieved using STED, respectively.[4, 5, 10] The need for short laser pulses in traditional STED and efficient depletion of fluorophores by SE entails high laser intensities, making it challenging for live-cell imaging. Recent developments of the technique have addressed such shortcomings.[10] Other limitations include low photon

signal from a reduced focal spot and slower imaging, characteristic of LSCMs.[5]

Stochastic approaches include (fluorescent) photoactivation localization microscopy ((f)PALM)[41, 42] and (direct) stochastic optical reconstruction microscopy ((d)STORM).[43, 44] These techniques share the same basic concept for achieving super-resolution and are part of a broader subgroup of methods dubbed single-molecule localization microscopy (SMLM). SMLM offers better spatial resolutions than the previously mentioned methods, at the expense of reduced temporal resolution. Typical lateral and axial resolutions encountered in SMLM are $\sim$ 20 nm and $\sim$ 50 nm, respectively. The poor temporal resolution makes it incompatible for application in live cells in most instances.[5, 10] In SMLM, only a small subset of the fluorophores in a sample are emitting at a given time due to, for example, photoblinking in the case of STORM. Individual fluorophores can then be localized (assuming they are immobile) at each frame in an image series within the limitations of the diffraction limit. The precision error of localization, s_{loc}, is determined by the number of photons collected by an individual fluorophore, N_{phot}, such that (in the absence of noise),[4]

$$s_{\text{loc}} \equiv \sigma_{\text{PSF}}/\sqrt{N_{\text{phot}}}, \tag{1.5}$$

where σ_{PSF} is the standard deviation of the PSF, approximated to be Gaussian for localization. This last equation is true when the background noise is low and the pixel size is very small. More general expressions for the localization error when these effects are non-negligible have also been computed.[45, 46] By compiling the many individual fluorophore localizations after thousands of images, a super-resolved image can be formed. The necessity to localize individual molecules sequentially also entails that such approaches are usually limited to chemically fixed (i.e. nonliving) cells. The axial position of the fluorophores can also be inferred, for example, by encoding this information using astigmatism[47] or a double-helix PSF,[48] or by double-plane detection.[5, 49] For proper application of STORM, the time spent by the fluorescent probe in the off-state needs to be sufficiently long for a given density of fluorophores. Furthermore, the fluorophore density must obey the Nyquist criterion, so that there are two fluorophores *per* desired resolution length. Note since stochastic super-resolution approaches use widefield microscopy, the SNR can be improved by implementing TIRF imaging.

Super-resolution optical fluctuation imaging (SOFI)[50] is a stochastic approach that does not fall into the SMLM categorization. In this method, a spatio-temporal cross-cumulant[51] (a quantity related to the cross-correlation) is computed from an image series of immobile blinking (or any equivalent process) fluorophores. This cumulant, as a function of space, can be interpreted as an image. It turns out that the n^{th}-order cumulant

depends on the n^{th} power of the PSF.[50] If the PSF could be approximated as a Gaussian, for example, this would correspond to a "new" SOFI image with resolution improved by a factor of $\sqrt{n}$. As such, SOFI offers better temporal resolution than the previously mentioned stochastic methods at the cost of lower spatial resolution.[5] In practice, since reconstructed SOFI images do not scale linearly with brightness and different blinking rates, higher-order cumulants are limited in their improvement of the optical resolution. This has been addressed in spin-off techniques, such as, balanced SOFI (bSOFI),[51] which aimed to linearize the response to these parameters in the SOFI image.

More recently, a new localization SRM method called minimal photon fluxes (MINFLUX)[52] combines the concepts of SMLM and STED to achieve resolutions of ~ 1 nm (another recently published technique known as MINSTED[53] has also reported resolutions on this order, but we will not detail it here in the interest of space). The basic principle relies on probing a fluorophore with a donut shaped excitation beam (instead of the depletion beam used in STED) with an intensity minimum in the center and determining its position based on the number of photons emitted at several positions of the intensity minimum. The measurements are subsequently made more precise by iteratively moving the probe closer to the fluorophore. The closer the fluorophore is to the intensity minimum, the less emitted photons are collected. Ideally, the fluorophore would not emit any photons, indicating that its position is perfectly aligned with the intensity minimum. Localization becomes possible by stochastically switching the fluorophores between on/off states, as is done in PALM/STORM. In contrast to other SRM techniques, MINFLUX does not rely on acquiring more photons to achieve better resolutions, thus minimizing the effects of photobleaching and reducing acquisition times for localization (~ 100 µs). Furthermore, using centroid localization to determine particle positions, as is done in SMLM, can lead to inaccuracies depending on the orientation of the fluorophore.[54, 55] Conversely, localization using MINFLUX has been shown to be independent of such effects.

1.4 Mathematical primer

Before delving into the study of image correlation spectroscopy, we introduce some useful mathematical formalism. In this section, we begin by introducing stochastic processes and their autocorrelations. We then present the time-evolution equation (*i.e.*, the master equation) for a special class of processes, known as jump Markov processes. Finally, we outline the Gillespie algorithm for these processes,[56] which is used to simulate the master equation exactly.

1.4.1 Stochastic processes

In this work, we will be interested in understanding the fluorescence intensity fluctuations caused by particle diffusion and fluorophore blinking and bleaching (*i.e.*, fluorophore photophysics). These phenomena can be described mathematically as stochastic processes; that is, they can be described by a random variable at each point in time. Explicitly, the photophysical state of a fluorophore, Θ_t, can be written as:

$$\Theta_t = \begin{cases} 1 & \text{fluorophore is fluorescing at time } t \\ 0 & \text{otherwise} \end{cases}, \tag{1.6}$$

while the position of a particle diffusing in $\mathbb{R}^2$ can take on any value in that space at any point in time. The intensity at a given point in space as a function of time in a fluorescence microscopy image series, $i(\boldsymbol{r}, t)$, is also a stochastic process that is dependent on the particle positions and the photophysical states of the fluorophores. We will provide an expression for this quantity in Section 1.5.

All the stochastic processes considered in this work are known as Markov processes. A Markov process, X_t, has the property that its conditional probability density function at time t_j satisfies:

$$P(X_{t_j}|X_{t_{j-1}}, \ldots, X_{t_1}, X_{t_0}) = P(X_{t_j}|X_{t_{j-1}}), \tag{1.7}$$

for any $t_j \geq t_{j-1}$ and $j \geq 2$; that is, the value of X_{t_j} only depends on the last given state of the system, $X_{t_{j-1}}$. While this definition will not be especially useful in this work, we will be able to provide an expression for the conditional probability distribution of Θ_t through the master equation (presented in Section 1.4.3; see also photostate autocorrelation computation) by assuming it to be a Markov process, a standard assumption in the field for photophysical processes of a fluorophore. Interestingly, certain fluorophores have been shown to follow non-Markovian photoblinking trajectories; one such example being quantum dots, which exhibit power law photophysical kinetics.[57, 58]

We further define temporal homogeneity as a process that satisfies:

$$P(X_{t+\tau}|X_t) = P(X_{s+\tau}|X_s), \text{ for any } s, t > t_0;\ \tau \geq 0. \tag{1.8}$$

Moreover, the temporal homogeneous process, X_t, is said to be stable if:

$$\lim_{t\to\infty} P(x_t|x_0) = P_S(x), \tag{1.9}$$

where $P_S(x)$ is called the stationary distribution of X_t. The stationary distribution characterizes the process after it has had enough time to decorrelate from its previous state. This distribution will also be useful for computing the photostate autocorrelation in Chapter 2.

1.4.2 The autocorrelation

Central to this work is the time autocorrelation of the fluorescence intensities, $i(\boldsymbol{r}, t)$, which is usually written theoretically as (the same quantity is referred to as the autocovariance in mathematics):

$$\phi(\tau) \equiv \langle \delta i(\boldsymbol{r}, t) \delta i(\boldsymbol{r}, t+\tau) \rangle, \tag{1.10}$$

where $\langle \cdot \rangle$ is the expectation value, or ensemble average and $\delta i(\boldsymbol{r}, t) \equiv i(\boldsymbol{r}, t) - \langle i(\boldsymbol{r}, t) \rangle$.

In this last equation, we have implicitly assumed that $i(\boldsymbol{r}, t)$ is a (weakly) stationary process, *i.e.*, its mean and autocorrelation are independent of the time variable, t. Many factors, however, may break this assumption, the most obvious one being photobleaching. We will omit dependence on t throughout the rest of the introductory chapter to be consistent with the literature, but will reintroduce it in the main chapters, where we do consider the effects of photobleaching.

Another subtle point is that $i(\boldsymbol{r}, t)$ is usually assumed to be sampled discretely in time. There is, however, some hidden time information in the fluorescence intensity. This is due to the exposure time of the detector, during which fluorescence is collected. Furthermore, for the specific case of EMCCD detectors (the data presented in the main chapters was acquired using such detectors), there is also an associated dead time between image frames where the input signal is processed and fluorescence incident on the detector array is not recorded. It would, therefore, make sense to instead autocorrelate the fluorescence intensity collected during the exposure time of a single frame, so that we replace in the autocorrelation:

$$i(\boldsymbol{r}, t) \to \int_t^{t+\tau_i} i(\boldsymbol{r}, t), \tag{1.11}$$

where $0 \leq \tau_i \leq 1$ is the exposure time. Note that the integration of a Markov process is a well-defined quantity (see [56]). We will again only include this effect in the main chapters of this text. In Chapter 2, we will show that considering such effects in the autocorrelation can increase the dynamic range of measurable blinking rates, including ones that are faster than the detector sampling rate.

In practice, the autocorrelation of a process sampled uniformly in time, $x[t]$, of length T can be estimated as (for $\tau \geq 0$):

$$\hat{\phi}(\tau) \equiv \frac{1}{T-\tau} \sum_{t=0}^{T-\tau-1} \delta x[t]\delta x[t+\tau]; \tag{1.12}$$

however, if μ_t is unknown and is replaced by the sample mean, $\overline{x[t]}$, this estimator is generally biased, *i.e.*

$$\langle \hat{\phi}(\tau) \rangle \neq \phi(\tau; t). \tag{1.13}$$

We will revisit this later in Chapter 3, where we will provide a correction for this bias in our defined autocorrelation. Note that the estimator in Eq. (1.12) does have some nice asymptotic properties, such as being consistent[59] (*i.e.*, the estimator converges in probability to the parameter it is estimating, $\hat{\phi} \xrightarrow{p} \phi$) under certain assumptions.

The computation time of Eq. (1.12) scales as $\mathcal{O}(T^2)$; however, the autocorrelation can also be computed using the Wiener-Khinchin theorem, if δx_t is stationary, as:

$$\hat{\phi}(\tau) = \frac{1}{T-\tau} \mathcal{F}_\tau^{-1} \left(|\delta \tilde{x}^\star[\omega]|^2 \right), \tag{1.14}$$

where $\mathcal{F}_\tau^{-1}(\cdot)$ is the inverse discrete Fourier transform (DFT), ω is the Fourier transformation variable and $\tilde{x}^\star[\omega]$ is the DFT of $x^\star[t]$, where

$$\begin{gathered} x^\star[t] = x[t] \oplus \mathbf{0}_{T+s}, \text{ with} \\ s \equiv \arg\min_{m \geq 0} \{(2T+m) - 2^n = 0\}, \text{ for any integer } n \geq 0. \end{gathered} \tag{1.15}$$

Here we denote $\mathbf{0}_N$ as the N-dimensional zero vector. Eq. (1.14) reduces the computation time to scale as $\mathcal{O}(T \log T)$ when T is a power of 2, due to the fast Fourier transform (FFT) algorithm.[60] Owing to the cyclical nature of the DFT, Eq. (1.15) ensures that the autocorrelation computed using Eq. (1.14) is acyclical by padding with zeros to at least double the length of $x[t]$, as well as assuring that Eq. (1.14) utilizes the FFT by then padding to the next power of 2. Eq. (1.14) can also be extended for non-stationary processes through ensemble averaging, instead of time-averaging.[61]

1.4.3 The master equation

The time-evolution of a Markov process is generally characterized by an infinite order partial differential equation, known as the Kramers-Moyal equation.[56] For the purpose of this work, however, we will only need to consider jump Markov processes with discrete

states. A jump Markov process assumes that the number of jumps in any time interval is countable. In this special case, the time-evolution of the process, X_t, can be characterized by the forward master equation:[56]

$$\partial_t \mathcal{P}(X_t = n|X_{t_0} = n_0) = \sum_{\nu=-\infty}^{\infty} \Big[\mathcal{W}(n|n-\nu,t)\mathcal{P}(X_t = n-\nu|X_{t_0} = n_0) - \mathcal{W}(n-\nu|n,t)\mathcal{P}(X_t = n|X_{t_0} = n_0)\Big], \tag{1.16}$$

where $\mathcal{W}(n_2|n_1,t)$ is the rate of X_t jumping from $n_1 \to n_2$ at time t and $\mathcal{W}(n_2|n_1,t)\,\mathrm{d}t$ is the probability of this transition occurring in the time interval $[t, t+\mathrm{d}t)$. Notice the first term in the square brackets in Eq. (1.16) represents the probability "flux" into state n, while the second term represents the "flux" out of the state.

1.4.4 The Gillespie algorithm

We will use the Gillespie algorithm in this work to simulate the photoblinking/-bleaching process in Chapter 2. In order to do this, we will need to assume that this process is Markovian, as was previously mentioned. We will further assume temporal homogeneity for simplicity, although this assumption can be broken due to several factors affecting fluorophore photophysics, such as fluctuations in the excitation intensity, pH, temperature or oxygen levels.

In general, the approximate time evolution of a continuous Markov process can be simulated using the non-infinitesimal Langevin equation.[56] In the special case when X_t is a jump Markov process, it is possible to simulate the process exactly through the Gillespie algorithm.[62]

Here we briefly outline the algorithm for a temporally homogeneous process. This condition implies that the wait time to the next jump out of initial state n_1 is exponentially distributed,[56] so that one can simulate the next jump time, τ, by randomly sampling this distribution, so that:

$$\tau = -\frac{1}{\lambda}\ln(r_1), \tag{1.17}$$

where r_1 is a random sample taken from the continuous uniform distribution on $[0,1]$ (denoted $U(0,1)$) and

$$\lambda \equiv \sum_{n_2} \mathcal{W}(n_2|n_1). \tag{1.18}$$

The absence of time from this last equation is a consequence of temporal homogeneity. Note that λ is then simply the rate of leaving n_1 at any time. Given that a jump occurred, we now need to randomly determine the new state, n_2. This can be accomplished by solving:

$$n_2 = \arg\min_n \left\{ \lambda r_2 < \sum_{n'=-\infty}^{n} \mathcal{W}(n'|n_1) \right\}, \tag{1.19}$$

where r_2 is again sampled from $U(0,1)$. Eq. (1.19) is a direct consequence of the jump probabilities being proportional to the transition rates. Eqs. (1.17) and (1.19) describe how to exactly simulate a discrete jump Markov process.

1.5 Fluorescence fluctuations and correlation analysis

In Section 1.3 we introduced SRM methods, which cleverly overcome the physical limitations imposed by the diffraction limit on fluorescence microscopy. These techniques are mostly focused on obtaining super-resolved images of immobile particles, but typically do not reveal any information about the dynamics in the system (although there exist methods that aim to obtain both that we will briefly discuss in Chapter 3). Many approaches exist for characterizing dynamics in fluorescence microscopy and a very popular group of such approaches auto- or cross-correlate the fluctuations in fluorescence intensities to this end. The advantage of these correlation techniques is that they are relatively quick and accessible, sometimes involving only a simple linear regression in their application. Moreover, additive white noise present in an image series will not contribute to the autocorrelation at non-zero lag values by definition.

1.5.1 Mathematical representation of a fluorescence image series

We previously discussed that the image of a point source under a fluorescence microscope has a spatial intensity distribution characterized by the PSF. Thus, the intensity of an image series, $i(\boldsymbol{r}, t)$, at position $\boldsymbol{r}$ at time t is given by the spatial convolution of the apparent fluorophore density, $\rho(\boldsymbol{r}, t)$, and the PSF, $I(\boldsymbol{r})$, if we ignore the effects of noise, *i.e.*

$$i(\boldsymbol{r}, t) = I(\boldsymbol{r}) \otimes_{\boldsymbol{r}} \rho(\boldsymbol{r}, t). \tag{1.20}$$

Note that this equation assumes that the acquisition of the fluorescence image is a linear and shift invariant process. For example, shift invariance can be broken by a non-uniform excitation illumination, so that the PSF is not consistent over the entire field of view.

Spherical aberration can also affect the PSF when considering different imaging planes in 3D imaging.[63] See [64, 65] for proposed solutions to these issues.

The apparent fluorophore density can be written as:

$$\rho(\boldsymbol{r}, t) = \sum_m q_{m,t} \Theta_{m,t} \delta(\boldsymbol{r} - \boldsymbol{u}_{m,t}), \tag{1.21}$$

where $q_{m,t}$ is the brightness of fluorophore m at time t, given it is in an emissive state (we later add a stochastic integral to Eq. (1.20), at which point we refer to $q_{m,t}$ as the instantaneous rate of detector counts); $\boldsymbol{u}_{m,t}$ denotes the fluorophore's position; $\delta(\cdot)$ is the Dirac delta function, thus assuming fluorophores are ideal point sources of fluorescence; and $\Theta_{m,t}$ is the photo-emissive state of the fluorophore, as given in Eq. (1.6).

Note $q_{m,t}$ will generally depend on multiple factors, including the quantum efficiency of the fluorophore and the detector, the absorption cross-section of the fluorophore, how the detector converts analogue signal to discrete counts, as well as other factors. Note also we assume a linear relationship between excitation intensity and detector counts. This is a simplifying assumption as the conversion between number of photons and detector counts is a stochastic process. We will include this detector noise in our simulations following a model proposed by Hirsch *et al.* (2013)[66] for an EMCCD detector. Also note that $\Theta_{m,t}$ is affected by both photoblinking and photobleaching. We do not consider the faster transitions between the singlet states, as these are on much shorter timescales than the time-resolutions of CCD detectors, which we utilize to acquire our data. Using fluorescence correlation spectroscopy (FCS), which will be introduced in the next section, one can measure these faster dynamics.[67] We will be particularly interested in $\Theta_{m,t}$ throughout this work.

1.5.2 Fluorescence correlation spectroscopy

Historically, FCS[12–14] was the first method to propose an autocorrelation approach for analyzing fluorescence fluctuation data in 1972[12] and is still in use today. The method consists of autocorrelating the intensity fluctuations collected from a spatially fixed confocal focus in the sample over time.[68] Its first realization was applied to a reaction-diffusion system of particles for measuring diffusion coefficients and chemical kinetic rates. The restriction to a single point in space allows for high temporal resolution; however, this is at the cost of longer acquisition times to attain sufficient data for meaningful statistical analysis. Scanning FCS (SFCS) was developed to address such limitations by scanning the sample. Its first realization was proposed as a method for determining the molecular

weights of DNA molecules.[69] This set the stage for the development of the imaging analog image correlation spectroscopy (ICS) using an LSCM,[15] which we discuss in the next section.

FCS consists of computing the autocorrelation function (ACF), which is defined in FCS as:

$$\hat{\Phi}_{\mathrm{FCS}}(\tau) \equiv \frac{\frac{1}{T-\tau}\sum_{t=0}^{T-\tau-1}\delta i(t)\delta i(t+\tau)}{\left(\frac{1}{T}\sum_{t=0}^{T-1} i(t)\right)^2} \tag{1.22}$$

where we assumed stationarity. This last estimator is assumed to be an estimate of:

$$\Phi_{\mathrm{FCS}}(\tau) \equiv \langle\hat{\Phi}_{\mathrm{FCS}}(\tau)\rangle \simeq \frac{\langle\delta i(t)\delta i(t+\tau)\rangle}{\langle i(t)\rangle^2}. \tag{1.23}$$

This turns out to be true to lowest order of an expansion in terms of the fluctuations of Eq. (1.22); however, the ACF is asymptotically unbiased with its variance also approaching zero at large T (see [70]), as is also the case with the sample autocorrelation with unknown mean. Note in these last equations the intensity is only a function of t since it is only monitored at a single confocal spot in FCS. The normalization of the FCS ACF is specifically chosen to give information about the particle density within the confocal volume (we show this in the next section).

1.5.3 Image correlation spectroscopy

ICS[15, 16] was developed as the imaging (spatial domain) extension of FCS and involves correlation analysis of images from widefield and LSCM fluorescence microscopes. It was first utilized to measure concentrations and degrees of aggregation.[15] Assuming ergodicity in space and time, the idea of ICS is to use spatial information to calculate the same statistics as in FCS. Since ICS is not limited to fluorescence fluctuations acquired from a single point in space, statistically meaningful correlations can usually be computed with less temporal sampling.

In ICS techniques, the generalized spatiotemporal sample ACF is written as:

$$\hat{\Phi}_{\mathrm{ICS}}(\boldsymbol{\xi},\tau) \equiv \frac{\overline{\delta_{\boldsymbol{r}} i(\boldsymbol{r},t)\delta_{\boldsymbol{r}} i(\boldsymbol{r}+\boldsymbol{\xi},t+\tau)}_{\boldsymbol{r},t}}{\overline{i(\boldsymbol{r},t)}_{\boldsymbol{r}}\,\overline{i(\boldsymbol{r},t+\tau)}_{\boldsymbol{r}}}, \tag{1.24}$$

where we have used subscripts after the sample means to denote which variables are being averaged over, and

$$\delta_{\boldsymbol{r}} i(\boldsymbol{r}, t) \equiv i(\boldsymbol{r}, t) - \overline{i(\boldsymbol{r}, t)}_{\boldsymbol{r}}. \tag{1.25}$$

As in FCS, the ACF normalization in Eq. (1.24) is chosen so that the ACF amplitude gives information about the particle density. To see this, we evaluate the ACF as the lag variables approach $\mathbf{0}$. We do not evaluate at $\mathbf{0}$ because it is potentially affected by white noise.

Using Eqs. (1.20) and (1.21), we evaluate the ACF amplitude denominator, so that:

$$\begin{aligned} \langle i(\boldsymbol{r}, t)\rangle^2 &= \left(\sum_m \langle q_{m,t} I(\boldsymbol{r} - \boldsymbol{u}_{m,t})\rangle\right)^2 \\ &= N^2 q^2 \langle I(\boldsymbol{r} - \boldsymbol{u}_t)\rangle^2, \end{aligned} \tag{1.26}$$

where we assumed $q_{m,t} \equiv q$ is a constant; all fluorophores are identical so that the subscript m is dropped; N is the number of fluorophores in the sample volume; and $\boldsymbol{u}_t$ is the particle position. Note we have also omitted the photophysical term, $\Theta_{m,t}$, as it is unimportant for the current derivation (see [71] for a derivation including this term).

Similarly, we evaluate the ACF amplitude numerator:

$$\begin{aligned} \langle \delta i^2(\boldsymbol{r}, t)\rangle &= \sum_{m,n} \langle \delta i_m(\boldsymbol{r}, t) \delta i_n(\boldsymbol{r}, t)\rangle \\ &= \sum_m \langle \delta i_m^2(\boldsymbol{r}, t)\rangle \\ &= N q^2 \langle \delta I^2(\boldsymbol{r} - \boldsymbol{u}_t)\rangle. \end{aligned} \tag{1.27}$$

In this last equation, we defined $i_m(\boldsymbol{r}, t)$ to be the fluorescence intensity contribution from the m^{th} fluorophore and assumed independence between different particles.

To evaluate the ensemble averages in Eqs. (1.26) and (1.27), we assume that the sample being imaged is two-dimensional *e.g.* a cell membrane. Recall that the 2D PSF for a point source of light in an optical microscope is an Airy disk, which can be reasonably approximated as a Gaussian, *i.e.*,

$$I(\boldsymbol{r}) = I_0 \exp(-2\boldsymbol{r}^2/\omega_0^2), \tag{1.28}$$

with ω_0 being the e^{-2} radius of the PSF and I_0 being the amplitude of the excitation intensity. Note this assumes a linear dependence between the excitation intensity and the fluorescence intensity. This is a good approximation at low light intensities,[25] but

breaks down at higher intensities due to optical saturation, where fluorophore excitation to the excited singlet state is limited by the relaxation rate to the ground singlet state.

We then have:

$$\langle I^2(\boldsymbol{r}-\boldsymbol{u}_t)\rangle = \langle I^2(\boldsymbol{u}_t)\rangle = \int_{\mathbb{R}^2} \mathrm{d}\boldsymbol{u}_t \underbrace{P(\boldsymbol{u}_t)}_{=1/A_S} I^2(\boldsymbol{u}_t) = I_0^2\pi\omega_0^2/4A_S, \text{ and} \tag{1.29}$$

$$\langle I(\boldsymbol{r}-\boldsymbol{u}_t)\rangle^2 = \langle I(\boldsymbol{u}_t)\rangle^2 = \left(\int_{\mathbb{R}^2} \mathrm{d}\boldsymbol{u}_t\, P(\boldsymbol{u}_t) I(\boldsymbol{u}_t)\right)^2 = I_0^2\pi^2\omega_0^4/4A_S^2, \tag{1.30}$$

where A_S is the sample area and the unconditioned probability density of finding a fluorophore at any time is uniform within this area. We also assumed $\omega_0^2 \ll A_S$ to extend the integrals over real space.

Using these last expressions, we write the ACF amplitude:

$$\begin{aligned}\Phi(\boldsymbol{\xi}\to\mathbf{0}, \tau\to 0) &= \frac{\langle \delta i^2(\boldsymbol{r},t)\rangle}{\langle i(\boldsymbol{r},t)\rangle^2} \\ &= \frac{1}{N\pi\omega_0^2/A_S} - \frac{1}{N}.\end{aligned} \tag{1.31}$$

The first term in this equation represents the amplitude of the ACF, whereas the second term is a constant offset. Note that the first term is the inverse of the expected number of fluorophores within a characteristic PSF area.

The original ICS technique was developed using only the spatial autocorrelation. The more general spatiotemporal ICS (STICS)[72] considers both spatial and temporal lag variables, as its name implies. The STICS ACF offers a visual representation of the particle dynamics in a system. Briefly, a diffusing population will broaden the STICS ACF Gaussian profile and a flowing population will appear as a translated Gaussian peak. Another technique dubbed k-space image correlation spectroscopy (kICS)[73] investigates the autocorrelation of the spatially Fourier transformed intensities. This approach has several advantages, including being able to separate the photophysics from the transport properties (*e.g.* diffusion, flow) in a system, as well as the ability to obtain a PSF independent ACF. We discuss kICS further in Chapter 3.

Particle ICS (PICS)[74] is a technique that combines ICS and single-particle tracking (SPT) to determine diffusion coefficients. Unlike other ICS techniques, PICS normalizes by the number of particles at a specific point in time. Another method, dubbed raster ICS (RICS),[75] calculates spatial correlations of fluorescence along the independent orthogonal scan directions of the raster scan acquired image, collected on an LSCM. RICS considers the scan times in its autocorrelation, thus allowing for measurement of faster

diffusion coefficients in comparison with other ICS techniques.

The assumption of ergodicity connecting FCS to ICS is a strong one. Any inhomogeneous distribution of the fluorophores (or fluorescence) in space causes this assumption to break. Moreover, parameters that vary spatially (*e.g.* viscosity, confinement potentials) will alter the particle dynamics in different regions of the sample being studied. Likewise, non-stationary temporal processes, such as photobleaching, also prevent one from simply calculating the ACF through a time average without considering these effects. These types of spatiotemporal non-uniformities are especially encountered when studying cellular samples.

The lack of ergodicity in these systems calls into question how we should compute the averages in the sample ACF. Furthermore, the expected value of the ACF will depend on which means are used in the definition of the sample ACF. For instance, in Chapter 2 we show that subtracting the temporal mean of the fluorescence intensity, as opposed to the spatial one, when defining the intensity fluctuations in the ACF, results in a loss of information in the photoblinking. We further use a moving/local spatial mean to lessen the effect of spatial heterogeneities caused by, for example, the excitation illumination beam pattern. In Chapter 3, we show that subtracting a local temporal mean in the intensity fluctuation definition results in a filtering of unwanted information about blinking immobile fluorophore positions. Therefore, one must choose the definition of the ACF carefully depending on the quantities that they hope to measure.

1.5.4 k-Space image correlation spectroscopy (kICS)

As mentioned above, kICS[73] is an ICS technique that considers the autocorrelation of the spatial Fourier transform of the microscope image fluorescence intensities. One obvious advantage of kICS is the utilization of the convolution theorem in Eq. (1.20), allowing for the possibility of dividing out the PSF from the autocorrelation. Another advantage is the ability to separate photophysical and transport kinetics in certain systems, as will be shown below.

To derive the kICS autocorrelation, we first consider the spatial Fourier transform of the image series intensities, defined in Eq. (1.20):

$$\tilde{i}(\boldsymbol{k},t) = \tilde{I}(\boldsymbol{k})\tilde{\rho}(\boldsymbol{k},t). \tag{1.32}$$

The kICS autocorrelation is defined as (assuming stationarity):

$$\tilde{\phi}(\boldsymbol{k},\tau) = \langle \tilde{i}(\boldsymbol{k},t)\tilde{i}^{*}(\boldsymbol{k},t+\tau)\rangle. \tag{1.33}$$

Using Eq. (1.21) in this last equation, we have:

$$\tilde{\phi}(\boldsymbol{k},\tau) = Nq^2|\tilde{I}(\boldsymbol{k})|^2\langle\Theta_t\Theta_{t+\tau}\rangle\langle e^{i\boldsymbol{k}\cdot(\boldsymbol{u}_{t+\tau}-\boldsymbol{u}_t)}\rangle, \tag{1.34}$$

where we have used the Fourier transform definition $\tilde{f}(\boldsymbol{k}) \equiv \int \mathrm{d}\boldsymbol{r}\exp(i\boldsymbol{k}\cdot\boldsymbol{r})f(\boldsymbol{r})$ and made the same assumptions as in the last section. Note we have assumed independence between particle position and photophysics in this last equation. Such an assumption may not hold if the excitation power varies sufficiently over the region of interest (ROI) being analyzed and optical saturation has not been attained over its entirety (see [76]). Note further we do not consider these effects of the excitation beam intensity profile in our formalism of an image series in Eq. (1.20), as was previously mentioned.

With the substitution $\boldsymbol{\zeta} \equiv \boldsymbol{u}_{t+\tau} - \boldsymbol{u}_t$, the expectation value depending on the particle positions can be rewritten in 2D as:

$$\langle e^{i\boldsymbol{k}\cdot\boldsymbol{\zeta}}\rangle = \int_{\mathbb{R}^2} \mathrm{d}\boldsymbol{\zeta}P(\boldsymbol{\zeta},\tau)e^{i\boldsymbol{k}\cdot\boldsymbol{\zeta}} = \tilde{P}(\boldsymbol{k},\tau), \tag{1.35}$$

which is the Fourier transformed probability distribution of the particle displacement after time τ. Note we have implicitly assumed that the particle position is a stationary process. We have further assumed that the sample area is large compared to the particle displacements, so that the last integral is carried over all space.

The convection-diffusion process is one example of a stationary process of interest in this work. The motion associated with this process is free diffusion with a velocity. Its time-evolution equation is given by:[77]

$$\partial_\tau P(\boldsymbol{\zeta},\tau) = \boldsymbol{\nabla}_{\boldsymbol{\zeta}}\cdot\left((D\boldsymbol{\nabla}_{\boldsymbol{\zeta}} - \boldsymbol{v})P(\boldsymbol{\zeta},\tau)\right), \tag{1.36}$$

where D is the diffusion coefficient and $\boldsymbol{v}$ is the velocity. Solving this equation in Fourier space gives:[77]

$$\tilde{P}(\boldsymbol{k},\tau) = e^{-|\boldsymbol{k}|^2 D\tau}e^{i\boldsymbol{k}\cdot\boldsymbol{v}\tau}. \tag{1.37}$$

In the case of free diffusion, one can then separate diffusion dynamics in Eq. (1.34) from the rest of the equation by writing:

$$\ln\tilde{\phi}(\boldsymbol{k},\tau) = \ln\left(\frac{1}{4}Nq^2I_0^2\pi^2\omega_0^4\langle\Theta_t\Theta_{t+\tau}\rangle\right) - |\boldsymbol{k}|^2\left(D\tau + \frac{\omega_0^2}{4}\right), \tag{1.38}$$

where we have used the Fourier transform of the Gaussian PSF (see Eq. (1.28)) to write this last expression. The fit for the diffusion coefficient then simply reduces to be linear in

$|\boldsymbol{k}|^2$ for fixed τ and the offset term containing the photophysical information can simply be ignored. In Durisic *et al.* (2007),[78] the authors applied kICS to measure diffusion rates independently of photoblinking of quantum dot probes tagging cell surface receptors, for example.

Convection-diffusion in 3D will also be of interest to us. To determine the kICS autocorrelation of this process, we first need to provide an expression for the 3D PSF. A simple approximation is to assume a Gaussian PSF in the axial dimension with an e^{-2} radius z_0, such that:

$$I(\boldsymbol{r}) = I_0 \exp(-2(\boldsymbol{r}_\parallel^2/\omega_0^2 + z^2/z_0^2)), \tag{1.39}$$

where $\boldsymbol{r}_\parallel$ is the displacement in the lateral plane, and z is that along the axial direction. More accurate analytical expressions exist for predicting the 3D PSF (*e.g.*, see [79]). The details of the kICS autocorrelation calculation for 3D convection-diffusion are given in Kolin *et al.* (2006).[73] The resulting expression reads:[73]

$$\tilde{\phi}(\boldsymbol{k},\tau) = \tilde{\phi}_{2D}(\boldsymbol{k},\tau) \times \frac{z_0^2}{4\sqrt{\pi}\sqrt{4D\tau + z_0^2}} \exp\left(-\frac{v_z^2\tau^2}{4D\tau + z_0^2}\right), \tag{1.40}$$

with $\tilde{\phi}_{2D}(\boldsymbol{k}_\parallel,\tau)$ being the expression found for the kICS autocorrelation in the 2D case in Eq. (1.34); $\boldsymbol{k}_\parallel$ being the counterpart of $\boldsymbol{r}_\parallel$ in Fourier space; and v_z being the velocity in the axial direction. The 3D kICS autocorrelation is thus a product of the 2D autocorrelation with an additional factor accounting for the axial component of the system.

In Chapter 2, we provide an explicit expression for the photophysical correlation in Eq. (1.34). Specifically, we consider a simple two-state on-off system with photobleaching. The on-state occurs when the fluorophore is switching between the ground singlet and excited singlet states and has the potential to emit fluorescence photons, while the off-state occurs when the fluorophore becomes trapped in the triplet state, or any other intermittent "dark"-state, for example. We will also consider the time-integration effects of the detector in our derivation. In Chapter 3, we extend kICS to analyze systems with non-uniformly distributed, immobile blinking and bleaching fluorophores. The application of the original technique to such a system would yield oscillations in the autocorrelation, as will also be shown in Chapter 3.

1.6 Outline of main chapters

Before we proceed to the main chapters, we first briefly outline their contents.

In Chapter 2, we introduce a correlation technique for rapidly measuring photophysical rates of immobile fluorophores. We saw in Chapter 1.3 the rates of these processes are important for optimizing single-molecule localization microscopy (SMLM), a commonly used subset of SRM methods. Fluorescent probe photophysical rates can also be useful for sensing chemical changes in the cell environment. A common technique for measuring these rates is to localize single molecules, binarize their intensity traces through intensity thresholding and then fit the resulting binary traces. We will show that this method can lead to aliasing when the photophysical processes are fast compared to the camera detector sampling rate. Furthermore, this type of method is typically time-consuming and cannot be utilized at high fluorescent probe densities, where single molecules cannot be resolved in isolation.

In Chapter 3, we introduce another correlation technique that can rapidly measure diffusion properties and photophysical rates of a system simultaneously. Unlike other fluorescence image correlation methods, our method was capable of analyzing regions with non-uniform distributions of immobile blinking fluorescent molecules, or fluorophores. This allowed us to study the dynamics in systems relevant to SMLM. We believe this is important as most SMLM studies have so far been focused on producing static super-resolution images without considering dynamics.

Preface to Chapter 2

In this chapter we will introduce a novel fluorescence image correlation technique for measuring photoblinking and photobleaching rates of immobile fluorophores. Currently, the most commonly used method for measuring photoblinking rates is to localize single fluorophores and fit their intensity traces. One way to do this is to use hidden Markov modeling as described in [80] (in fact, this method was developed for analyzing fluorescence resonance energy transfer trajectories, but this process is analogous to photoblinking under certain assumptions). The on- and off-blinking times are then collected from the analyzed fluorophores and binned in histograms that are subsequently fit with exponential distributions to determine the mean on-off blinking times (this is the case for a simple two-state on-off blinking system). This approach is not only time-consuming, taking hours to implement typically, but also does not consider the exposure time of the camera detector, which can result in an aliased measurement of the blinking rates (when the rates are near or faster than the camera image frame rate). By considering the effect of the camera integration time in our ACF definition, we showed that we can successfully measure these faster photoblinking rates in photoblinking simulations with simulated EMCCD noise and for real fluorophores; namely, we investigated DNA-Cy5 duplexes immobilized on a glass coverslip. Note that the single-molecule approach can also consider the effects of camera exposure time (to our knowledge, this has not yet been done). Autocorrelation techniques can also be used at much higher fluorophore densities than single-molecule methods.

Analyzing single-molecule intensity traces is crucial when different fluorophores do not assume the same photoblinking rates. On the other hand, the autocorrelation approach we developed cannot determine the underlying probability distributions for the blinking rates. Furthermore, unlike single-molecule methods, our technique requires uniformly distributed fluorophores. This assumption can be hard to satisfy, for instance, when the fluorophores are aggregated. Another effect that needs to be considered when applying our method is the sampling bias encountered when dealing with rates relevant to STORM single-molecule localization studies (see Chapter 1.3). The high-throughput nature of our method, however, makes it a good candidate for rapidly screening dyes for application in

SMLM and SOFI studies and to actively probe for environmental changes in the cell by detecting changes in the blinking rates of fluorescent probes.

Chapter 2

A High-Throughput Image Correlation Method for Rapid Analysis of Fluorophore Photoblinking and Photobleaching Rates

This section is based on the published manuscript:
Sehayek, S., Gidi, Y., Glembockyte, V., Brandão, H.B., François, P., Cosa, G., and Wiseman, P.W. A High-Throughput Image Correlation Method for Rapid Analysis of Fluorophore Photoblinking and Photobleaching Rates, *Biophys. Rep.* **13**, 10, 11955–11966 (2019).[1]

2.1 Abstract

Super resolution fluorescence imaging based on localization microscopy requires tuning the photoblinking properties of fluorescent dyes employed. Missing is a rapid way to analyze the blinking rates of the fluorophore probes. Herein we present an ensemble autocorrelation technique for rapidly and simultaneously measuring photoblinking and bleaching rate constants from a microscopy image time series of fluorescent probes that is significantly faster than individual single-molecule trajectory analysis approaches. Our method is accurate for probe densities typically encountered in single-molecule studies as well as for higher-density systems which cannot be analyzed by standard single-molecule techniques. We also show that we can resolve characteristic blinking times that are faster than camera detector exposure times, which cannot be accessed by threshold based single molecule approaches due to aliasing. We confirm this through computer simulation and single-molecule imaging data of DNA-Cy5 complexes. Finally, we demonstrate that with

sufficient sampling our technique can accurately recover rates from stochastic optical reconstruction microscopy (STORM) super-resolution data.

2.2 Introduction

Fluorescence microscopy is the most widely used microscopy modality for live cell imaging and within this field super-resolution fluorescence microscopy has expanded rapidly since initial developments just over a decade ago. Single-molecule localization microscopy (SMLM) is a major subgroup of these methods that relies on emission photoblinking, or reversible binding/unbinding of probes, for molecular localization[1–4]. Therefore, probe development and experimental optimization of SMLM requires the understanding of probe photophysical and photochemical behavior. Quantitative biophysics measurements are also impacted by emission blinking of probes. Researchers have shown that fluorescence correlation spectroscopy (FCS) measurements of quantum dot and nanoparticle labeled biomolecules are impacted by blinking of the probe nanoparticles[5, 6]. Thus it is important to be able to measure the rates of photo-processes accurately and rapidly to optimize imaging based measurements and for screening new dyes and probes for single molecule and super-resolution applications.

Currently, it is standard to measure fluorophore photoblinking rates from a fluorescence microscopy image series by first localizing a large set of individual (isolated) dye molecules and then fitting their respective intensity time traces using logistic regression (or a multinomial regression when intermediate fluorescent states exist). The localization and binarization of these traces is not only time-consuming, dependent on subjective choice of arbitrary thresholds and manual user-input, but also needlessly discards important intensity information that can be used to more accurately determine the photophysical and photochemical properties of the system.

Here we develop an automated image autocorrelation method that can rapidly and simultaneously measure "ensemble" photophysical/-chemical rates (*i.e.* photoblinking and bleaching rates) from a region of interest (ROI) encompassing multiple fluorescent dyes within a fluorescence microscopy intensity image series (see Figure 2.1). We show that independent of the underlying photophysical/-chemical process, we can obtain an expression for the autocorrelation function (ACF) that is solely dependent on the photophysical/-chemical rate parameters.

In this work, we studied dyes that exhibit exponentially distributed dwell times in both a fluorescent on- and a non-fluorescent off-state, while also accounting for the effect of photobleaching. Moreover, we lay the mathematical groundwork for extending to more

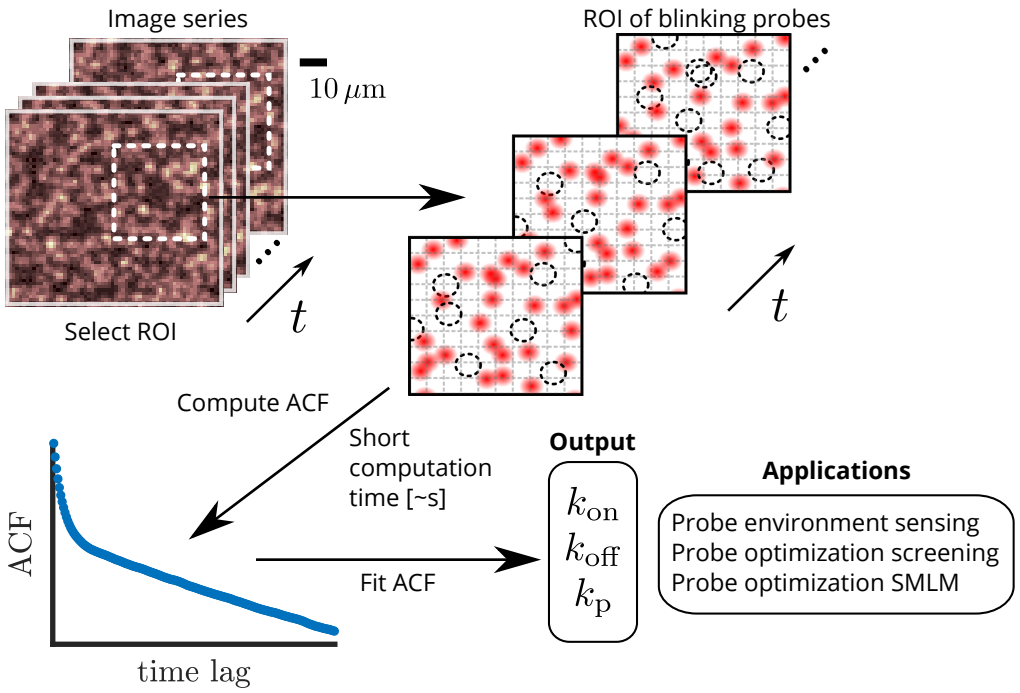

FIGURE 2.1: Schematic illustration of autocorrelation method applied to high-density fluorescent image series of immobile blinking fluorophores. An ROI is first chosen to minimize spatial non-uniformities (top-left) and sample a number of fluorophores (top-right; dashed circles represent positions of dyes that are not emitting in a given frame). The fluorescence fluctuation time autocorrelation is then computed for each ROI pixel. The ACF from each pixel is then averaged (bottom-left) and subsequently fit for the photophysical/-chemical parameters using the fit model. Applications include fast probe screening for photophysical and photochemical properties, which can be especially useful in SMLM, and using probe blinking rates for environment sensing.

complex systems (*e.g.* with intermediates, multiple fluorescent states, *etc.*). Furthermore, our method can be applied to any system that exhibits binary emission states. We were able to successfully apply our method to fluorophore densities ranging from those typically encountered in single-molecule studies (< 1 molecule/μm^2) to higher-density systems where single molecules cannot be resolved. Single-molecule methods for extracting photoblinking rates, which rely on being able to localize isolated single dyes, cannot analyze these higher-density systems akin to those exploited in SMLM imaging modalities (> 1 molecule/100 nm^2). We also show that by using the full fluorescence intensity information from a CCD camera, we are able to accurately recover photoblinking rates that are faster than the image frame rate of the camera detector. We achieve this by using the full intensity information (*i.e.* no arbitrary threshold) and accounting for the detector integration time in our ACF fits.

Our approach involves first deriving the ACF for immobile fluorescent dyes, assumed to be subject to some general photophysical/-chemical emission process. We proceed to show that we are able to accurately recover photophysical/-chemical rates from a wide range of realistic computer simulations, including those with rates greater than the detector's sampling frequency, when we account for the effect of detector exposure time in the autocorrelation analysis. We also show that we can successfully recover rates from simulations with high densities of blinking particles, which could not be analyzed by standard single-molecule methods. We further successfully analyze additional simulations generated by the TestSTORM[7] software package. We experimentally demonstrate our technique on immobilized DNA-Cy5 complexes and compare our results to those obtained *via* typical single-molecule analysis, showing that our method can extract photophysical/-chemical rates that exceed the camera detector's sampling frequency, while standard single-molecule analysis cannot. Finally, we analyze STORM super-resolution data and show that with sufficient sampling, our method can accurately recover the photophysical/-chemical rates.

We anticipate that our high throughput image correlation based method will prove useful to researchers interested in rapid characterization of fluorescence probe emission and photobleaching characteristics as is the case for developers optimizing new fluorescent proteins through genetic screens, fluorescent probe designers as well as applied researchers who wish to optimize probe photoblinking for single molecule localization and stochastic optical fluctuation imaging. We also expect our technique will prove useful for testing photo-stabilization approaches.

2.3 Results and Discussion

2.3.1 Theory

Here we derive the ACF for immobile particles subject to a general photophysical/-chemical process. The basis of our approach is similar to that described by Kolin and Wiseman (2007) in development of the temporal image correlation spectroscopy (TICS) fluorescence fluctuation technique[8]. We start with the definition of a fluorescence microscopy image series of intensities, $i(\boldsymbol{r}, t)$:

$$i(\boldsymbol{r}, t) = i_s(\boldsymbol{r}, t) + \epsilon(\boldsymbol{r}, t) = I(\boldsymbol{r}) \circledast_{\boldsymbol{r}} \rho(\boldsymbol{r}, t) + \epsilon(\boldsymbol{r}, t), \tag{2.1}$$

where $i_s(\boldsymbol{r}, t)$ is the fluorescence signal from the labeled particles at position $\boldsymbol{r}$ and time t, hereafter referred to as the signal; $\epsilon(\boldsymbol{r}, t)$ is an additive noise term, which we assume to be independent from the signal and from itself for any $(\boldsymbol{r}, t) \neq (\boldsymbol{r}', t')$; $I(\boldsymbol{r})$ is the optical point-spread function (PSF); $\circledast_{\boldsymbol{r}}$ is a spatial convolution; and $\rho(\boldsymbol{r}, t)$ is the *effective* particle density. For a discrete distribution of particles,

$$\rho(\boldsymbol{r}, t) = \sum_m q_{m,t} \Theta_{m,t} \delta(\boldsymbol{r} - \boldsymbol{u}_{m,t}). \tag{2.2}$$

In this last equation, $\delta(\cdot)$ is the 2-dimensional Dirac delta function; m is the particle index; $q_{m,t}$ is the instantaneous rate of detector counts for the m^{th} particle at time t, which depends on several factors, including the number of photons emitted by the particle, quantum efficiency of the detector, and camera gain; $\boldsymbol{u}_{m,t}$, and $\Theta_{m,t}$, are the position, and the photo-emissive state of the m^{th} particle at time t, respectively, and

$$\Theta_{m,t} = \begin{cases} 1 & m^{\text{th}} \text{ particle is fluorescing at time } t \\ 0 & \text{otherwise} \end{cases}. \tag{2.3}$$

We proceed to write the autocorrelation of the intensity fluctuations between two fixed times, t_1 and t_2 ($t_1 \neq t_2$), as

$$\begin{aligned} \phi_{\delta i}(t_1, t_2) &\equiv \langle \delta i(\boldsymbol{r}, t_1) \delta i(\boldsymbol{r}, t_2) \rangle \\ &= \langle \delta i_s(\boldsymbol{r}, t_1) \delta i_s(\boldsymbol{r}, t_2) \rangle \\ &\equiv \langle i_s(\boldsymbol{r}, t_1) i_s(\boldsymbol{r}, t_2) \rangle - \langle i_s(\boldsymbol{r}, t_1) \rangle \langle i_s(\boldsymbol{r}, t_2) \rangle, \end{aligned} \tag{2.4}$$

where $\langle\cdot\rangle$ denotes an ensemble average; and

$$\delta i(\boldsymbol{r},t) \equiv i(\boldsymbol{r},t) - \langle i(\boldsymbol{r},t)\rangle. \tag{2.5}$$

In practice, we compute the intensity fluctuations (given in the last equation) by subtracting local spatial means to help minimize spatial non-uniformity (see Autocorrelation computation section for further details). Moreover, the equivalence between the autocorrelated intensity fluctuations and the autocorrelation of the signal in Eq. (2.4) follows from the autocorrelation of a white-noise process being a delta function. Note that the additive noise term can have non-zero mean for this equality to hold because we autocorrelate the intensity fluctuations. Note as well if $\Theta_{m,t}$ were a weakly-stationary process in time, we would further assume the autocorrelation in Eq. (2.4) can be written as[9],

$$\phi_{\delta i}(t_1,t_2) \equiv \phi_{\delta i}(|t_2 - t_1|); \tag{2.6}$$

however, we do not make this assumption here, so that we can later introduce photobleaching into our photophysical/-chemical model.

We proceed by computing the first term in Eq. (2.4) using Eqs. (2.1) and (2.2),

$$\begin{aligned}
\phi_{i_s}(t_1,t_2) &\coloneqq \langle i_s(\boldsymbol{r},t_1) i_s(\boldsymbol{r},t_2)\rangle \\
&= q^2 \sum_{m,n} \langle \Theta_{m,t_1}\Theta_{n,t_2}\rangle \langle I(\boldsymbol{r}-\boldsymbol{u}_{m,t_1}) I(\boldsymbol{r}-\boldsymbol{u}_{n,t_2})\rangle \\
&= Nq^2 \langle \Theta_{t_1}\Theta_{t_2}\rangle \langle I^2(\boldsymbol{r}-\boldsymbol{u})\rangle \\
&\quad + N(N-1)q^2 \langle\Theta_{t_1}\rangle\langle\Theta_{t_2}\rangle \langle I(\boldsymbol{r}-\boldsymbol{u})\rangle^2,
\end{aligned} \tag{2.7}$$

where N is the number of fluorophores in the analyzed ROI.

In the equation above we have implicitly assumed independence of photostate between different particles, as well as independence of photostate from position. Furthermore, we have assumed all fluorophores have equal quantal brightness on average (*i.e.* $\langle q_{m,t}\rangle \equiv q$), are immobile, and have identical photophysical/-chemical rates. These assumptions only need to hold within the ROI being analyzed. Note the particle indices (m and n) were dropped because we further assume the particles are identical.

Similarly, we can write,

$$\langle i_s(\boldsymbol{r},t_1)\rangle\langle i_s(\boldsymbol{r},t_2)\rangle = N^2 q^2 \langle\Theta_{t_1}\rangle\langle\Theta_{t_2}\rangle\langle I(\boldsymbol{r}-\boldsymbol{u})\rangle^2. \tag{2.8}$$

Eq. (2.4) then reduces to,

$$\phi_{\delta i}(t_1, t_2) = Nq^2 \left(\langle I^2(\boldsymbol{u}) \rangle \langle \Theta_{t_1} \Theta_{t_2} \rangle - \langle I(\boldsymbol{u}) \rangle^2 \langle \Theta_{t_1} \rangle \langle \Theta_{t_2} \rangle \right), \tag{2.9}$$

where we have used the fact that shifting the PSF does not change its mean if the fluorophores are assumed to be *uniformly distributed*. We show that the second term in the previous equation is negligible in the Supporting Information (SI). With the omission of this term, the autocorrelation is simply

$$\phi_{\delta i}(t_1, t_2) = A \langle \Theta_{t_1} \Theta_{t_2} \rangle, \tag{2.10}$$

where A is an all-encompassing term containing non photophysical/-chemical quantities; specifically,

$$A \equiv Nq^2 \langle I^2(\boldsymbol{u}) \rangle. \tag{2.11}$$

Accounting for the integration time of the detector amounts to redoing the above derivation, such that

$$i(\boldsymbol{r}, t) \to \int_t^{t+\tau_i} i(\boldsymbol{r}, t) \, \mathrm{d}t. \tag{2.12}$$

In this case, we instead obtain

$$\phi_{\delta i}(\tau; t) = A \int_{t+\tau}^{t+\tau+\tau_i} \int_t^{t+\tau_i} \langle \Theta_{t_1} \Theta_{t_2} \rangle \, \mathrm{d}t_1 \mathrm{d}t_2, \tag{2.13}$$

with τ_i being the detector exposure time per frame.

Finally, the temporal autocorrelation of the image series is written as

$$\Phi(\tau) \equiv \frac{1}{T - \tau} \sum_{t=0}^{T-\tau-1} \phi_{\delta i}(\tau; t), \tag{2.14}$$

where T is the number of frames in the image series. One can further normalize Eq. (2.14) by $\Phi(\tau = 1)$ to avoid fitting for A:

$$\tilde{\Phi}(\tau) \equiv \frac{\Phi(\tau)}{\Phi(\tau = 1)}. \tag{2.15}$$

This quantity will be referred to as the ACF throughout this work. Note that it is solely a function of photophysical/-chemical parameters. We do not divide by $\Phi(\tau = 0)$ as it is affected by white-noise.

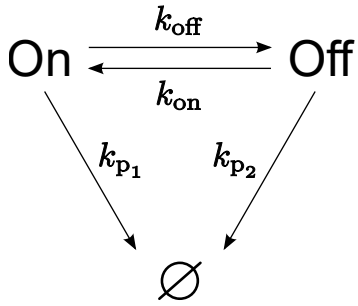

FIGURE 2.2: General photobleaching model

A simple photophysical/-chemical model is shown in the schematic below with on/off rates k_{on} and k_{off}, respectively, and different photobleaching rates from the on- and off-states, k_{p_1} and k_{p_2}, respectively. The photobleached state is denoted by ∅. Scheme 2.2 is a general model, but can be applied to, for example, a system of fluorophores exhibiting different photobleaching rates from the first excited singlet and triplet states (assuming bleaching does not occur from higher order energy states). Note we do not consider fast processes such as the exchange between the ground and first excited singlet states as they are well beyond the time resolution of CCD cameras.

As an example, for the simplified case when $k_{p_1} = k_{p_2} = k_p$ in Scheme 2.2, Eq. (2.16) can be calculated explicitly to give

$$\Phi(\tau) = \frac{A}{T-\tau}\frac{k_{on}}{k_p K^3 K_p}\frac{\left(e^{-k_p\tau} - e^{-k_p T}\right)}{\left(1-e^{-k_p}\right)}\times \\ \left\{k_{off}k_p\left(1-e^{-K}\right)\left(1-e^{-K_p}\right)e^{-K(\tau-1)} + k_{on}KK_p\left(1-e^{-k_p}\right)\right\}, \tag{2.16}$$

where $K \equiv k_{on} + k_{off}$ and $K_p \equiv K + k_p$. Note we set $\tau_i = 1$ (in units of frames here) for simplicity *i.e.* no dead time. More details on how to explicitly compute Eq. (2.14) for the general process illustrated in Scheme 2.2 are provided in the SI. We would like to emphasize that all the rates are fit simultaneously in the ACF (*i.e.* k_{on}, k_{off} and k_p). This would not have been possible had we defined the fluctuations in Eq. (2.5) using a temporal mean subtraction (see SI), as is done when spatial information is not available *e.g.* as in FCS.

The relative simplicity of Eq. (2.16) will be helpful to elucidate several important features of the ACF as computed from Eq. (2.15) throughout this work, even though we will be using a model that assumes photobleaching to occur only from the off-state for fitting purposes (omitted from main text due to size; see Eq. (2.24)). The off-state bleaching model was chosen for analysis as we have assumed that photobleaching pathways are more likely to occur from the much longer-lived triplet excited states and/or

radical intermediates, rather than from the short-lived singlet excited state; however, photobleaching pathways are generally poorly understood. It should be noted that both models agree on the fitted blinking rates in the limit $K \gg k_p$ (*i.e.* when the blinking occurs on a much faster time scale than the bleaching), as shown in the SI. The same observation was made when comparing the simplified case of a single bleaching rate with the general case, $k_{\mathrm{p}_1} \neq k_{\mathrm{p}_2}$. The data presented in this study was well fitted using a single photobleaching rate (*i.e.* k_p), however this can be easily extended to multiple bleaching rates if necessary. We also provide the photostate autocorrelation for the general case shown in Scheme 2.2 in the SI.

2.3.2 Computer simulations

We generated computer simulations of image series of blinking emitters to test the validity of our proposed analysis technique. In Figure 2.3, we show an example of an ACF computed from a simulation with its fit. Here we see the ACF is comprised of a shorter and a longer time lag decay, the former being attributed to the photoblinking and the latter to the photobleaching. This behaviour can be explained by examination of Eq. (2.16) (as mentioned previously, this is a simpler expression than the one used for fitting) where we see there are three exponentials that govern the autocorrelation decay. These exponentials have arguments $-K_p\tau$, $-K\tau$, and $-k_p\tau$. Since we usually consider $K \gg k_p$, we conclude that only the latter two exponentials contribute to the form of the complete ACF. Therefore, to get the behavior of the short-time lags we consider the limit $k_p\tau \to 0$, while for long time lags we consider $K\tau \to \infty$. Both of these limits are overlaid onto the ACF, along with its complete fit in Figure 2.3.

For accurate determination of the blinking rates, the range of time-lags to fit over should be chosen so that the blinking regime has fully decayed, and include a small segment of the bleaching regime, as the blinking and bleaching rates are both important for determining the behavior where the two regimes meet; however, we argue that fitting to longer time lags is unfavorable. One reason for this is because bleaching is a non-ergodic process, so that the ACF at higher time lags will not converge to its expected value without sufficient sampling. Additionally, an unweighted fit will place too much emphasis on the bleaching regime for longer lag-ranges, which is especially problematic when the blinking is fast *i.e.* the blinking regime is short. It should also be noted that the later lags of the sample autocorrelation in Eq. (2.20) are prone to small sampling effects, and therefore exhibit high variance and/or bias between different simulations/experiments.

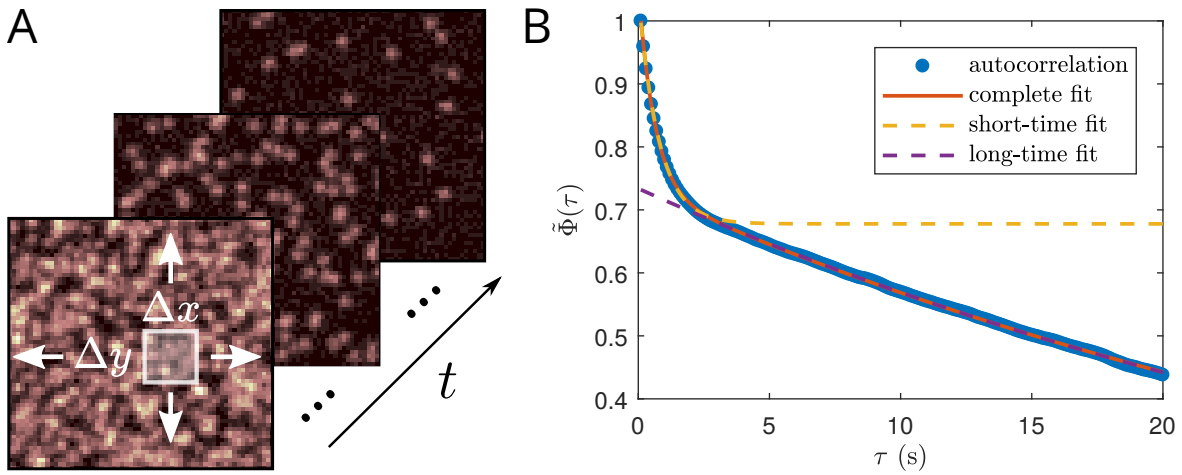

FIGURE 2.3: Example ACF computed from simulation and fit. (A) Sample simulated intensity images in time with superimposed local spatial averaging window of size $\Delta x \times \Delta y$. To get the local spatial intensity fluctuation of a pixel, we subtract the spatial mean taken from the $\Delta x \times \Delta y$ window around the pixel. This is done for each pixel over each frame. These intensity fluctuations are then used to compute the autocorrelation as in Eq. (2.20). (B) ACF and fit. ACF computed from fluorescence microscopy simulation of $T = 2,048$ frames and $N = 1,000$ molecules undergoing photoblinking and photobleaching. The short-time fit (blinking regime) represents the limiting expression as $k_p\tau \to 0$, while the long-time fit (bleaching regime) represents $K\tau \to \infty$. Simulated rates: $k_{\text{on}} = 1$ s^{-1}, $k_{\text{off}} = 0.5$ s^{-1}, $k_{\text{p}} = 0.1$ s^{-1}. Fitted rates: $k_{\text{on}} = 1.03 \pm 0.02$ s^{-1}, $k_{\text{off}} = 0.501 \pm 0.007$ s^{-1}, $k_p = (9.61 \pm 0.05) \times 10^{-2}$ s^{-1}.

Conversely, when the ACF does not exhibit a visible bleaching decay, we found it beneficial to fit to a wide time-lag range. We found this to be particularly important when dealing with STORM data (see SI for explanation). In this case, to avoid small sampling effects, the ACF should be fit up to about half of the available time-lags.

We include further examples of ACFs computed from simulation and their fits in Figure 2.9 and Table 2.5. All fits for blinking rates are within reasonable error. When the fitted lag range was increased, the photobleaching rates were recovered more accurately at the expense of less accurate photoblinking rates. Therefore, fitting over multiple timescales can provide a complete description of the photophysical/-chemical rates.

Photoblinking rates beyond camera detector sampling rate

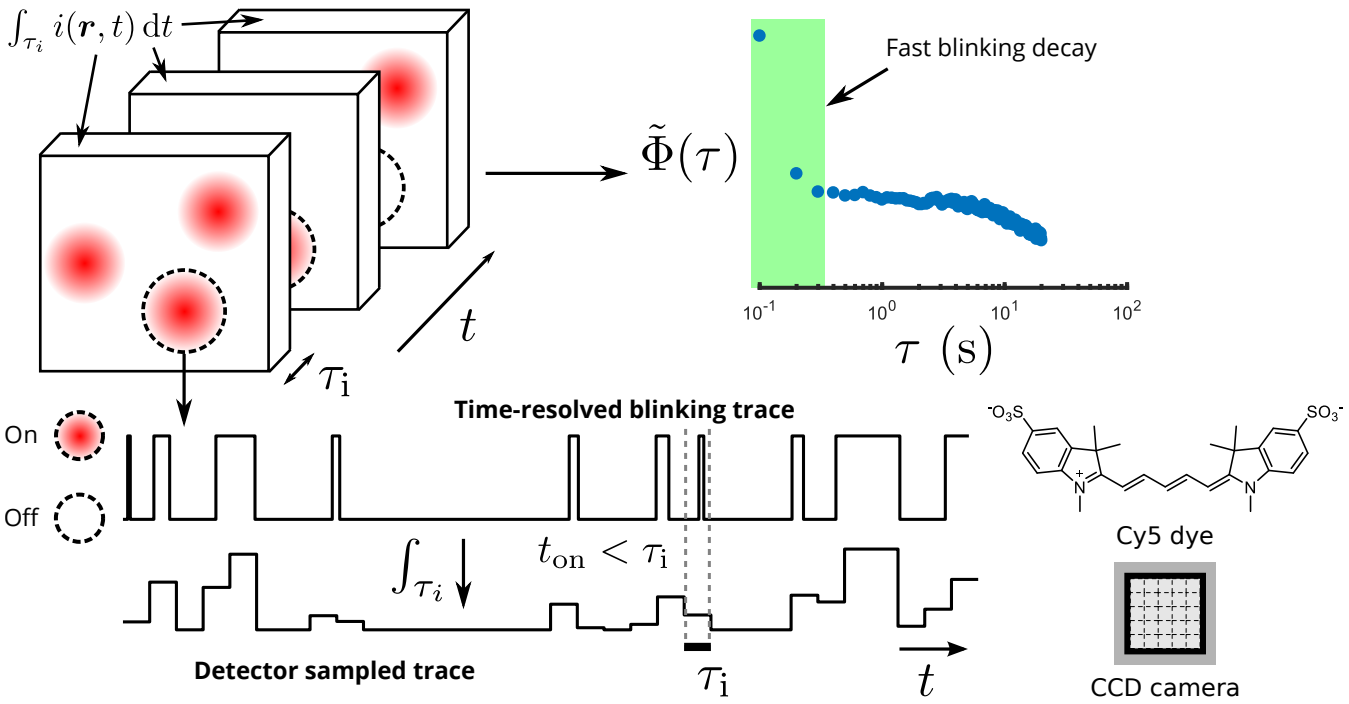

FIGURE 2.4: CCD detector time-integrated sampling of fast photoblinking trace. Blinking fluorophore (indicated within black dashed line; *e.g.* Cy5 dye) is shown with its time-resolved blinking trace (top trace) with characteristic on-time, t_on, faster than detector sampling time, τ_i, and compared with its detector integrated time trace (bottom trace). The ACF of an image series of fast blinking dyes reveals a fast blinking decay at early time lags (top right plot).

When the characteristic blinking rates of a dye are faster than the camera detector sampling rate, intensity time traces acquired using CCD cameras can still provide information about these blinking kinetics. The autocorrelation of the intensity fluctuations likewise

makes use of this information (see Figure 2.4). Autocorrelations further avoid the problem of aliasing because blinking rates that greatly exceed the detector integration time will be indicated as abrupt or absent short-time decays from which meaningful rates cannot be extracted.

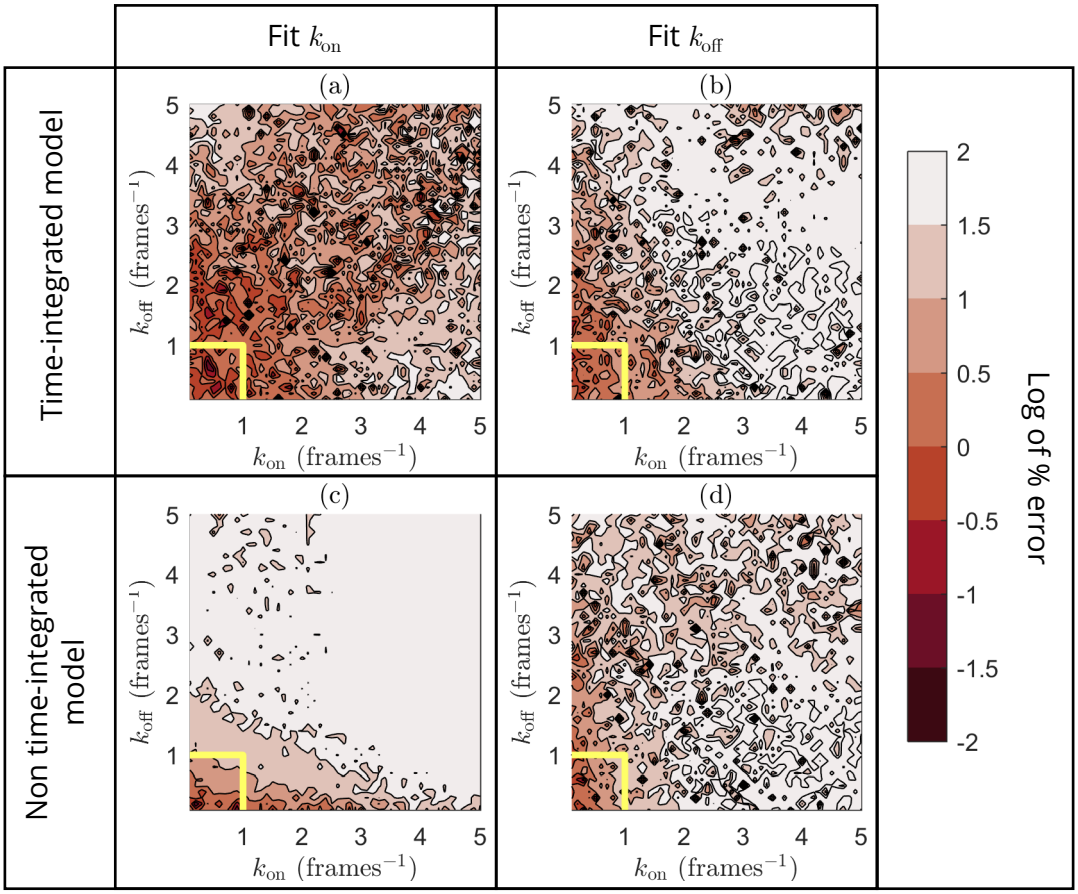

FIGURE 2.5: Comparison of fits for ACF with and without camera integration time included in the fitting function over a range of blinking rates. Figures (a) and (b) show the log of the percent error between simulated and fitted k_{on} and k_{off}, respectively, including the camera integration time in the fitting function. Similarly, figures (c) and (d) show the log of the percent error between simulated and fitted k_{on} and k_{off}, respectively, without accounting for the camera integration time in the fitting function. The region within the yellow lines represents photoblinking rates that are slower than the detector frame exposure time. The grid spacing in each of the above contour plots is 0.1 frames^{-1}. All simulations were done with $N = 50$ particles and have a fixed photobleaching rate of $k_p = 10^{-4}$ frames^{-1}. The number of frames for each simulation is chosen so that $\nu_c = 10^4$. All fits are done over the first 150 time-lags (excluding $\tau = 0$).

To demonstrate that our method can successfully recover blinking rates that are faster than detector sampling, we compare fitting ACFs from simulations with and without detector integration time included in the fitting model. To do this, we analyzed a set

of simulations over a wide range of blinking parameters and fixed bleaching rate (see Figure 2.5). Each coordinate $(k_{\text{on}}, k_{\text{off}})$ represents the fit of the ACF resulting from an average over five simulations with the same parameters. We varied the number of frames simulated for different blinking parameters, so that the expected total number of blink cycles, ν_c, is constant for every simulation (see SI). Note we obtained better results at higher blinking rates when fitting without the normalization described in Eq. (2.15); that is, we leave A as a free parameter. We believe this is due to the biased nature of ratio estimators (see for example Saffarian and Elson, 2003)[10].

From Figure 2.5, we see that there is a clear advantage in using the time-integrated fit model over its non time-integrated counterpart. The improvement is evident in the fitting of k_{on}, while the fitting for k_{off} also benefits with a slight improvement. We think that this is caused by a greater sensitivity of the fitting function to k_{on}. There also appear to be some successful fits in the upper part of the contour plot for k_{off} without time-integration, where the fits with time-integration perform worse. This is caused by a compensation for the poor fit for k_{on} in the exponential which decays as the sum of the blinking rates.

TestSTORM simulations

We also generated and analyzed simulations using TestSTORM v2.1 (see Table 2.1). To test our method under realistic conditions we added drift and an axial dimension using this simulator. In order to analyze these simulations, it is important to choose an ROI

Fitted		Simulated	
t_{on} (s)	t_{off} (s)	t_{on} (s)	t_{off} (s)
0.192 ± 0.004	1.95 ± 0.05	0.2	2
0.102 ± 0.002	3.13 ± 0.07	0.1	3
0.0302 ± 0.0006	3.9 ± 0.1	0.03	4
0.052 ± 0.001	5.1 ± 0.2	0.05	5

TABLE 2.1: Examples of ACF fits computed from TestSTORM simulations. Each simulation is generated using the predefined `star` pattern. The number of blinking particles on each arm of the star is set to $\langle N_{\text{on}} \rangle \simeq 2$/arm for the first frame. Drift type is set to the predefined `'Large'` option. All other options which are not specified are set to default. Default values include simulated camera exposure time of $\tau_i = 0.05$ s, $T = 3{,}000$ frames and $t_p = 1{,}700$ s. All fits are done over the first 300 time-lags (excluding $\tau = 0$) without photobleaching accounted for in the fit model (in each case, the bleaching regime is flat over the range analyzed).

where the density is approximately constant, as this is one of our assumptions (discussed further in the SI).

We further tested our method on the preset values supplied by the software for Alexa 568 and Alexa 647. The high fitting error produced from these results (tabulated below) is caused by insensitivity of the ACF to large changes in k_{on} in the regime $k_{\text{on}} \ll k_{\text{off}}$. We refer the reader to the STORM data section and the SI for further details.

	Fitted		Simulated	
	t_{on} (s)	t_{off} (s)	t_{on} (s)	t_{off} (s)
Alexa 568	0.025 ± 0.002	9.31 ± 0.49	0.025	9.25
Alexa 647	0.048 ± 0.002	46.3 ± 8.7	0.05	41.6

TABLE 2.2: TestSTORM simulations for Alexa 568 and Alexa 647.
Each simulation is generated using the predefined `star` pattern using the default settings of 200 single-labeled epitopes per star arm. Default values include simulated camera exposure time of $\tau_i = 0.05$ s, $T = 3,000$ frames. Default photobleaching time constants $t_p = 100,000$ s for Alexa 568 and $t_p = 1,700$ s for Alexa 647. All fits are done over the first 1,500 time-lags (excluding $\tau = 0$) without photobleaching accounted for in the fit model (in each case, the bleaching regime is flat over the range analyzed).

When multiple labels were allowed per simulated molecule, we found that we can accurately extract the sum of the blinking rates $K \equiv k_{\text{on}} + k_{\text{off}}$, however the individual rates could not be accurately resolved. This is due to the assumption of uniform labeling density being broken.

High-density simulations

A clear advantage of using our method over single-molecule techniques is the power to quickly analyze dense regions of fluorophores without having to localize any single molecules. This is particularly relevant for SMLM super-resolution methods characterized by high labeling densities. Furthermore, single-molecule techniques fail when there exists too much spatial overlap between simultaneously emitting fluorophores, as it becomes impossible to isolate enough single particle intensity traces needed for extracting the blinking rates.

We demonstrate this through simulations by varying the average effective fraction per image occupied by fluorophore PSFs, ρ_{eff}, which is computed as,

$$\rho_{\text{eff}} \equiv \langle \Theta_t \rangle \langle n_p \rangle, \text{ where } \langle n_p \rangle \equiv N \times \frac{\text{Eff. PSF Area}}{\text{Sample Area}}. \tag{2.17}$$

This quantity accounts for the expected number of dyes that are emitting in every frame, as well as the PSF size from each of these dyes. As our simulations assume a Gaussian PSF, we calculate the effective PSF area as

$$\text{Eff. PSF Area} = \pi\omega_0^2, \tag{2.18}$$

where ω_0 is the e^{-2} PSF radius. We considered 4 different values for ρ_{eff}, specifically 0.1, 0.5, 10 and 100. For values greater than $\rho_{\text{eff}} = 0.1$, we could not acquire enough isolated single-molecule intensity time traces to perform a single-molecule analysis. Note our model and simulations do not account for high-density interactions between simulated fluorophores, such as self-quenching and homo-FRET.[11, 12] These effects would define an upper density-limit in our analysis of experimental data. We summarize the results from these simulations in Table 2.3 below.

	Autocorrelation		Single-molecule	
ρ_{eff}	t_{on} (s)	t_{off} (s)	t_{on} (s)	t_{off} (s)
0.1	9.3 ± 0.2	0.99 ± 0.01	9.5 ± 1.0	1.03 ± 0.10
0.5	10.3 ± 0.1	0.99 ± 0.01	—	—
10	10.7 ± 0.1	0.995 ± 0.006	—	—
100	10.44 ± 0.04	1.005 ± 0.004	—	—

TABLE 2.3: Analysis of simulations with varying densities.
All simulations have characteristic blinking times of $t_{\text{on}} = 10$ s and $t_{\text{off}} = 1$ s. Camera exposure time simulated as $\tau_i = 0.1$ s for $T = 3,000$ frames. photobleaching was not included in these simulations. ACF fits were done over the first 100 time-lags (excluding $\tau = 0$).

In the simulation with $\rho_{\text{eff}} = 100$, $N = 45,000$ simulated fluorophores, each with simulated e^{-2} PSF radius of 1.7 pixels, were uniformly distributed in a 64×64 pixel grid. The high-densities successfully analyzed by our technique far exceed those that can be analyzed using a single-molecule approach, as demonstrated in Table 2.3.

2.3.3 Experimental data

Addition of Ni^{2+} to DNA-Cy5 system

We next tested our method on surface-tethered DNA-Cy5 complexes in the presence of different concentrations of Ni^{2+} ions, which can effectively quench the triplet excited state of Cy5 and avoid the subsequent formation of long-lived transient radicals[13]. We again benchmark the results from our technique using single-molecule analysis. It is worth

mentioning that in order to exclude the possibility of overfitting when handling real data, we recommend carrying out our method on at least two independent ROIs. Figure 2.6, along with Table 2.4, show analysis results from both techniques at two different Ni^{2+} concentrations. The fitted photoblinking times are in good agreement with each other for $[Ni^{2+}] = 1.0$ mM.

When the concentration of Ni^{2+} was reduced, we observed a significant decrease in the proportion of the on-times from both analysis techniques, in line with previous studies[14]. This was expected since the triplet-state of Cy5 is quenched by the Ni^{2+}, but has a lifetime that is too short to be probed at our acquisition rates. The observed dark-state is likely from a long-lived radical state of Cy5, which is unaffected by Ni^{2+} concentrations and has a longer lifetime.

	Autocorrelation		Single-molecule	
$[Ni^{2+}]$ (mM)	t_{on} (s)	t_{off} (s)	t_{on} (s)	t_{off} (s)
1.0	20.6 ± 1.9	0.285 ± 0.017	21.4 ± 2.1	0.301 ± 0.025
0.2	1.28 ± 0.23	0.076 ± 0.008	3.44 ± 0.31	0.197 ± 0.013

TABLE 2.4: Comparison of fitted photoblinking values from analyses shown in Figure 2.6.

Fitted photoblinking times are in good agreement when $[Ni^{2+}] = 1.0$ mM. The difference in fitted rates when $[Ni^{2+}] = 0.2$ mM arises from aliasing in the single-molecule analysis due to fast blinking rates. Computed p-values from $[Ni^{2+}] = 1.0$ mM on-/off-time histograms using χ^2 goodness-of-fit (expected distribution assumed to be geometric) were $\sim 10^{-6}$ and ~ 0.3, respectively; and ~ 0.02 for both $[Ni^{2+}] = 0.2$ mM histograms. The poor p-value for the fit of the on-time when $[Ni^{2+}] = 1.0$ mM is likely due to the simplified assumption of a two-state model. Three independent ROIs were used for the ACF analysis of the 0.2 mM data; tabulated results are averaged fitted values from these ROIs. Additional parameters: $\tau_i = 0.1\ s$, $T = 7,990$ frames (1.0 mM), $T = 2,359$ frames (0.2 mM).

The computed ACF when the concentration of Ni^{2+} was reduced from 1.0 mM to 0.2 mM also exhibited a quick short-time decay (see Figure 2.6), which suggests fast photoblinking dynamics. The fitted ACF (see Table 2.4) shows that the characteristic photoblinking off-time is beyond the sampling frequency of the camera detector.[1] This finding is not corroborated by our single-molecule analysis, however. We explain this observation by arguing that while our autocorrelation method uses the full intensity information, the single-molecule analysis requires binarization of the single-molecule intensity time traces in order to extract blinking rates so that short blinking events are

[1] Errors on fitted blinking times were high when analysis was done on a single ROI due to the small number of points in the blinking regime; therefore, three independent ROIs were analyzed to get blinking time estimates, in this case.

missed. This limits the single-molecule analysis to photoblinking dye systems that are slower than detector exposure times.

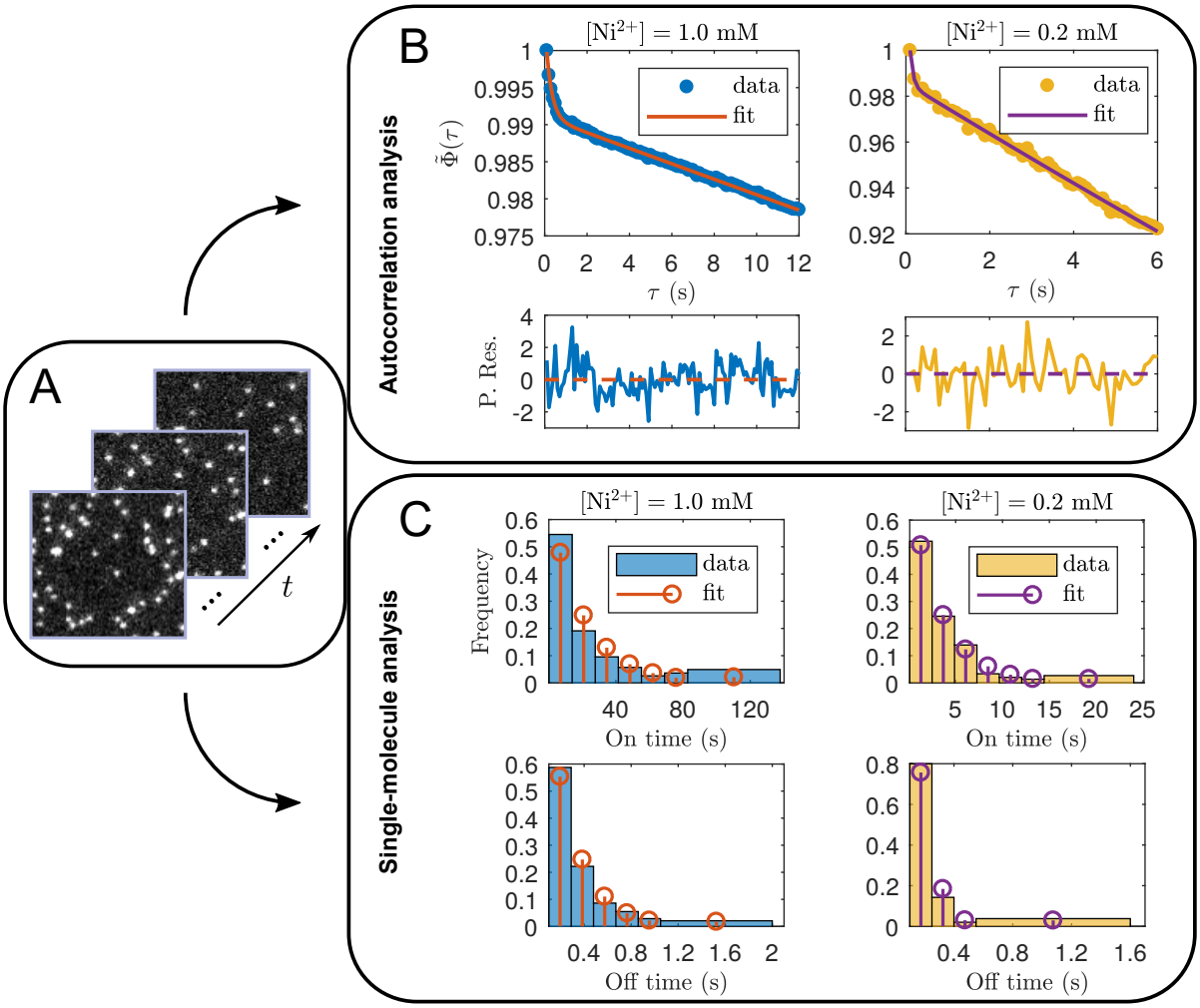

FIGURE 2.6: Comparison of autocorrelation and single-molecule analyses for probe blinking data imaged at different Ni^{2+} concentrations. (A) Sample fluorescence intensity images (contrast adjusted) from experiment of surface-tethered DNA-Cy5 duplexes. (B) ACFs computed from data and fits (top); Pearson residuals (bottom). (C) Histograms of observed on- and off-times from single-molecule analysis, overlaid with expected distributions. Assumed underlying distribution is geometric with best-fit parameter from maximum-likelihood estimation (MLE).

We confirm this hypothesis through simulation with photophysical/-chemical parameters chosen to be similar to the ones recovered using our autocorrelation method in Table 2.4 at $[Ni^{2+}] = 0.2$ mM. The analysis of the simulation is shown in Figure 2.7. In this figure, we see that both blinking times extracted using the single-molecule analysis are inconsistent with the simulated ones. Both recovered times were also inconsistent with our method in the analysis of the faster blinking data, as shown in Table 2.4.

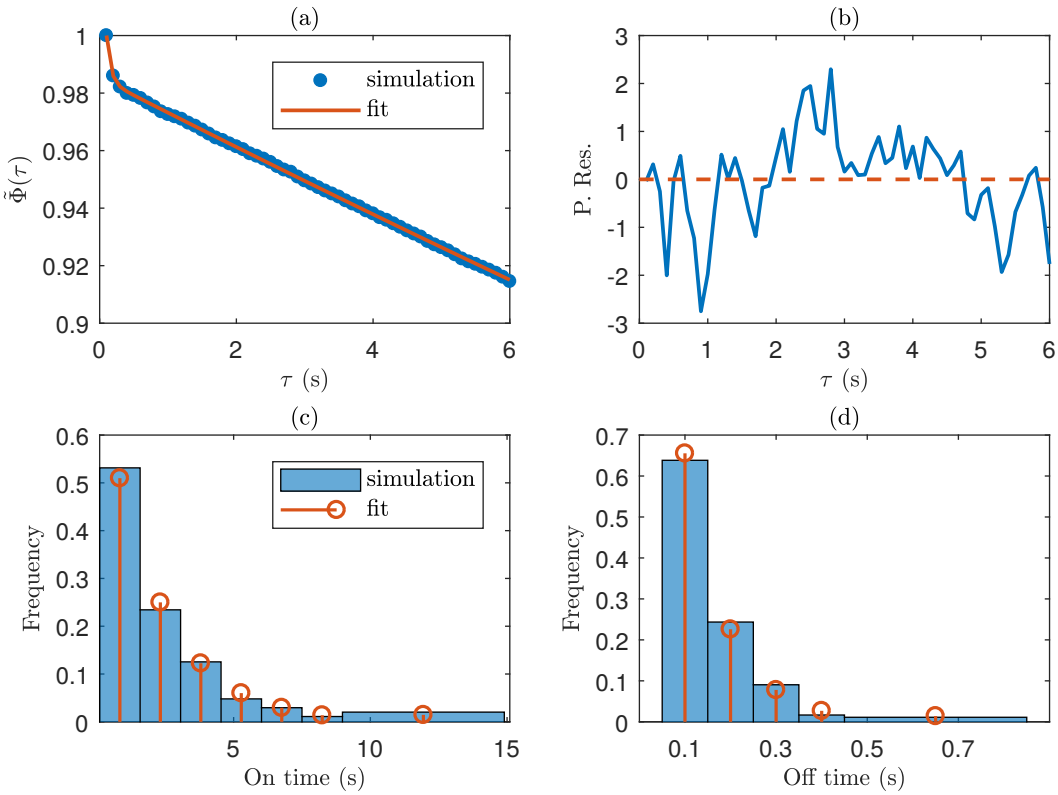

Autocorrelation		Single-molecule	
t_{on} (s)	t_{off} (s)	t_{on} (s)	t_{off} (s)
0.94 ± 0.25	0.066 ± 0.008	2.15 ± 0.18	0.153 ± 0.008

FIGURE 2.7: Comparison of autocorrelation and single-molecule analyses on a rapid photoblinking simulation. Simulated on-off times are similar to the ones extracted from the $[Ni^{2+}] = 0.2$ mM data using our autocorrelation method (shown in Table 2.4). (a) ACF and fit. (b) Pearson residuals from (a). (c) and (d) histogram of observed on- and off-times, respectively, overlaid with expected distributions. Assumed underlying distribution is geometric with best-fit parameter from MLE. p-values from χ^2 goodness-of-fit were computed to be ~ 0.6 and ~ 0.2 in (c) and (d), respectively. Simulation parameters: $t_{on} = 1$ s, $t_{off} = 0.067$ s, $t_p = 4$ s, $T = 2,048$ frames, $N = 170$, $\tau_i = 0.1$ s.

Note that the times output by the single-molecule analysis are also consistently higher than the ones extracted measured by our method. This is because the very short off-time events are missed by the single-molecule analysis, leading to an overestimation of both t_{on} and t_{off}. This is an expected result from aliasing in the single-molecule analysis, which is not present in our autocorrelation analysis. Furthermore, the problem of aliasing is avoided altogether by using an autocorrelation because if the blinking is too fast, the autocorrelation would not exhibit a short-time blinking decay, thus indicating that a fit for the photoblinking would not be accurate.

STORM data

We now discuss the applicability of our method in the regime $k_{on} \ll k_{off}$. To do this we analyzed the stochastic blinking of Cy5 in the presence of beta-mercaptoethanol (β-ME), imaged under diferent laser intensities. Low densities of Cy5 were used in order to compare with single-molecule analysis. Analyses of two separate data sets are shown in Figures 2.10 and 2.11. In Figure 2.10, our results are consistent with the single-molecule analysis, while in Figure 2.11 only t_{on} was reasonably recovered. k_{off} (recall, $k_{off} = 1/t_{on}$) was accurately recovered in both instances because it is effectively responsible for the decay in the ACF when $k_{on} \ll k_{off}$. The inconsistency in the recovered values for k_{on} between both analyses in Figure 2.11 can be explained by insufficient sampling in the chosen ROI. These results suggest that single-molecule techniques require less sampling to correctly recover blinking rates in the regime $k_{on} \ll k_{off}$ in comparison with our method. However, since our technique can quickly analyze high-density dye systems, acquiring sufficient sampling is not a problem as demonstrated in Figure 2.8, where we show the fitted k_{on} value from the ACF converges to the simulated value with increasing number of sampled blinking particles. Nevertheless, high labeling densities are required for achieving high spatial resolutions relevant in SMLM methods, as demonstrated in the same figure. Recall that our method requires an ROI with randomly positioned labels; for example, our autocorrelation analysis can successfully extract the sum of the blinking rates in samples with multiple labels per molecule, but cannot resolve both rates individually. We also point out that at very high densities when fluorophores are separated by distances smaller than typical Förster radii, self-quenching and homo-FRET can occur. So care should be exercised to verify that quenching is not present at these high densities, or a lower surface density should be used.

We show in the SI that more sampling is required with increasing k_{off}/k_{on} from simulation when using our method (see Figure 2.16). This is consistent with our results in Figures 2.10 and 2.11. To ensure sufficient sampling, one can plot the fitted k_{on} values as a function of number of frames and check for convergence. The large errors on t_{off} from the single-molecule analyses in Figures 2.10 and 2.11 are due to the restriction that we required both techniques be analyzed within the same ROI, rather than the entire image series. This is also due to long blink cycles in these datasets, leading to fewer events.

To accurately perform our analysis in this regime, we found it necessary to first divide out the non-uniform background from the image series. This is because we did not account for non-uniform laser excitation in our method. Although this effect does not usually bias the blinking rates extracted using our method, given we only performed our analyses on

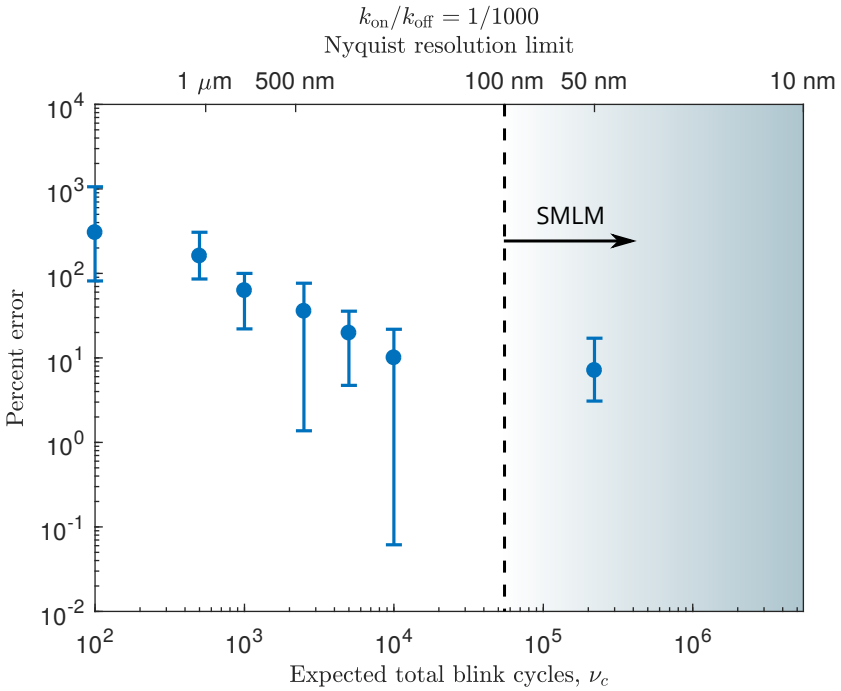

FIGURE 2.8: Percent error on ACF fit for k_{on} as a function of expected total blink cycles, ν_c (bottom axis), and Nyquist spatial resolution limit (top axis). Gradient demonstrates spatial resolutions which are of relevance in SMLM super-resolution methods. Each point represents the average fitted k_{on} value from 5 independent simulations, while error bars represent the minimum and maximum percent errors over the 5 simulations. To vary ν_c, T was fixed while N was varied across simulations. Analysis was done on a 45×45 pixel ROI in the center of each simulated image series. Simulated image series were background corrected before analysis. All fits are done over the first 2,000 time-lags (excluding $\tau = 0$). Simulation parameters: $T = 4,096$ frames; $t_{on} = 0.05$ s; $t_{off} = 50$ s; laser e^{-2} beam radius, $\Omega_0 = 64$ pixels; $k_p = 2 \times 10^{-3}$ s; 100 nm pixel size (dashed vertical line).

ROIs, small changes in the ACF cause significant variations in recovered k_{on} values when $k_{on} \ll k_{off}$ (see SI for more details). We used the predefined `movmean` function in MATLAB with a 10×10 pixel sliding window on each frame of the image series to approximate the background, which we then divided from each corresponding frame of the original image series. Furthermore, since we need to rely on the part after the blinking decay in the ACF to recover k_{on}, we choose to fit to a wider time-lag range.

2.3.4 Comparison with other methods

Several other studies have examined photophysical/-chemical properties of a system using autocorrelation methods[15, 16]. For instance, Widengren *et al.* (1995)[17] showed that FCS can be used to recover photophysical/-chemical parameters while simultaneously characterizing the diffusion and density of fluorescent dyes. Point FCS data are sampled at much shorter binning times than possible with widefield imaging and thus can resolve faster processes. Although similar high time resolutions are not possible to achieve with widefield microscopy, we presented a theoretical correction to the autocorrelation in order to push the capability to extract blinking rates that lie beyond the sampling frequency of the detector when increasing time-resolution is not an option. Furthermore, in FCS the non-uniform illumination in the confocal spot must be accounted for, which can render the mathematics to be relatively complex. Spatial non-uniformity can usually be mitigated in widefield data by choosing appropriate ROIs, where excitation intensity can be assumed to be uniform. There also exist techniques for achieving flat laser illumination profiles in widefield setups[18]. Moreover, the lack of spatial information in FCS means additional data is required to fully determine the on-off blinking rates and multi-point experiments are needed if rates vary in space. We have shown in this work that defining the intensity fluctuations through spatial mean subtraction yields an autocorrelation expression that can be fit for k_{on}, k_{off} and k_p, simultaneously. Conversely, in the SI we show that defining the fluctuations through temporal mean subtraction (as is done when spatial information is not available, *e.g.* FCS) results in an autocorrelation expression that cannot be simultaneously fit for both k_{on} and k_{off}. Processes with similar fluorescence behavior to photoblinking have also been studied using FCS, such as Förster resonance energy transfer (FRET)[19, 20] and binding/unbinding to a surface under total internal reflection fluorescence (TIRF) illumination[21].

Balanced super-resolution optical fluctuation imaging (bSOFI), an extension of SOFI developed by Geissbuehler *et al.* (2012)[22], offers a way to obtain super-resolved spatial maps of the molecular brightness, on-time ratio and molecular density. By computing a

temporal autocorrelation, the authors were also able to extract spatial maps of k_{on} and k_{off}. The authors further indicate that their technique can be extended beyond simple two-state systems. As we have assumed uniform molecular density and brightness, the difference between the two techniques is that our method holds only in a local region (*i.e.* in an ROI). However, spatial maps can also be extracted using our method simply by analyzing a collection of ROIs. Also, bSOFI assumes knowledge of the PSF and relies on solving systems of equations of coupled molecular parameters. Our method is solely dependent on the photophysical/-chemical parameters and does not require extraction of any other parameters intrinsic to the system. Moreover, bSOFI does not address the effects of photobleaching which are usually present.

Previous works have also tackled the problem of resolving events that are faster than the exposure time of camera detectors. Super temporal-resolved microscopy (STReM)[23] is a technique relying on PSF engineering through rotating phase masks which was successfully used to study processes up to 20 times faster than detector exposure times.

Autocorrelations have also been utilized to extract photophysical/-chemical properties in a single-molecule context.[24] Haase *et al.* (2004)[25] have previously reported that it is possible to extract triplet lifetimes as short as half the binning time of a single photon avalanche photodiode using histogram or autocorrelation methods on fluorescence collected from a single dye; however, this was found to require long intensity time traces (so that this analysis would not be possible with moderate photobleaching rates), while the on-time could not be correctly recovered simultaneously by either method when the triplet state was very short-lived compared to the "on"-state. Single molecule autocorrelation methods have also been useful for accurately analyzing power-law blinking kinetics of quantum dots[26].

Single molecule analysis techniques typically require hours of processing and are hard to automate when many dyes need to be localized. Conversely, the technique we have developed in this work does not require long computation times, or involved user input. In Figure 2.12, we show the time taken to compute the autocorrelation defined in Eq. (2.20) for varying image series sizes, which is the most time-consuming step in our method for larger image series. From this figure one can see autocorrelation computation is on the order of seconds, with the longest computation time taking about five minutes to be computed (for a 512×512 pixel, $4,096$ frame image series). For large image series, computation times can be even further reduced by utilizing parallel computing (see GitHub code).

2.4 Conclusions

We have presented an autocorrelation method that that can rapidly extract photophysical/-chemical rates from a fluorescence image series in a single fit. Furthermore, this fit is solely dependent on photophysical/-chemical parameters and does not rely on knowledge of other system parameters. This has potential applications in SMLM because it can be utilized for high-throughput screening of blinking fluorescent probes, as well as for testing photo-stabilization approaches. We have also shown that we can recover rates that are faster than CCD camera integration times by fitting a theoretical model for the ACF of the time-integrated intensities. We demonstrated this with both simulation and experimental data. Autocorrelations also have the advantage of avoiding aliasing when the blinking rates are too fast, as was discussed. Moreover, we have successfully analyzed high-density blinking fluorophore simulations, which could not be analyzed using standard single-molecule image analysis. We further found that given sufficient sampling, our method can successfully recover the correct photophysical/-chemical rates from STORM super-resolution data. In future work, we hope to quantify the amount of sampling required to successfully analyze this type of data. This can be done by theoretical calculations of the bias and variance of the ACF.

2.5 Methods/Experimental

Materials

$NiCl_2 \cdot 6H_2O$ salt, glucose oxidase type VII from Aspergillus niger (G2133), catalase from bovine liver (C30), and β-mercaptoethanol were purchased from Sigma. Water (molecular biology grade) was acquired from Thermo Scientific HyClone. 5 M NaCl stock solution and streptavidin were purchased from Life Technologies. Tris-HCl (pH 7.5 and 8.0) buffer was acquired from Fisher Scientific. Poly(ethyleneglycol) Silane, MW 5000 (mPEG-Sil) and biotin-PEG-Sil were purchased from Laysan Bio Inc. 10x PBS buffer (1.37 M NaCl, 27 mM KCl, 80 mM NaH_2PO_4, 20 mM K_2HPO_4, pH 7.4) was obtained from Life Technologies. Dye-labeled and biotinylated DNA oligonucleotides used in this study (Table 2.6) were acquired from Integrated DNA Technologies and purified by HPLC by the provider. All other materials were used without further purification.

Single molecule sample preparation and surface immobilization

Imaging in the presence of nickel ions

The glass coverslips for single-molecule imaging studies of Cy5-DNA in the presence of Ni^{2+} were prepared as previously described[14]. Glass coverslips (Fisher scientific) were first cleaned in piranha solution (25% H_2O_2, 75% conc. H_2SO_4 by volume) for 1 h and then rinsed with water and HPLC grade acetone 3 times. Clean coverslips were then amino silanized with Vectabond/acetone 1% solutions for 5 min. They were then rinsed with water and dried under a nitrogen stream. The coverslips were passivated with a mixture of poly(ethylene glycol) succinimidyl valerate (mPEG-SVA, MW = 5000) and biotin-PEG-SVA. More specifically, the coverslips were masked with patterned silicone films (Grace, Bio-Labs) and the unprotected area was incubated with 25% w/w m-PEG-SVA solution containing 0.25% w/w biotin-PEG-SVA in 0.1 M sodium bicarbonate solution for 3–4 h. The silicone templates were removed, and the excess PEG rinsed with water.

STORM imaging

The glass coverslips for STORM studies were initially cleaned and then passivated in one step utilizing PEG-Silane as previously described.[27] A mixture of poly(ethylene glycol) silane, MW 5000 (PEG-Sil) and Biotin-poly(ethylene glycol) silane (bio-PEG-Sil) at a ratio of 99/1 (w/w) was used. Imaging chambers (~ 8 μL) were constructed by pressing a polycarbonate film with an adhesive gasket onto a PEG-coated coverslip. Two silicone connectors were glued onto the predrilled holes of the film and served as inlet and outlet ports.

Single molecule sample preparation and surface immobilization

Before image acquisition, the surface was incubated with 12 μL of 0.2 mg/mL streptavidin solution for 10 min. The unbound streptavidin was washed away with imaging buffer. Following streptavidin incubation, biotinylated DNA-Cy5 complexes were immobilized on PEG-coated glass coverslips *via* biotin-streptavidin interactions upon incubating a 100 pM solution of the construct. Unbound complexes were flushed out with additional imaging buffer.

TIRF microscopy and imaging

Imaging in the presence of nickel ions

Single-molecule measurements were performed using an objective-based total internal reflection fluorescence (TIRF) microscope (Olympus IX-71 inverted microscope) equipped with laser-based TIRFM illumination module (IX-RFAEVA-2, Olympus) coupled to a diode pumped solid-state red laser (641 nm, CrystaLaser). The beam position was adjusted using a TIRFM illuminator to achieve total internal reflection through an oil-immersion objective (NA 1.45, Olympus PLAN APO N 60X). For Cy5 imaging, the excitation was directed by a beam splitter (FF660-Di01-25 × 36, Brightline Semrock) and filtered with two emission filters before the detector (HQ 685/70 and HQ 685/80, Chroma Technology). Fluorescence from the surface immobilized molecules was collected by the same objective and imaged onto the chip of the electron-multiplying CCD (EMCCD) detector (Cascade II: 512, Roper Scientific). An additional 2× magnification was achieved by a relay lens placed between the camera and the microscope. Emission was chromatically separated using a dichroic mirror (640dcxr, Chroma Technology) with the 'green' and 'red' channels each imaged on half the EMCCD chip. Images consisted of a region *ca.* 35 μm × 70 μm, (*ca.* 135 nm/pixel). The acquisition was controlled by μ-Manager software (freely available) capturing 16-bit 512 × 512 pixel images with an exposure time of 100 ms, a conversion gain of 3, and multiplication gain of 4095. Excitation was carried out with a power output of 5.0–6.5 mW measured out of the objective.

STORM imaging

Fluorescence imaging was carried out using an inverted Nikon Eclipse Ti microscope equipped with the Perfect Focus System (PFS) implementing an objective-type TIRF configuration with a Nikon TIRF illuminator and an oil-immersion objective (CFI SR Apo TIRF 100× Oil Immersion Objective Lens, numerical aperture (NA) 1.49). The effective pixel size was 160 nm. A 647 nm laser was used for excitation (Agilent MLC400B Monolithic Laser Combiner). For Cy5 imaging, the laser beam was passed through a multiband cleanup filter (ZET405/488/561/647×, Chroma Technology) and coupled into the microscope objective using a multiband beam splitter (ZT405/488/561/640rpc, Chroma Technology). For Cy5, fluorescence light was spectrally filtered with a (ET705/72m, Chroma Technology) emission filter. All images series were recorded onto a 512 × 512 pixel region of a back-illuminated EMCCD camera (iXon X3 DU-897-CS0-#BV, Andor Technology). The camera was controlled using Micro-Manager Software (Micro-Manager 1.4.13, San Francisco, CA, USA).

Anti-fading solution

To increase Cy5 photostability, all experiments were carried out under a constant flow of an oxygen scavenger solution consisting of D(+)glucose 0.8–3.0% w/v and glucose oxidase type VII (165 units/mL) 0.04 mg/mL (1600 units/mL) catalase. For STORM imaging, solutions were 20 mM in TRIS buffer pH 8.0, 50 mM in NaCl, and 146 mM in 2-mercaptoethanol. Imaging under 0.2 and 1.0 mM Ni^{2+} ions was performed under the buffer conditions specified in Table 2.7. The imaging solution was injected through one of the ports and incubated for at least 10 min to allow the equilibration of the oxygen concentration in the chamber. All experiments were conducted at room temperature (23 °C).

Computer simulations

All individual simulations were generated and analyzed using MATLAB R2017a on a Dell XPS 9530 (Intel(R) Core™ i7 @ 2.3 GHz, 16 GB RAM) running Windows 10. All phase-space analyses were also generated using MATLAB R2017a on a dedicated research server (Intel(R) Core™ i7 @ 3.2 GHz, 16 GB RAM) running Ubuntu version 18.04.

To simulate fluorophore movies, we randomly distributed point emitters on a pixel grid with specified number of frames. We proceeded to convolve the generated image series with a 2D Gaussian function (integrated over pixel dimensions) to simulate the optical PSF. To model photoblinking and bleaching of the simulated emitters we used the Gillespie algorithm[28]. The rate diagram in Scheme 2.2 represents the photophysical/-chemical process that we simulated. In all simulations we assume photobleaching only occurs from the off-state *i.e.* $k_{\mathrm{p}_1} = 0$ and $k_{\mathrm{p}_2} = k_{\mathrm{p}}$. For each time frame of the simulated image series, the average number of counts from a simulated emitter is proportional to the integral of its photostate over the frame time. For more simulation details, we refer the reader to the SI.

To assign intensity values to the pixels we used an EMCCD model proposed by Hirsch *et al.*[29] We drew numbers from a Poisson distribution, with rate parameter being a function of pixel location, $\boldsymbol{x}$, and frame number, f, as described by the equation below,

$$n(\boldsymbol{x}, f) = (n_{\mathrm{s}}(\boldsymbol{x}, f) + n_{\mathrm{afl}})Q_d L(\boldsymbol{x}) + n_{\mathrm{dn}} + n_{\mathrm{cic}}, \tag{2.19}$$

where $n_{\mathrm{s}}(\boldsymbol{x}, f)$ is the counts from the simulated emitters at pixel $\boldsymbol{x}$ and frame f; n_{afl} and n_{dn} are the counts for the simulated auto-fluorescence and dark noise, respectively; n_{cic} is number of counts for the simulated clock-induced charge; Q_d is the value used to model

the quantum yield of the detector; and $L(\boldsymbol{x})$ is the simulated laser illumination profile. We then proceeded to simulate EM gain and readout noise.

The computed ACFs were fit using Eqs. (2.15) and (2.24) assuming again that photobleaching occurs exclusively from the off-state (see SI for more details). When the photobleaching was not apparent in the ACF, we simply used the same fit model in the limit where $k_p \to 0$.

The fitting of the ACFs for obtaining photophysical/-chemical parameters was done using the built-in MATLAB function `nlinfit`. The errors were subsequently computed using the built-in MATLAB function `nlparci`. We used uniformly drawn random numbers in the interval $(0, 1)$ as initial guess parameters for the blinking rates, in order to demonstrate the robustness of our method. When the photoblinking rate is also a fitting parameter, we have found that the initial guess must be small in order for the fit to converge. We consistently used 10^{-4} as an initial guess for k_p. Note we have discarded the 0^{th} time-lag from all the fits presented in this work as it includes white-noise.

Autocorrelation computation

The autocorrelation was calculated as,

$$\widehat{\Phi}(\tau) = \frac{1}{XY}\sum_{x=1}^{X}\sum_{y=1}^{Y}\frac{1}{T-\tau}\mathcal{F}_t^{-1}\left(|\mathcal{F}_t(\delta_{\Delta x\times\Delta y} i(x,y,t))|^2\right), \tag{2.20}$$

where X and Y are the number of pixels along each dimension in the image ROI and $\mathcal{F}_t$ is the fast Fourier transform in time. $\delta_{\Delta x\times\Delta y}$ denotes the local spatial fluctuation at pixel (x, y) *i.e.* we subtract the mean of a rectangular region centered on pixel (x, y) of dimensions $\Delta x \times \Delta y$ from the number counts at pixel (x, y) (see MATLAB function `movmean` for details). We choose to define the fluctuations this way in order to deal with spatial non-uniformity in the intensity, which was not accounted for in the theory of this work. We set $\Delta x = \Delta y = 10$ pixels. Ideally, the size of the local rectangular region being subtracted should be slightly bigger than the e^{-2} radius of the PSF. To further mitigate the effects of non-uniformity in the analysis of our experimental data, we chose to do our analyses on ROIs. For small ROIs, we replaced the local spatial mean subtraction by a global one. When analyzing our simulations, the autocorrelations were computed on the entire pixel grid, unless specified otherwise. The ACF was computed by dividing Eq. (2.20) by $\widehat{\Phi}(\tau = 1)$. Note that the above equation utilizes the Wiener-Khinchin theorem to minimize the computation time *via* Fourier (reciprocal) space calculations.

Single-molecule analysis

Fluorescence intensity-time trajectories of individual molecules were extracted from the videos using a self-written algorithm in MATLAB. The same was done in the analysis of the simulated fluorescence image series. On-off transitions for the Cy5 + Ni^{2+} system were investigated through the application of hidden Markov modeling (HaMMy) using the software provided by the Ha lab[30]. On-off transitions for the Cy5 + β-ME system were investigated through the application of a threshold. Background signal was fitted to a Gaussian function. Intensities above 5 standard deviations from the center of the background signal were considered on-state peaks.

Additional Content

- The Supporting Information is available free of charge on the ACS Publications website.

  Autocorrelation analysis of additional simulations; STORM data analysis comparisons; autocorrelation computation times; additional methods data; derivation of photostate autocorrelation; autocorrelation of temporal fluctuations; simulation details; comparison of different photo-bleaching models; expected total number of blinking cycles derivation; further discussion of STORM data; autocorrelation analysis with non-uniform densities; comparison between local and global spatial mean subtraction; ROI selection

- We will maintain a GitHub repository with analysis and simulation codes relevant to this study at `https://github.com/ssehayek/blink-project.git`.

Acknowledgment

P.W.W. kindly acknowledges support of a Natural Sciences and Engineering Research Council of Canada (NSERC) Discovery Grant.

G.C. is thankful to NSERC, the Canadian Foundation for Innovation (CFI), the Fonds de Recherche du Québec - Nature et Technologies (FRQNT), and the Canada Institute for Health Research (CIHR) for funding. V.G. and Y.G. are thankful to the Drug Discovery and Training Program and NSERC CREATE Bionanomachines programs for postgraduate scholarships. V.G. is also thankful to Groupe de Recherche Axé sur la Structure

des Protéines (GRASP) and Y.G. is also thankful to the Drug Discovery and Training Program (CIHR) and Vanier Canada, for postgraduate scholarships.

H.B.B. is supported by the NSERC CREATE Bionanomachines graduate scholarship and also in part by an NSERC CGS-M.

P.F. is supported by a Simons Investigator in Mathematical Modelling of Living Systems grant, an Integrated Quantitative Biology Initiative grant, Regroupement Québecois sur les matérieux de Pointe, and an NSERC Discovery Grant.

We would also like to thank C. Shaheen for very helpful discussions.

2.6 Supporting Information

Supplementary figures and tables

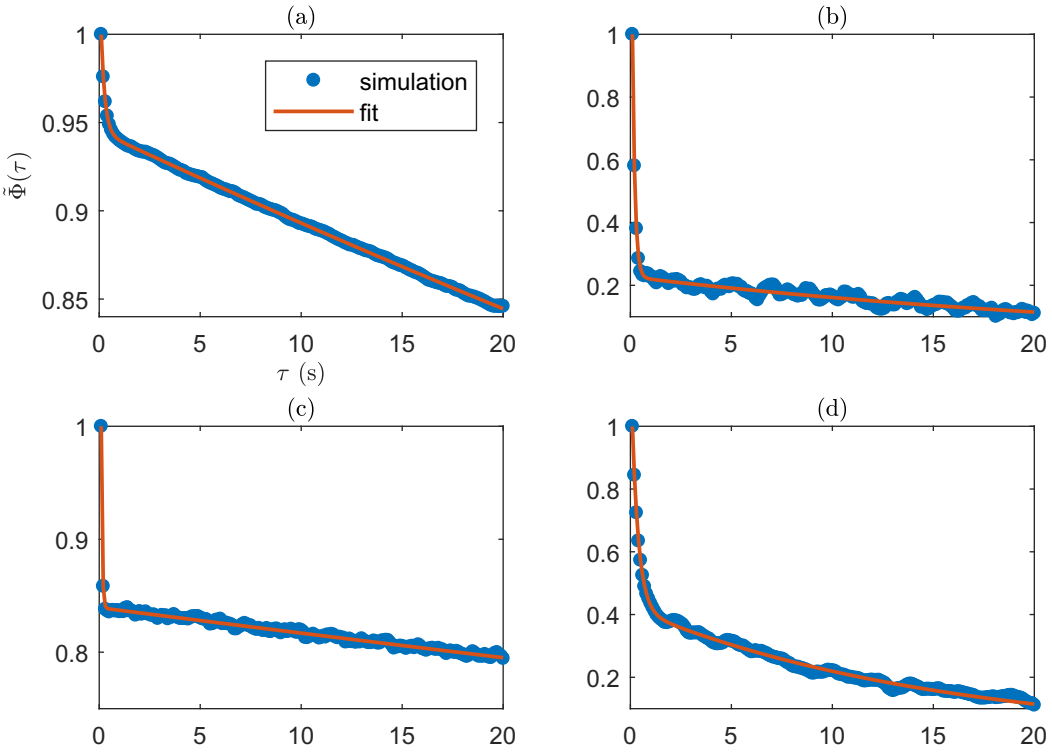

FIGURE 2.9: Autocorrelation analysis of fluorescence microscopy simulations and their fits ($N = 100$, $T = 2,048$ frames and $\tau_i = 0.1$ s for all simulations). All fits are done over the first 200 time-lags (excluding $\tau = 0$). Simulation and fit parameters are given in Table 2.5.

	Fitted			Simulated		
Figure	k_{on} (s^{-1})	k_{off} (s^{-1})	k_p (s^{-1})	k_{on} (s^{-1})	k_{off} (s^{-1})	k_p (s^{-1})
(a)	4.8 ± 0.1	0.49 ± 0.02	$(9.7 \pm 0.1) \times 10^{-2}$	5	0.5	0.1
(b)	0.97 ± 0.03	7.0 ± 0.4	$(4.5 \pm 0.2) \times 10^{-2}$	1	7	0.05
(c)	10.1 ± 0.2	11.4 ± 1.4	$(8.9 \pm 0.5) \times 10^{-3}$	10	10	0.01
(d)	1.02 ± 0.04	2.05 ± 0.08	0.106 ± 0.002	1	2	0.1

TABLE 2.5: Corresponding fitted values for the simulated photoblinking and bleaching rates from Fig. 2.9.

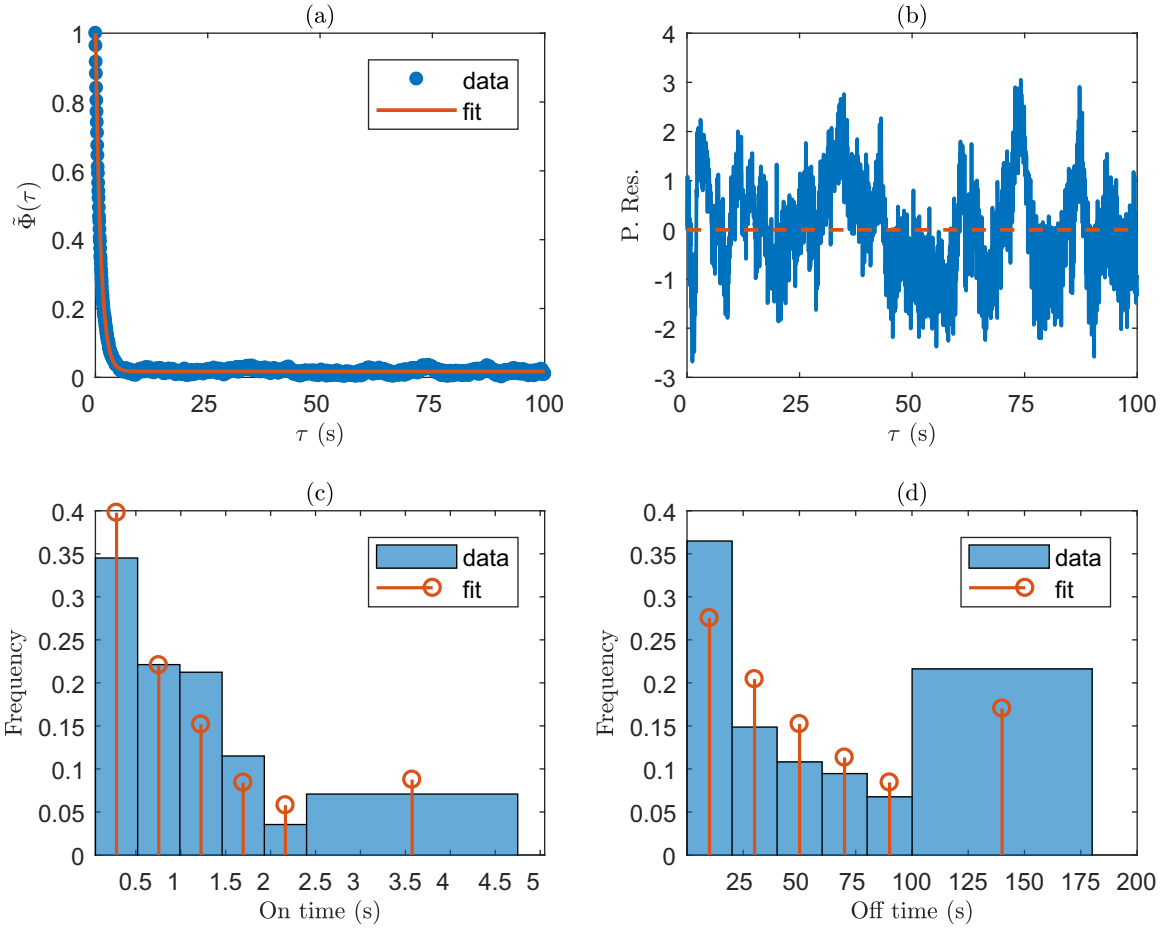

Autocorrelation		Single-molecule	
t_{on} (s)	t_{off} (s)	t_{on} (s)	t_{off} (s)
1.14 ± 0.01	69.3 ± 1.2	1.01 ± 0.18	67.8 ± 23.6

FIGURE 2.10: Comparison of autocorrelation and single-molecule analyses of STORM data under 4.5 mW laser light intensity ($\tau_i = 0.05$ s, $T = 3,600$ frames). (a) Autocorrelation and fit (photobleaching assumed to be negligible). (b) Pearson residuals from (a). (c) and (d) histogram of observed on- and off-times, respectively, overlaid with expected distributions. Assumed underlying distribution is geometric (truncated)* with best-fit parameter from MLE. p-values from χ^2 goodness-of-fit were computed to be $p \sim 0.2$ in both (c) and (d). Table compares fitted photoblinking times from both methods. The analysis in either case was done on a single ROI.

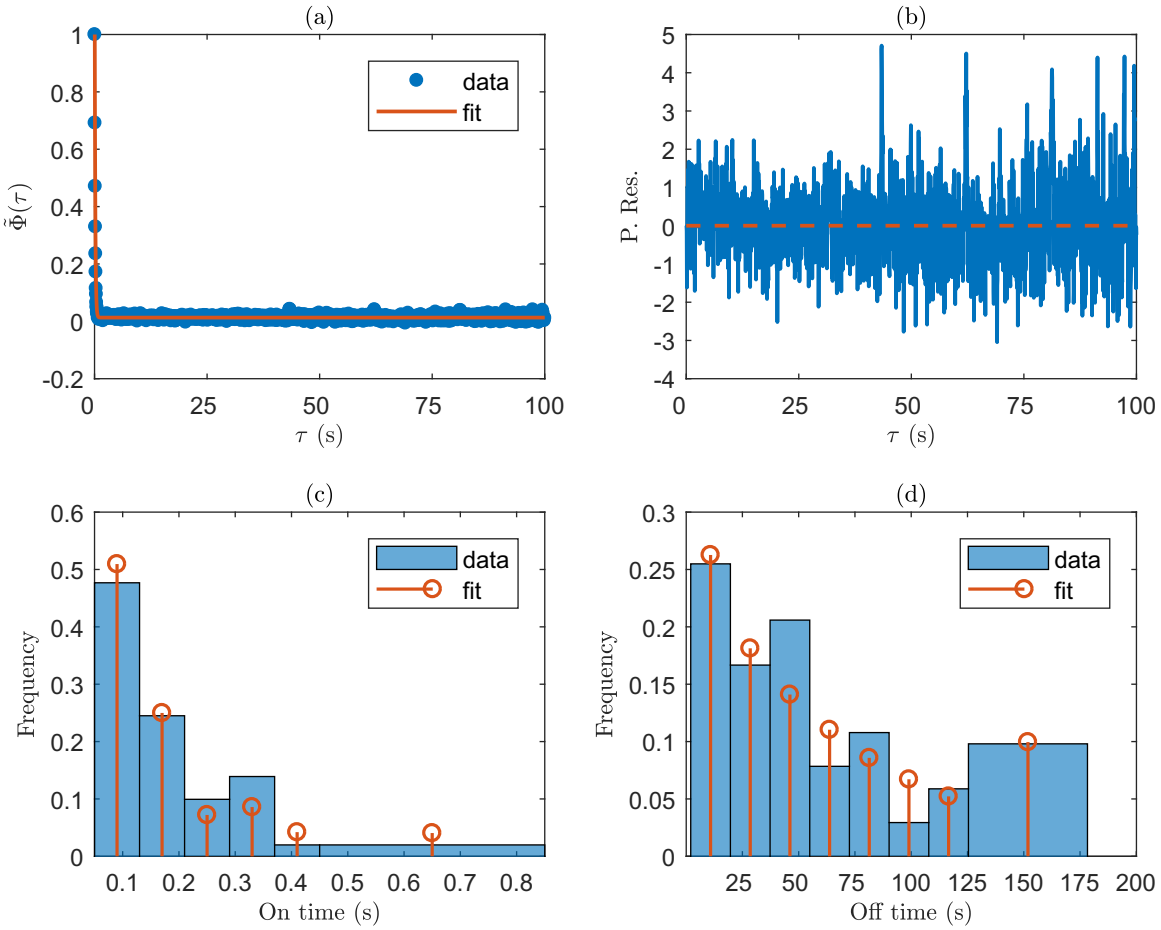

Autocorrelation		Single-molecule	
t_{on} (s)	t_{off} (s)	t_{on} (s)	t_{off} (s)
0.135 ± 0.002	14.7 ± 0.3	0.167 ± 0.022	71.0 ± 21.8

FIGURE 2.11: Comparison of autocorrelation and single-molecule analyses of STORM data under 20 mW laser light intensity ($\tau_i = 0.05$ s, $T = 3,600$ frames). (a) Autocorrelation and fit (photobleaching assumed to be negligible). (b) Pearson residuals from (a). (c) and (d) histogram of observed on- and off-times, respectively, overlaid with expected distributions. Assumed underlying distribution is geometric (truncated)* with best-fit parameter from MLE. p-values from χ^2 goodness-of-fit computed to be $p \sim 0.02$ and $p \sim 0.3$ in (c) and (d), respectively. Table compares fitted photoblinking times from both methods. The analysis in either case was done on a single ROI.

*Since the observed values for t_{off} are very close to the number of frames in the image series itself, we force the condition that there is 0 probability to exceed this value, while maintaining geometric weights for the other observations.

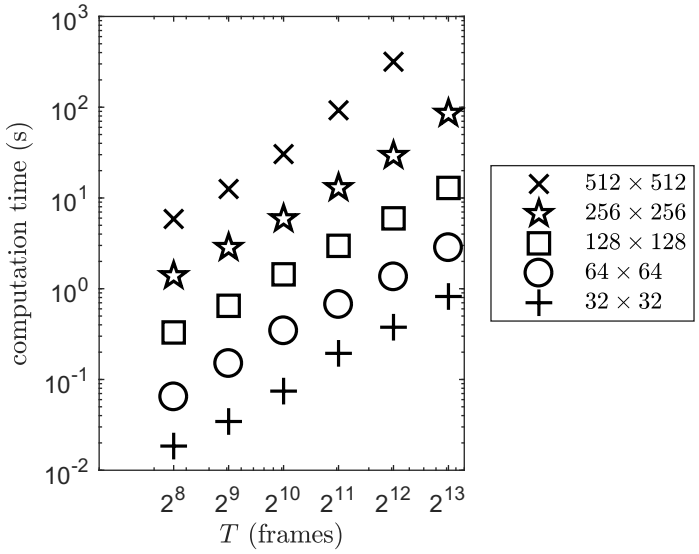

FIGURE 2.12: Computation times for calculating autocorrelations defined in Eq. (2.20) of different sized image series. Local spatial fluctuations were calculated using the default 10×10 pixel windows. Computation times were calculated on a research dedicated server (specifications detailed in methods section of main text).

Name	**Linker**	**DNA sequence**
Cy5-SeqA	phosphoramidite	5'-TTT TAT ATC TAT AGC GCG C-Cy5-3' 5'-ATT AGA TTA GCC CTT CCA GTG CGC GCT ATA GAT ATA AAA AGT GGC GTG GC-Biotin-3'
Cy5-RS1	succinimide	5'-Cy5-ACT CCA AGA CTT CGA CAC GAC T-3' 5'-Biotin-AGT CGT GTC GAA GTC TTG GAG T-3'
Cy5-D18	succinimide	5'-Cy5- ACC TCG CGA CCG TCG CCA -Biotin-3'

TABLE 2.6: Sequences of all oligonucleotides used in this study.

Sequence	Quencher	Buffer	Laser λ	Laser power*	Frame time	Emission filters
Cy5-RS1	Ni^{2+} (0.2 mM)	TRIS, pH 7.5	641 nm	6.5 mW	100 ms	HQ 685/70 and HQ 685/80
Cy5-SeqA	Ni^{2+} (1.0 mM)	PBS, pH 7.4		5.0 mW		
Cy5-D18	β-ME (143 mM)	TRIS, pH 8.0	647 nm	4.5 mW and 20 mW	50 ms	ET 705/72m

TABLE 2.7: Single-molecule imaging conditions used in this study.

*Measured out of the objective in widefield mode.

Imaging buffers

- PBS buffer pH 7.4 (137 mM NaCl, 2.7 mM KCl, 8 mM NaH_2PO_4, 2 mM K_2HPO_4)
- Tris buffer pH 7.5 (50 mM Tris-HCl, 40 mM NaCl)
- Tris buffer pH 8.0 (20 mM Tris-HCl, 50 mM NaCl)

Photostate autocorrelation

We first discuss the reason for neglecting the second term in Eq. (2.9). We assume here that the PSF is well-approximated by a Gaussian, but the argument should be easily extendable for any reasonable PSF functional shape; specifically, we have,

$$\frac{\langle I(\boldsymbol{u})\rangle^2}{\langle I^2(\boldsymbol{u})\rangle} = \frac{\omega_0^2}{A_{\mathrm{ROI}}} \ll 1 \implies \langle I(\boldsymbol{u})\rangle^2 \ll \langle I^2(\boldsymbol{u})\rangle,$$

where ω_0 is the e^{-2} radius of the Gaussian PSF and A_{ROI} is the area of the region of interest being analyzed, which we assume to be much greater than ω_0. Additionally, we expect the autocorrelation of the photostate to be positive on average, since each state has inherent memory in time,

$$\langle \Theta_{t_1}\Theta_{t_2}\rangle - \langle \Theta_{t_1}\rangle\langle \Theta_{t_2}\rangle \geq 0.$$

It follows that,

$$\langle I^2(\boldsymbol{u})\rangle\langle \Theta_{t_1}\Theta_{t_2}\rangle \gg \langle I(\boldsymbol{u})\rangle^2\langle \Theta_{t_1}\rangle\langle \Theta_{t_2}\rangle.$$

Omitting the second term in Eq. (2.9) yields Eq. (2.10).

In order to calculate Eq. (2.10) explicitly, we solve the system of differential equations in Eq. (2.21) representing the general photobleaching process depicted in Scheme 2.2.

$$\frac{\mathrm{d}}{\mathrm{d}t}\begin{pmatrix} N_{\mathrm{on}}(t) \\ N_{\mathrm{off}}(t) \\ N_{\varnothing}(t) \end{pmatrix} = \begin{pmatrix} -(k_{\mathrm{off}} + k_{\mathrm{p}_1}) & k_{\mathrm{on}} & 0 \\ k_{\mathrm{off}} & -(k_{\mathrm{on}} + k_{\mathrm{p}_2}) & 0 \\ k_{\mathrm{p}_1} & k_{\mathrm{p}_2} & 0 \end{pmatrix} \begin{pmatrix} N_{\mathrm{on}}(t) \\ N_{\mathrm{off}}(t) \\ N_{\varnothing}(t) \end{pmatrix}. \tag{2.21}$$

To get $\mathcal{P}(\sigma_2|\sigma_1)$, *i.e.* the conditional probability of the photostate at time t_2, σ_2, given the state at time t_1 ($\leq t_2$), σ_1, we solve the above system of differential equations with initial condition,

$$\begin{pmatrix} N_{\mathrm{on}} \\ N_{\mathrm{off}} \\ N_{\varnothing} \end{pmatrix}(t = t_1) = \delta_{\sigma_1,\sigma_2},$$

where $\delta_{\sigma_1,\sigma_2}$ is the Kronecker delta function. This can be easily accomplished by using standard eigenvalue/eigenvector methods.

To compute the autocorrelation while accounting for photobleaching, we specify that for $t < 0$, Θ_t is a pure photoblinking process, while for $t \geq 0$, it is the same blinking process with bleaching "turned on". We can then calculate the autocorrelation by using the law of total probability conditioned at $t = 0$,

$$\begin{aligned}\langle \Theta_2 \Theta_1 \rangle &= \sum_{\theta_0,\theta_1,\theta_2} \theta_1\theta_2 \mathcal{P}(\Theta_2 = \theta_2|\Theta_1 = \theta_1)\mathcal{P}(\Theta_1 = \theta_1|\Theta_0 = \theta_0)\mathcal{P}(\Theta_0 = \theta_0) \\ &= \mathcal{P}(\Theta_2 = 1|\Theta_1 = 1) \sum_{\theta_0} \mathcal{P}(\Theta_1 = 1|\Theta_0 = \theta_0)\mathcal{P}(\Theta_0 = \theta_0).\end{aligned}$$

In the above equation, Θ_0 is the observed photostate at $t = 0$, so that $\mathcal{P}(\Theta_0 = \theta_0)$ is the steady-state probability of the photoblinking process. Θ_1 and Θ_2 are the observed photostates at times t_1 and t_2 ($t_1 \leq t_2$), respectively.

We now explore three cases of the photostate autocorrelation relevant to this paper.

(i) Symmetric photobleaching. In this case, we consider $k_{\mathrm{p}_1} = k_{\mathrm{p}_2} = k_p$. The autocorrelation can then be expressed as,

$$\langle \Theta_2 \Theta_1 \rangle = \frac{k_{\mathrm{on}}}{K^2} e^{-k_p t_2}(k_{\mathrm{on}} + k_{\mathrm{off}} e^{-K(t_2 - t_1)}), \tag{2.22}$$

where we have defined $K = k_{\text{on}} + k_{\text{off}}$. When including the effect of time-integration of the detector, we get for $\tau \neq 0$

$$\int_{t+\tau}^{t+\tau+\tau_i}\int_{t}^{t+\tau_i}\langle\Theta_{t_2}\Theta_{t_1}\rangle \mathrm{d}t_1\mathrm{d}t_2 = \frac{k_{\text{on}}}{K^2}e^{-k_p(t+\tau)}\left(\frac{k_{\text{off}}\left(1-e^{-K}\right)\left(1-e^{-K_p}\right)}{KK_p}e^{-K(\tau-1)} + \frac{k_{\text{on}}\left(1-e^{-k_p}\right)}{k_p}\right)$$

where $K_p = K + k_p$. Note we set $\tau_i = 1$ (in units of frames here) for simplicity *i.e.* no dead time. Finally, we carry out the sum in Eq. (2.14),

$$\Phi(\tau) = \frac{A}{T-\tau}\frac{k_{\text{on}}}{k_pK^3K_p}\frac{\left(e^{-k_p\tau}-e^{-k_pT}\right)}{\left(1-e^{-k_p}\right)}\times \left\{k_{\text{off}}k_p\left(1-e^{-K}\right)\left(1-e^{-K_p}\right)e^{-K(\tau-1)} + k_{\text{on}}KK_p\left(1-e^{-k_p}\right)\right\}. \quad (2.23)$$

One can then normalize as in Eq. (2.15) to obtain an expression in terms of only photophysical/-chemical rates.

(ii) Off-state photobleaching. We now consider a model that only allows photobleaching from the off-state *i.e.* $k_{\text{p}_1} = 0$ and $k_{\text{p}_2} = k_p$.

In this case,

$$\langle\Theta_2\Theta_1\rangle = \frac{k_{\text{on}}}{4K\Delta^2}e^{-(K_p-\Delta)t_2/2}\Big\{\left((K_p-2k_{\text{off}}+\Delta)-(K_p-2k_{\text{off}}-\Delta)e^{-\Delta(t_2-t_1)}\right) \times\left((K_p+\Delta)-(K_p-\Delta)e^{-\Delta t_1}\right)\Big\},$$

where we have defined,

$$\Delta \equiv \sqrt{K_p^2-4k_pk_{\text{off}}}.$$

The time-integrated photostate autocorrelation is then (for $\tau \neq 0$),

$$\int_{t+\tau}^{t+\tau+\tau_i}\int_{t}^{t+\tau_i}\langle\Theta_{t_2}\Theta_{t_1}\rangle \mathrm{d}t_1\mathrm{d}t_2 = \frac{1}{2K\Delta^3}k_{\text{on}}(\Delta-2k_{\text{off}}+K_p)e^{-(K_p-\Delta)(t+\tau)/2} \times\left\{\frac{\Delta+2k_{\text{off}}-K_p}{\Delta-2k_{\text{off}}+K_p}\left(1-e^{-\Delta}+\frac{\Delta-K_p}{\Delta+K_p}\Delta e^{-\Delta(t+1)}\right)\left(1-e^{-(K_p+\Delta)/2}\right)e^{-\Delta(\tau-1)} - \left(\frac{\Delta+K_p}{\Delta-K_p}\Delta+\left(1-e^{-\Delta}\right)e^{-\Delta t}\right)\left(1-e^{-(K_p-\Delta)/2}\right)\right\},$$

where we again set $\tau_i = 1$. Finally, the sum in Eq. (2.14) gives

$$\begin{aligned}\Phi(\tau) = \frac{1}{2K\Delta^3} k_{\text{on}}(\Delta - 2k_{\text{off}} + K_p) e^{-(K_p-\Delta)\tau/2} \Bigg\{ & \frac{\Delta + 2k_{\text{off}} - K_p}{\Delta - 2k_{\text{off}} + K_p} \left(1 - e^{-(K_p+\Delta)/2}\right) e^{-\Delta(\tau-1)} \\ & \times \left((1 - e^{-\Delta}) \frac{1 - e^{-(K_p-\Delta)(T-\tau)/2)}}{1 - e^{-(K_p-\Delta)/2}} + \Delta e^{-\Delta} \frac{\Delta - K_p}{\Delta + K_p} \frac{1 - e^{-(K_p+\Delta)(T-\tau)/2}}{1 - e^{-(K_p+\Delta)/2}} \right) \\ & - \left(\left(1 - e^{-\Delta}\right) \frac{1 - e^{-(K_p+\Delta)(T-\tau)/2}}{1 - e^{-(K_p+\Delta)/2}} + \frac{\Delta + K_p}{\Delta - K_p} \Delta \frac{1 - e^{-(K_p-\Delta)(T-\tau)/2)}}{1 - e^{-(K_p-\Delta)/2}} \right) \\ & \times \left(1 - e^{-(K_p-\Delta)/2}\right) \Bigg\}. \end{aligned} \tag{2.24}$$

(iii) Asymmetric photobleaching. In the most general case of the two-state blinking system, both the on- and off-states have independent bleaching rates of k_{p_1} and k_{p_2}, respectively.

The photostate autocorrelation in this case is computed as

$$\begin{aligned}\langle \Theta_2 \Theta_1 \rangle = \frac{k_{\text{on}}}{4K\Delta^2} e^{-(K_p-\Delta)t_2/2} \Big\{ & \left((K_p - 2k_{\text{p}_1} + \Delta) - (K_p - 2k_{\text{p}_1} - \Delta) e^{-\Delta t_1} \right) \\ & \times \left((K_p - 2(k_{\text{p}_1} + k_{\text{off}}) + \Delta) - (K_p - 2(k_{\text{p}_1} + k_{\text{off}}) - \Delta) e^{-\Delta(t_2 - t_1)} \right) \Big\}, \end{aligned} \tag{2.25}$$

where we have redefined,

$$K_p \equiv K + k_{\text{p}_1} + k_{\text{p}_2}, \text{ and}$$

$$\Delta \equiv \sqrt{K_p^2 - 4(k_{\text{p}_1}(k_{\text{p}_2} + k_{\text{on}}) + k_{\text{p}_2} k_{\text{off}})}.$$

The time-integrated and time-averaged expressions are omitted from this text because of their size, but computation of these quantities is straightforward and we follow the same procedure as in the case above.

Temporal-mean subtraction

Defining the autocorrelation through the temporal intensity fluctuations, produces an autocorrelation expression that cannot be used to simultaneously fit both photoblinking rates in a simple two-state system. To demonstrate this, we consider the simple case of on-off photoswitching without bleaching. The general autocorrelation of the temporal

intensity fluctuations is written as

$$\begin{aligned}\Phi_{\delta t i}(\tau) &\equiv \langle \delta_t i_s(\boldsymbol{r}, t_1)\delta_t i_s(\boldsymbol{r}, t_2)\rangle \\ &= \langle i_s(\boldsymbol{r}, t_1) i_s(\boldsymbol{r}, t_2)\rangle - \langle \langle i_s(\boldsymbol{r}, t_1)\rangle_t \langle i_s(\boldsymbol{r}, t_2)\rangle_t\rangle, \end{aligned} \tag{2.26}$$

where the temporal mean is denoted as $\langle\cdot\rangle_t$. The first term was already calculated in Eq. (2.7). The second term can be calculated explicitly to give (making the same assumptions given in the main text)

$$\langle \langle i_s(\boldsymbol{r}, t_1)\rangle_t \langle i_s(\boldsymbol{r}, t_2)\rangle_t\rangle = q^2 \langle \Theta_{t_1}\rangle\langle \Theta_{t_2}\rangle\{N\langle I^2(\boldsymbol{u})\rangle + N(N-1)\langle I(\boldsymbol{u})\rangle^2\}.$$

Note that the temporal average does not affect $I(\boldsymbol{u})$ as the fluorophores are assumed to be immobile. Eq. (2.26) then yields

$$\phi_{\delta i}(t_1, t_2) = A\langle \delta\Theta_{t_1}\delta\Theta_{t_2}\rangle, \tag{2.27}$$

where,

$$A \equiv Nq^2\langle I^2(\boldsymbol{u})\rangle.$$

If we take Θ_t to be a simple two-state process (*i.e.* a fluorophore turning on and off), we have,

$$\begin{aligned}\langle \Theta_t\rangle &= \frac{k_{\text{on}}}{K} \text{ and} \\ \langle \Theta_t\Theta_{t+\tau}\rangle &= \frac{k_{\text{on}}}{K^2}(k_{\text{on}} + k_{\text{off}}e^{-K\tau}) \\ \implies \langle \delta\Theta_t\delta\Theta_{t+\tau}\rangle &= \frac{k_{\text{on}}k_{\text{off}}}{K^2}e^{-K\tau},\end{aligned}$$

where,

$$K \equiv k_{\text{on}} + k_{\text{off}}.$$

As one can see, Eq. (2.27) is unaffected by the interchange $k_{\text{on}} \leftrightarrow k_{\text{off}}$ so that both rates cannot be fit for simultaneously. Conversely, using spatial intensity fluctuations gives an expression that is not symmetric in the blinking rates, as was shown in this work.

Simulation details

This section gives full details about our simulations, initially discussed in methods section of main text. In order to explicitly compute the mean number of counts in Eq. (2.19) we

first compute the counts from the simulated emitters at pixel $\boldsymbol{x}$ and frame t as

$$n_s(\boldsymbol{x}, f) = \int_f \int_{\boldsymbol{x}} I(\boldsymbol{r}) \circledast_{\boldsymbol{r}} \rho(\boldsymbol{r}, t)\, \mathrm{d}\boldsymbol{r}\, \mathrm{d}t.$$

The first integral is over the entirety of pixel $\boldsymbol{x}$, while the second integral is over the exposure time of frame f. We choose the form of the PSF to be a Gaussian with e^{-2} radius ω_0. The laser illumination profile is also chosen to be Gaussian with peak set to unity at the center of each simulated image and e^{-2} radius Ω_0. Each simulated fluorophore emits n_{avg} photon counts per frame per molecule on average, given that the molecule occupies the on-state for a full frame.

Tabulated below are default parameters used in our simulations.

Parameter description	Value
Analogue to digital conversion factor	12
Autofluorescent photon rate (n_{afl})	$1 - 5\%$ of n_{avg} pixel^{-1}
Clock induced charge (n_{cic})	5×10^{-3} frame^{-1} pixel^{-1}
Dark noise photon rate (n_{dn})	8×10^{-4} frame^{-1} pixel^{-1}
Detector quantum efficiency (Q_d)	0.9
EM Gain	200
Exposure time (τ_i)	0.1 s frame^{-1}
Image dimensions	64×64 pixels^2
Laser e^{-2} radius (Ω_0)	128 pixels
Average photon rate per molecule (n_{avg})	500 frame^{-1}
PSF e^{-2} radius (ω_0)	1.7 pixels

TABLE 2.8: Default simulation parameters.
These parameters were used to generate simulations presented throughout this work, unless otherwise stated. Some simulated noise values are negligible, but are included for completeness.

Photobleaching model comparison

As mentioned in the main text, the autocorrelation of a blinking system of particles photobleaching from the off-state is comparable to that of equal photobleaching rates from both on- and off-states in certain limits. We show two examples comparing the two models in Figure 2.13. As can be observed from this figure, the two models diverge from one another as both blinking rates become comparable to the photobleaching rate *i.e.* as K approaches k_p. Conversely, in the limit where at least one of the blinking rates is much faster than the bleaching rate, the autocorrelations from both models recover the correct

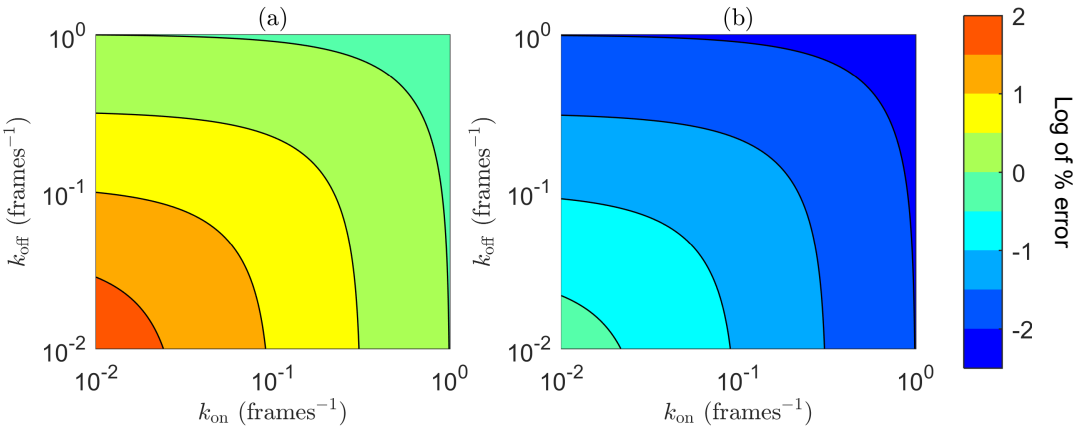

FIGURE 2.13: Contour plots comparing the autocorrelation of the symmetric-bleach model to that of the off-bleach model as a function of the photoblinking rates. Each plot compares the log of the percent error between the fixed k_{on} and the fitted k_{on}; the same plots for k_{off} yield almost identical results, and so are omitted from this work. In order to generate these plots, we first evaluate the off-bleach model with a fixed set of parameters, and subsequently fit the symmetric-bleach model in order to assess how well the chosen blinking rates can be recovered from the fit. In Figure (a) $k_p = 10^{-2}$ frames^{-1} and in (b) $k_p = 10^{-4}$ frames^{-1}. Note that k_p is not expected to agree between both models, and so is not compared here.

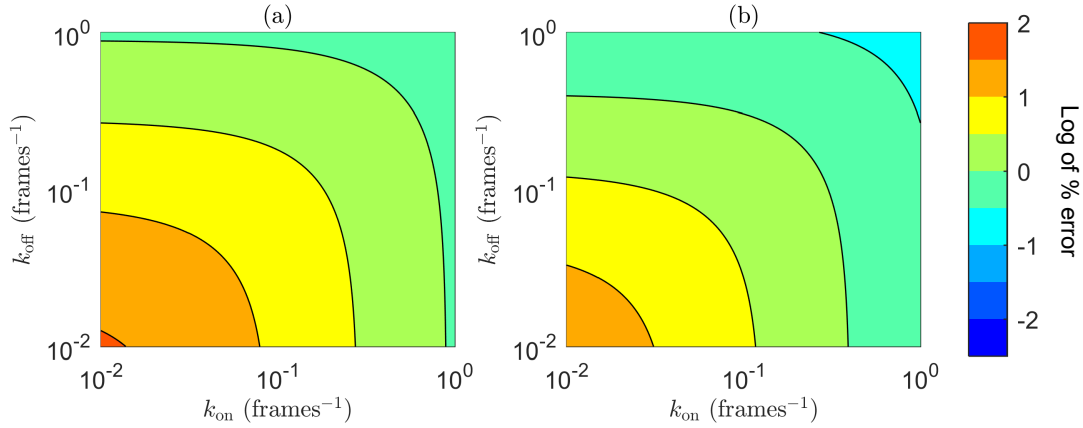

FIGURE 2.14: Contour plots comparing the autocorrelation of the symmetric- and asymmetric-bleach models as a function of the photoblinking rates. Each plot compares the log of the percent error between the fixed k_{on} and the fitted k_{on}; the same plots for k_{off} yield more accurate results when k_{p_2} is lower. The same relation was found between k_{on} and k_{p_1}. In order to generate these plots, we first evaluate the asymmetric-bleach model with a fixed set of parameters, and subsequently fit the symmetric-bleach model in order to assess how well the chosen blinking rates can be recovered from the fit. In Figure (a) $k_{\text{p}_1} = 10^{-2}, k_{\text{p}_2} = 10^{-3}$ frames^{-1} and in (b) $k_{\text{p}_1} = 10^{-3}$, $k_{\text{p}_2} = 5 \times 10^{-3}$ frames^{-1}.

blinking rates *i.e.* $K \gg k_p$. The same behavior was observed when comparing the model with equal bleaching rates from both on/off states to the general case when the two rates are not equal, $k_{\mathrm{p}_1} \neq k_{\mathrm{p}_2}$, as can be seen in Figure 2.14. In this case, the two models agree on the fitted blinking rates when $K \gg k_{\mathrm{p}_1} + k_{\mathrm{p}_2}$.

Expected total number of blink cycles

We derive the expected total number of blink cycles in T frames for N fluorophores undergoing photobleaching exclusively from the off-state.

The expected length of a blink cycle is,

$$T_c = \frac{1}{k_{\mathrm{on}}} + \frac{1}{k_{\mathrm{off}}}.$$

Assuming there are $N_{\mathrm{eff}}(t)$ unbleached fluorophores in the infinitesimal time window $[t, t+\mathrm{d}t)$, this means the infinitesimal number of cycles that occur on average in this window is

$$\mathrm{d}\nu_c = N_{\mathrm{eff}}(t)\,\mathrm{d}t/T_c \implies \nu_c = \int_0^{T-1} N_{\mathrm{eff}}(t)\,\mathrm{d}t/T_c. \tag{2.28}$$

In order to proceed, we need to first determine $N_{\mathrm{eff}}(t)$. As the bleaching only occurs from the off-state, we have,

$$N'_{\mathrm{eff}}(t) = -k_p N_{\mathrm{off}}(t). \tag{2.29}$$

As was shown in Eq. (2.21), $N_{\mathrm{off}}(t)$ can be computed from solving the following coupled differential equations,

$$\frac{\mathrm{d}}{\mathrm{d}t}\begin{pmatrix} N_{\mathrm{on}}(t) \\ N_{\mathrm{off}}(t) \end{pmatrix} = \begin{pmatrix} -k_{\mathrm{off}} & k_{\mathrm{on}} \\ k_{\mathrm{off}} & -(k_{\mathrm{on}} + k_{\mathrm{p}}) \end{pmatrix} \begin{pmatrix} N_{\mathrm{on}}(t) \\ N_{\mathrm{off}}(t) \end{pmatrix}.$$

with initial conditions,

$$N_{\mathrm{on}}(t=0) = Nk_{\mathrm{on}}/K,\ N_{\mathrm{off}}(t=0) = Nk_{\mathrm{off}}/K.$$

The solution to Eq. (2.29) is given by,

$$N_{\mathrm{eff}}(t) = \frac{N}{4K\Delta} e^{-(K_p-\Delta)t/2} \times \left\{(\Delta + K_p)(\Delta + K - k_p) - (\Delta - K_p)(\Delta + k_p - K)e^{-\Delta t}\right\}.$$

In order to determine the number of frames needed for a fixed number of expected events, we numerically solve Eq. (2.28) for T. To choose the number of frames for the simulations in Figure 2.5, we additionally impose the condition that $\min T_c = 2$ frames (independent of the rates simulated).

Analysis of STORM data

Application of STORM analysis requires the condition $k_{\text{on}} \ll k_{\text{off}}$ in order to yield isolated emitters. Here we discuss the applicability of our method in this limit.

For demonstration purposes, we make the simplifying assumptions of negligible photobleaching and detector-resolvable on-times. The autocorrelation of the image intensity fluctuations is then given by Eq. (2.22). We simplify this equation further using the fact that $k_{\text{on}} \ll k_{\text{off}}$, so that we now have

$$\Phi(\tau) \simeq A \frac{k_{\text{on}}}{k_{\text{off}}} \left(\frac{k_{\text{on}}}{k_{\text{off}}} + e^{-k_{\text{off}}\tau} \right).$$

From this expression we see that k_{off} is responsible for the exponential decay, while information about k_{on} can be found in the constant offset term. Moreover, we have that the ratio $k_{\text{on}}/k_{\text{off}}$ tends to 0, so that the constant term becomes small enough to be comparable to the noise, making it more difficult to recover k_{on} from a fit as this ratio decreases.

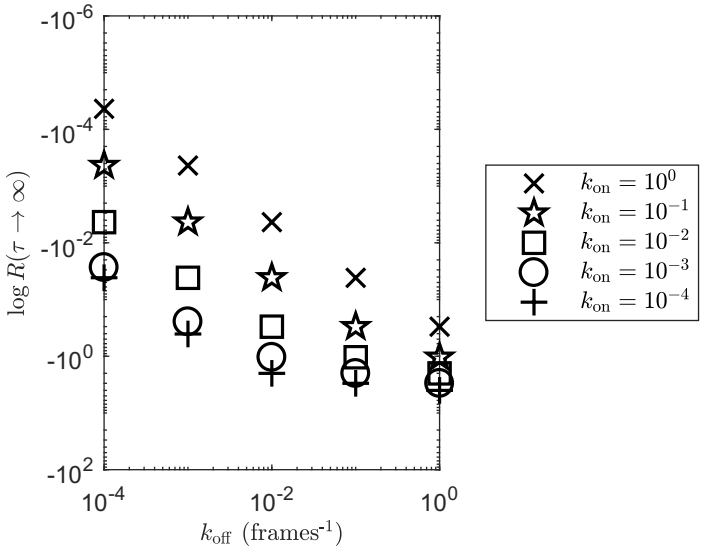

FIGURE 2.15: Logarithm of offset values from Eq. (2.22) for different instances of $(k_{\text{on}}, k_{\text{off}})$ when $k_p = 0$.

From Figure 2.15 one can also see that increasing the value of k_{on} by an order of magnitude has little effect on the offset as the ratio k_{on}/k_{off} decreases. This is problematic since this means small systematic errors in the ACF computed from data can result in significantly biased fits for k_{on}, which is why it is important to correct for background illumination when $k_{on} \ll k_{off}$, for example. It is also crucial to get as much information as possible for k_{on} from the ACF by fitting a wide time-lag range. In Figure 2.16, we demonstrate the performance of our method through simulations generated with different values of this ratio. As expected, the fits for k_{on} worsen as k_{on}/k_{off} decreases. We also show in Figure 2.8 that the fit for a simulation generated with low k_{on}/k_{off} converges to the correct k_{on} value given enough sampling.

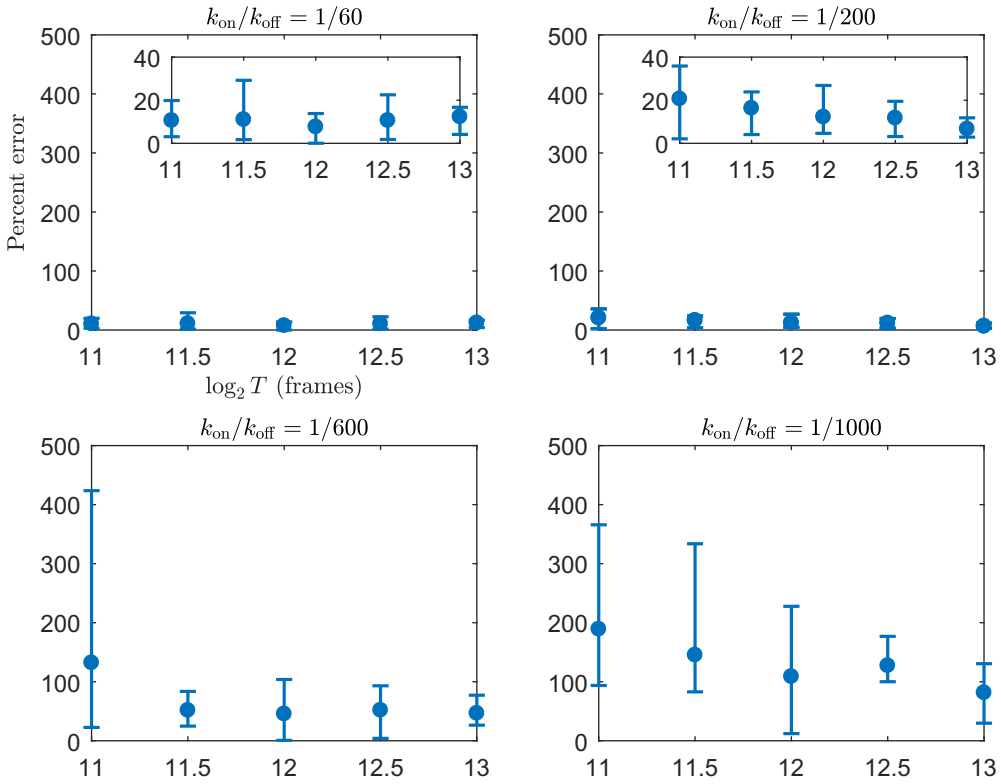

FIGURE 2.16: Percent error on ACF fits for k_{on} for different instances of k_{on}/k_{off} from simulation as a function of number of frames analyzed. Each point represents the average fitted k_{on} value from 5 independent simulations, while error bars represent the minimum and maximum percent errors over the 5 simulations. Analysis was done on a 45×45 pixel ROI in the center of each simulated image series. Simulated image series were background corrected before analysis (see STORM data section in main text for more details). All fits are done over the first 2,000 time-lags (excluding $\tau = 0$). Insets show magnified portions of plots. Simulation parameters: $N = 200$; $t_{off} = 60$ s; laser e^{-2} beam radius, $\Omega_0 = 64$ pixels; $k_p = 2 \times 10^{-3}$ s. t_{on} is chosen according to the given k_{on}/k_{off} for each plot.

Non-uniform densities

Here we analyze a simulated movie that is non-uniform in density and show that the most effective approach, in this case, is to compute the ACF from an ROI where the label density can be considered approximately uniform. We simulate a "star" pattern using the TestSTORM[7] package suite with set default parameters, except for the blinking rates. This pattern consists of 16 arms, with each arm having 200 simulated fluorescent labels randomly placed along it, by default.

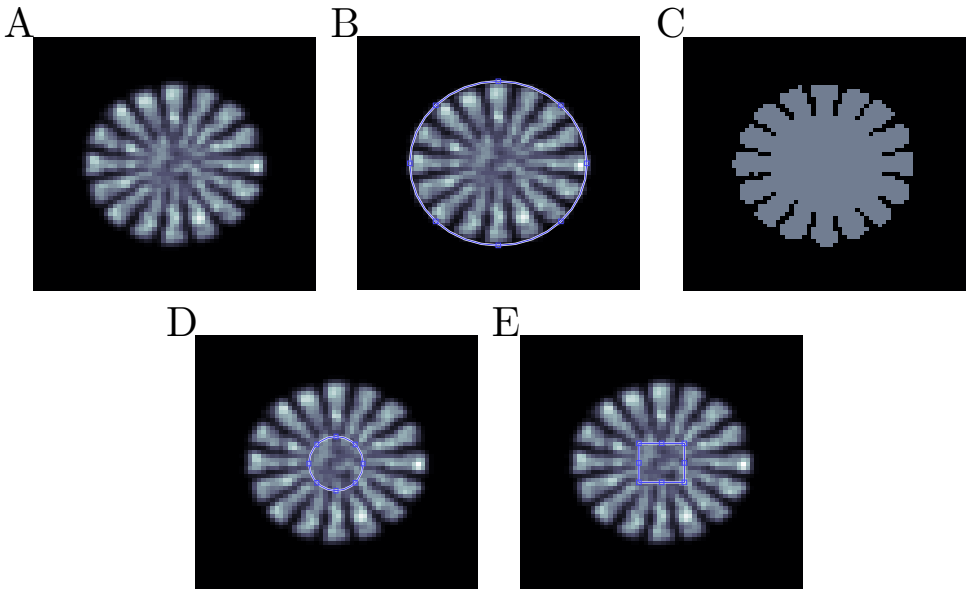

	Fitted		Simulated		
Figure	t_{on} (s)	t_{off} (s)	t_{on} (s)	t_{off} (s)	t_p (s)
(A)	0.0518 ± 0.0003	0.843 ± 0.005	0.05	5	1700
(B)	0.0516 ± 0.0003	0.852 ± 0.005			
(C)	0.0502 ± 0.0003	1.36 ± 0.01			
(D)	0.051 ± 0.001	5.1 ± 0.2			
(E)	0.052 ± 0.001	5.0 ± 0.2			

FIGURE 2.17: Different ROIs used to analyze simulated movie. Fits to the corresponding ACFs are shown in the table. All fits are done over the first 200 time-lags (excluding $\tau = 0$) and without bleaching incorporated into the fit function as the autocorrelations do not show a bleaching decay due to the relatively slow bleaching rate simulated. Camera exposure time simulated as $\tau_i = 0.05$ s for $T = 3,000$ frames. (A) temporal mean of the simulated image counts, in this case the whole movie was analyzed without choosing an ROI; (C) the ROI is chosen so that the autocorrelation is computed only in the gray region; (B), (D), (E) ROIs superimposed on the temporal mean of simulated counts.

The non-uniformity of this pattern can be seen in the temporal mean in Figure 2.17 (A). The fits are only accurate for the ROIs shown in Figures 2.17 (D) and (E). In Figure 2.18 we compare the autocorrelations computed from Figures 2.17 (A) and (E). One can see that the decay due to photoblinking is the same. This matches with the accurate recovery of the sum of the rates in each case in Figure 2.17, which is approximately equal to k_{off} since $k_{\text{on}} \ll k_{\text{off}}$ (recall $t_{\text{on}} = 1/k_{\text{off}}$). Conversely, the ACF offsets do not match.

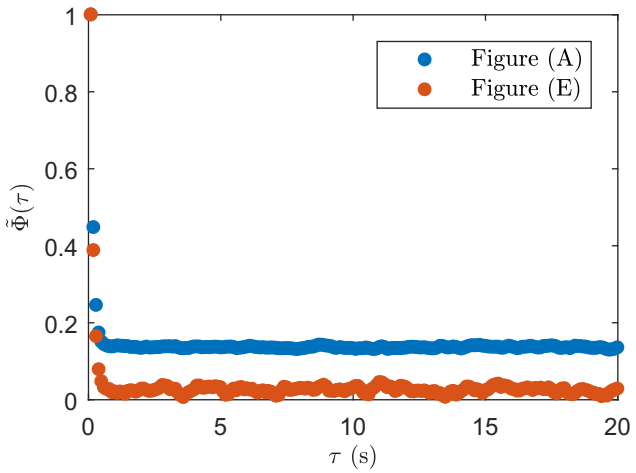

FIGURE 2.18: Comparison between ACFs computed from ROIs shown in Figures 2.17 (A) and (E).

Local spatial mean subtraction

As argued in the previous section, non-uniformity in an image series can yield inaccurate fits for photophysical/-chemical parameters. As a way to mitigate these effects, we choose to define intensity fluctuations through subtraction of local spatial means (see Eq. (2.20)). Using an example we demonstrate that this yields better results than simply subtracting the global spatial mean from each image. In Figure 2.19 we compare the autocorrelation computed from both local and global spatial mean subtractions of a simulation with a non-uniform laser illumination profile (using our default simulated laser e^{-2} beam radius of $\Omega_0 = 128$ pixels).

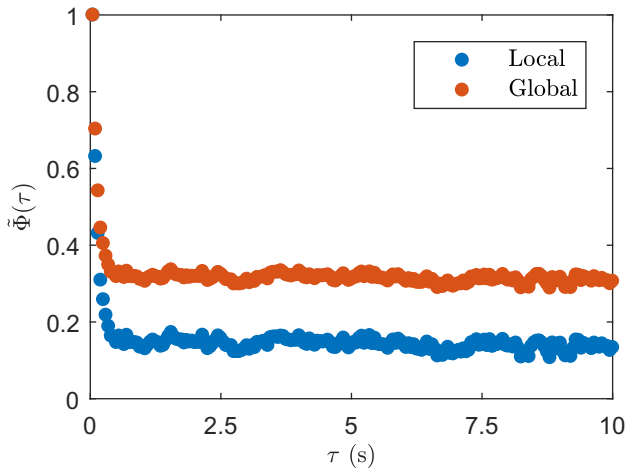

FIGURE 2.19: Comparison of ACFs calculated with local and global spatial mean subtraction. Simulation parameters: $T = 2,048$ frames, $N = 50$, $\tau_i = 0.05$ s, $k_p = 2 \times 10^{-2}$ s^{-1}.

	Fitted		Simulated	
	t_{on} (s)	t_{off} (s)	t_{on} (s)	t_{off} (s)
Local	0.101 ± 0.005	0.946 ± 0.038	0.1	1
Global	0.115 ± 0.006	0.411 ± 0.012		

TABLE 2.9: Fitted and simulated values for the ACFs shown in Figure 2.19.

ROI selection

Ideally, an ROI should be chosen so that it is big enough to sample sufficient blinking fluorophores; however, non-uniformity present in an image series also needs to be considered. For example, photobleaching rates are well known to be dependent on excitation laser intensity, which could cause spatial dependence on the bleaching rates. We also discussed the effects of analyzing non-uniform fluorophore densities using our method. Therefore, it is important to consider these effects and to select ROIs that are also small enough so that non-uniformity is not present.

References for Chapter 2

[1] M. J. Rust, M. Bates, and X. Zhuang. Sub-diffraction-limit imaging by stochastic optical reconstruction microscopy (STORM). *Nat. Methods* **3**,10 (2006), pp. 793–796.

[2] T. Dertinger et al. Fast, background-free, 3D super-resolution optical fluctuation imaging (SOFI). *Proc. Natl. Acad. Sci. U.S.A.* **106**,52 (2009), pp. 22287–22292.

[3] A. Sharonov and R. M. Hochstrasser. Wide-field subdiffraction imaging by accumulated binding of diffusing probes. *Proc. Natl. Acad. Sci. U.S.A.* **103**,50 (2006), pp. 18911–18916.

[4] G. T. Dempsey et al. Evaluation of fluorophores for optimal performance in localization-based super-resolution imaging. *Nat. Methods* **8**,12 (2011), p. 1027.

[5] S. Doose et al. Comparison of Photophysical and Colloidal Properties of Biocompatible Semiconductor Nanocrystals Using Fluorescence Correlation Spectroscopy. *Anal. Chem.* **77**,7 (2005), pp. 2235–2242.

[6] S. Boyle et al. Quantum Dot Fluorescence Characterizes the Nanoscale Organization of T Cell Receptors for Antigen. *Biophys. J.* **101**,11 (2011), pp. L57–L59.

[7] T. Novák et al. TestSTORM: Versatile simulator software for multimodal super-resolution localization fluorescence microscopy. *Sci. Rep.* **7**,1 (2017), pp. 1–8.

[8] D. L. Kolin and P. W. Wiseman. Advances in image correlation spectroscopy: measuring number densities, aggregation states, and dynamics of fluorescently labeled macromolecules in cells. *Cell Biochem. Biophys.* **49**,3 (2007), pp. 141–164.

[9] C. Chatfield. *The analysis of time series: an introduction*. 6th. Florida, US: CRC Press, 2004.

[10] S. Saffarian and E. L. Elson. Statistical analysis of fluorescence correlation spectroscopy: the standard deviation and bias. *Biophys. J.* **84**,3 (2003), pp. 2030–2042.

[11] R. Luchowski et al. Single molecule studies of multiple-fluorophore labeled antibodies. Effect of homo-FRET on the number of photons available before photobleaching. *Curr. Pharm. Biotechnol.* **9**,5 (2008), pp. 411–420.

[12] E. M. Conroy et al. Self-Quenching, Dimerization, and Homo-FRET in Hetero-FRET Assemblies with Quantum Dot Donors and Multiple Dye Acceptors. *J. Phys. Chem. C* **120**,31 (2016), pp. 17817–17828.

[13] V. Glembockyte, R. Lincoln, and G. Cosa. Cy3 Photoprotection Mediated by Ni2+ for Extended Single-Molecule Imaging: Old Tricks for New Techniques. *J. Am. Chem. Soc.* **137**,3 (2015), pp. 1116–1122.

[14] V. Glembockyte, J. Lin, and G. Cosa. Improving the Photostability of Red- and Green-Emissive Single-Molecule Fluorophores via Ni2+ Mediated Excited Triplet-State Quenching. *J. Phys. Chem. B* **120**,46 (2016), pp. 11923–11929.

[15] E. K. L. Yeow et al. Characterizing the Fluorescence Intermittency and Photobleaching Kinetics of Dye Molecules Immobilized on a Glass Surface. *J. Phys. Chem. A* **110**,5 (2006), pp. 1726–1734.

[16] W.-T. Yip et al. Classifying the Photophysical Dynamics of Single- and Multiple-Chromophoric Molecules by Single Molecule Spectroscopy. *J. Phys. Chem. A* **102**,39 (1998), pp. 7564–7575.

[17] J. Widengren, U. Mets, and R. Rigler. Fluorescence correlation spectroscopy of triplet states in solution: a theoretical and experimental study. *J. Phys. Chem.* **99**,36 (1995), pp. 13368–13379.

[18] I. Khaw et al. Flat-field illumination for quantitative fluorescence imaging. *Opt. Express* **26**,12 (June 2018), pp. 15276–15288.

[19] H. D. Kim et al. Mg2+-dependent conformational change of RNA studied by fluorescence correlation and FRET on immobilized single molecules. *Proc. Natl. Acad. Sci. U.S.A.* **99**,7 (2002), pp. 4284–4289.

[20] G. Cosa et al. Secondary Structure and Secondary Structure Dynamics of DNA Hairpins Complexed with HIV-1 NC Protein. *Biophys. J.* **87**,4 (2004), pp. 2759–2767.

[21] J. Mücksch et al. Quantifying Reversible Surface Binding via Surface-Integrated Fluorescence Correlation Spectroscopy. *Nano Lett.* **18**,5 (2018), pp. 3185–3192.

[22] S. Geissbuehler et al. Mapping molecular statistics with balanced super-resolution optical fluctuation imaging (bSOFI). *Opt. Nanoscopy* **1**,1 (2012), pp. 1–7.

[23] W. Wang et al. Super Temporal-Resolved Microscopy (STReM). *J. Phys. Chem. Lett.* **7**,22 (2016), pp. 4524–4529.

[24] R. M. Dickson et al. On/off blinking and switching behaviour of single molecules of green fluorescent protein. *Nature* **388**,6640 (1997), p. 355.

[25] M. Haase et al. Exponential and Power-Law Kinetics in Single-Molecule Fluorescence Intermittency. *J. Phys. Chem. B* **108**,29 (2004), pp. 10445–10450.

[26] J. Houel et al. Autocorrelation Analysis for the Unbiased Determination of Power-Law Exponents in Single-Quantum-Dot Blinking. *ACS Nano* **9**,1 (2015), pp. 886–893.

[27] Y. Gidi et al. Efficient One-Step PEG-Silane Passivation of Glass Surfaces for Single-Molecule Fluorescence Studies. *ACS Appl. Mater. Interfaces* **10**,46 (2018), pp. 39505–39511.

[28] D. T. Gillespie. Exact stochastic simulation of coupled chemical reactions. *J. Phys. Chem.* **81**,25 (1977), pp. 2340–2361.

[29] M. Hirsch et al. A Stochastic Model for Electron Multiplication Charge-Coupled Devices – From Theory to Practice. *PLOS ONE* **8**,1 (Jan. 2013), pp. 1–13.

[30] S. A. McKinney, C. Joo, and T. Ha. Analysis of Single-Molecule FRET Trajectories Using Hidden Markov Modeling. *Biophys. J.* **91**,5 (2006), pp. 1941–1951.

Preface to Chapter 3

In this chapter we will introduce another novel fluorescence image correlation technique optimized for rapid simultaneous measurements of diffusion coefficients, photoblinking rate constants and fraction of diffusing particles. As was previously discussed, FCS only considers temporal fluorescence fluctuations in a single focal volume in the computation of its ACF, while ICS techniques utilize both spatial and temporal information to increase the statistical sampling. Therefore, most ICS methods require ergodicity in both time and space to be properly applied for analysis of a given ROI and time of interest (TOI) sample from a microscopy image series of the system of interest. This requirement is especially challenging to meet in the complex environment of live cells. A spatially inhomogeneous distribution of fluorophores within an ROI is one example that can violate such a condition. If this inhomogeneous population of particles can be assumed to be immobile or slowly moving, one can apply a Fourier filter[72] or subtract a moving average[75, 81] from the fluorescence image series to remove these components. If the fluorophores are also blinking and bleaching, however, these solutions are not generally applicable without additional consideration of these effects. Here we developed an extended kICS technique that is capable of analyzing ROIs with spatially inhomogeneous distributions of fluorophores that are subject to photophysical processes. This allows for analysis of fluorescence image series that were previously inaccessible to image correlation methods, including the analysis of systems relevant to SOFI and STORM. This further allows one to increase spatial sampling by analyzing larger ROIs. We demonstrated the range of applicability and applied our method on computer simulated images with simulated EMCCD noise and Dronpa-C12 labeled beta-actin in live NIH/3T3 and HeLa cells. The diffusion rates measured using our method for globular actin (G-actin) in the cytoplasm were consistent with previously reported values in the literature. Furthermore, we showed that the photoblinking rates followed the expected trend with varying excitation intensity in the live HeLa cell experiments.

Previously mentioned comparisons with single-molecule approaches apply to our extended kICS method, except that with this technique one can analyze ROIs with spatially inhomogeneous distributions of immobile blinking and bleaching particles. Note that our

technique also requires sufficient spatial and temporal sampling to yield accurate measurements. On the other hand, it can be challenging to employ SPT methods on systems with both blinking and diffusion processes. We hope our developed method will be used together with STORM or SOFI to also characterize dynamics pertinent to optimization of the single-molecule localization measurements.

Chapter 3

Rapid Ensemble Measurement of Protein Diffusion and Probe Blinking Dynamics in Cells

This section is based on the published manuscript:
Sehayek, S., Yi, X., Weiss, S., and Wiseman, P.W. Rapid Ensemble Measurement of Protein Diffusion and Probe Blinking Dynamics in Cells, *Biophys. Rep.*, **1**, 2, 100015 (2021).[3]

3.1 Abstract

We present a fluorescence fluctuation image correlation analysis method that can rapidly and simultaneously measure the diffusion coefficient, photoblinking rates, and fraction of diffusing particles of fluorescent molecules in cells. Unlike other image correlation techniques, we demonstrated that our method could be applied irrespective of a non-uniformly distributed, immobile blinking fluorophore population. This allows us to measure blinking and transport dynamics in complex cell morphologies, a benefit for a range of super-resolution fluorescence imaging approaches that rely on probe emission blinking. Furthermore, we showed that our technique could be applied without directly accounting for photobleaching. We successfully employed our technique on several simulations with realistic EMCCD noise and photobleaching models, as well as on Dronpa-C12 labeled beta-actin in living NIH/3T3 and HeLa cells. We found that the diffusion coefficients measured using our method were consistent with previous literature values. We further found that photoblinking rates measured in the live HeLa cells varied as expected with changing excitation power.

Why it matters

We developed an image correlation fluorescence fluctuation analysis technique that can analyze microscopy images of cells containing non-homogeneous distributions of immobile biomolecules labeled with fluorophores that are subject to photoblinking and photobleaching. As far as we know, this is the first image correlation method that does this. This enables the study of intricate cellular systems using fluorescent probes with complex photophysical properties. Our method rapidly and simultaneously measures diffusion and photoblinking rates, as well as the fraction of diffusing particles. We tested our technique on simulations and Dronpa-C12 labeled beta-actin in live NIH/3T3 and HeLa cells. Our measured diffusion coefficients from the live cell experiments were consistent with previously reported values in the literature.

3.2 Introduction

The past decade has seen a revolution in optical microscopy with the advent of far-field super-resolution approaches. Fluorescence super-resolution microscopy has become an invaluable tool for furthering our understanding of biological systems by allowing one to circumvent the diffraction limited resolution of traditional fluorescence microscopy techniques, leading to important insights in cell biology, neuroscience and cellular biophysics.[1–5] Among the super-resolution imaging techniques, single-molecule localization microscopy (SMLM) methods are one of the most commonly used. These methods rely on photophysical processes to localize the position of single fluorophores with a spatial uncertainty much lower than the wavelength diffraction limit of light. Some popular examples of such techniques are stochastic optical reconstruction microscopy (STORM)[6] and photoactivated localization microscopy (PALM).[7] Super-resolution optical fluctuation imaging (SOFI)[8] also relies on the stochastic photoswitching nature of fluorophores, but builds super-resolution images using the cumulants of the fluorescence fluctuations. Many applications of super-resolution, however, have so far been limited to studying immobile components in cells, or static molecules in chemically fixed cells, without examining their dynamic counterparts. While super-resolution has also been coupled with quantitative methods to investigate these dynamics, there are currently only a limited number of approaches that combine super-resolution imaging and measurement of dynamics. Notably, stimulated emission depletion (STED) microscopy was combined with fluorescence correlation spectroscopy (FCS) in STED-FCS,[9] which was shown to better characterize heterogeneous diffusive behavior of membrane biomolecules than traditional FCS by

reducing the beam spot size. Scanning versions of this technique exist, as well.[10, 11] Single-particle tracking (SPT) and PALM were also combined in sptPALM.[12] Minimal photon fluxes (MINFLUX)[13] is also capable of super-resolved SPT. Another example is fcsSOFI, which combines FCS and SOFI techniques to form super-resolved diffusion maps.[14]

Many methods currently exist for measuring the dynamics in biological systems and a significant subset rely on measurement of fluorescence fluctuations to compute autocorrelations that are then fit with specific models to measure transport parameters, such as biomolecule diffusion coefficients and directed flow rates. Conventional FCS[15–17] is a widely used example that analyzes fluorescence fluctuation time series collected from a single fixed laser focal spot. Imaging FCS[18] was developed to allow for multiplexed FCS analysis of pixels forming a fluorescence image. Similarly, image correlation spectroscopy (ICS) methods[19–22] also analyze fluorescence fluctuations in images, but utilize both spatial and temporal information when computing the autocorrelation. One advantage of ICS techniques is that the use of spatial information increases statistical sampling; however, the inherent spatiotemporal heterogeneity in biological systems makes it difficult to simply average over different pixels and frames. ICS techniques usually handle spatiotemporal heterogeneity by analyzing many smaller local regions of interest (ROIs), and then correlating over a chosen time of interest (TOI). This is the approach for generating flow maps when using spatiotemporal image correlation spectroscopy (STICS).[21] The most challenging example of heterogeneity in time in fluorescence microscopy is the issue of photobleaching, which has been addressed using both pre-[23–25] and post-processing[26–30] methods. Another example is anomalous diffusion, which has been investigated in multiple FCS studies.[31–36]

As super-resolution aims to better resolve complex cell processes in space and time, a technique that can analyze dynamics in the presence of spatially and temporally heterogeneous structures is required. Here we present an image correlation method that can successfully and rapidly analyze heterogeneous systems for accurate measurement of biomolecule diffusion coefficients, probe photoblinking rates and fraction of particles undergoing diffusion (see Figure 3.1). Along with measuring dynamic parameters in a complex cell environment, we anticipate that the measurement of probe photoblinking rates will be useful for optimal fluorescent probe development and optimization for methods like STORM and SOFI. The ability of our method to analyze spatially heterogeneous systems further allows us to significantly increase the spatial sampling used in our autocorrelation computation.

Our method is based on k-space image correlation spectroscopy (kICS),[19] which

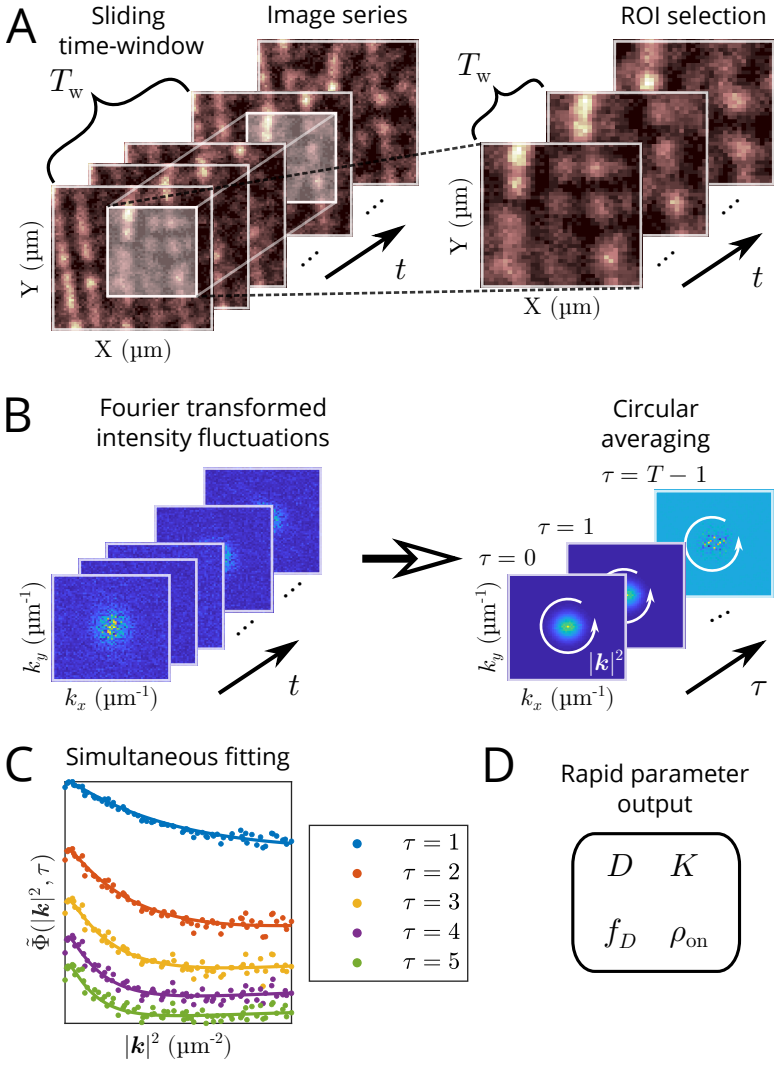

FIGURE 3.1: Schematic illustrating extended kICS method application. (A) An ROI and sliding time-window are first chosen from an image series. Intensity fluctuations are computed locally in time, according to the chosen time-window size, to mitigate the effects of photobleaching. (B) The 2D spatial Fourier transforms of the intensity fluctuations are first computed in each frame, then this k-space ROI frame stack is autocorrelated in time. A circular averaging of the autocorrelation is also calculated when the dynamics of the system are isotropic. Non-uniformly distributed, immobile blinking fluorophore populations do not systematically affect the fluctuation defined autocorrelation. (C) Computed ACF (points) and simultaneous fits (lines) over five time-lags. (D) The process of computing the ACF and fitting is rapid (order of seconds for 64×64 pixel image series with 2048 frames) and outputs: the diffusion coefficient (D), the sum of the photoblinking rates (K), the fraction of time spent in the on-state (ρ_{on}), and the fraction of diffusing particles relative to all particles (f_D).

was originally developed for measuring transport parameters independently from the fluorophore photophysics. Similar to other ICS techniques, one of the underlying assumptions behind kICS is uniformity in space and time in the data being analyzed.[20]

Non-uniformity in space caused by the presence of immobile structures were commonly filtered out by either subtracting the time average, or equivalently, applying a Fourier filter. This solution does not work, however, when the fluorophores labeling these structures are undergoing photophysical processes *e.g.* photoblinking and photobleaching on timescales comparable to the imaging, thus making them difficult to analyze with traditional ICS methods. This is especially relevant in the context of SMLM and SOFI methods. Therefore, this significant extension of kICS is important for dealing with real heterogenities in space and time in the complex cellular environment.

We begin by showing that our definition of the autocorrelation is approximately independent of immobile particle positions. We then derive the autocorrelation for a mixed system of photoblinking immobile and diffusing particles that is independent of any direct imaging parameters in 2D, such as the point spread function (PSF). We proceed to demonstrate the accurate measurement of diffusion and photophysical parameters, when applying our technique on simulations. We then employ our method on Dronpa-labeled beta-actin (β-actin) imaged in live 3T3 and HeLa cells. Our measured diffusion coefficients for β-actin from these experiments are consistent with previously reported values. Furthermore, we observed that the photoblinking follows the expected dependence on excitation power in our HeLa cell experiments.

3.3 Theory

In the development of the original kICS technique by Kolin et al. (2006),[19] it was shown that diffusion and flow dynamics could be recovered regardless of the photophysical properties of the flurophores (*e.g.* photoblinking and photobleaching). However, the original method did not consider the presence of immobile particle populations also undergoing photophysical processes. We show here that with the presence of such populations, one cannot simply apply the original kICS analysis technique. We further derive an expression for the autocorrelation function (ACF) that we simultaneously fit for transport and photophysical parameters. This expression is independent of any direct imaging parameters in 2D (*e.g.* PSF size, amplitude, *etc*), as well as the immobile particle positions, allowing us to probe systems with complex immobile particle spatial arrangements and non-uniform cell morphologies. Furthermore, this enables us to maximize statistical spatial sampling when computing the ACF. This is in contrast with other image correlation techniques, which require spatially uniform regions for analysis.[20] Consequently, previous image correlation techniques would not be able to include cell boundaries and narrow

projections, such as dendritic spines and narrow cellular lamellae, such as dendritic projections, when choosing ROIs for analysis. The 2D model presented here can be used to model membrane dynamics sampled using TIRF microscopy, for example. We later extend this to the 3D case when analyzing the live 3T3 and HeLa cell data. We will refer to the developed technique as an extended kICS method.

We begin with the definition of a fluorescence microscopy image series of intensities in 2D, $i(\boldsymbol{r}, t)$:

$$i(\boldsymbol{r}, t) = \sum_{\alpha} i_s^{(\alpha)}(\boldsymbol{r}, t) + \epsilon(\boldsymbol{r}, t) = \sum_{\alpha} I(\boldsymbol{r}) \circledast_{\boldsymbol{r}} \rho^{(\alpha)}(\boldsymbol{r}, t) + \epsilon(\boldsymbol{r}, t), \tag{3.1}$$

where $i_s^{(\alpha)}(\boldsymbol{r}, t)$ is the fluorescence intensity from the labeled particles at position $\boldsymbol{r}$ and time t, belonging to population α with common transport parameters; $I(\boldsymbol{r})$ is the PSF; $\circledast_{\boldsymbol{r}}$ is a spatial convolution; $\epsilon(\boldsymbol{r}, t)$ is an additive noise term, which is assumed to be independent from itself for any $(\boldsymbol{r}, t) \neq (\boldsymbol{r}', t')$; and $\rho^{(\alpha)}(\boldsymbol{r}, t)$ is the apparent particle density of population α, *i.e.*, the density of particles in population α that are emitting and detectable. Note we only consider dependence of population α on particle position in this work. The apparent density of particles belonging to population α is given by:

$$\rho^{(\alpha)}(\boldsymbol{r}, t) = \sum_{m} q_{m,t} \Theta_{m,t} \delta(\boldsymbol{r} - \boldsymbol{u}_{m,t}^{(\alpha)}). \tag{3.2}$$

In this last equation, $\delta(\cdot)$ is the 2-dimensional Dirac delta function; m is an index denoting the fluorophores (which we also refer to as "particles"); $q_{m,t}$ is the instantaneous rate of detector counts for the m^{th} fluorophore at time t, which depends on several factors, including the photon budget, quantum efficiency of the detector, and camera detector gain; $\boldsymbol{u}_{m,t}^{(\alpha)}$ is the position of the m^{th} fluorophore at time t (belonging to population α), and $\Theta_{m,t}$ is its photo-emissive state, expressed as:

$$\Theta_{m,t} = \begin{cases} 1 & m^{\text{th}} \text{ particle is fluorescing at time } t \\ 0 & \text{not emitting} \end{cases}. \tag{3.3}$$

Note we do not consider photophysical transitions between singlet states (*i.e.*, absorption/emission and quenching), as these are far beyond the time-resolution capabilities of electron multiplying charge-coupled device (EMCCD) camera detectors.

Since we developed this approach for widefield fluorescence microscopy, we account for faster processes by also considering the effects of camera detector integration time by

substituting:[30]

$$i(\boldsymbol{r},t) \to \int_{t}^{t+\tau_i} \mathrm{d}s\, i(\boldsymbol{r},s), \tag{3.4}$$

with τ_i being the integration time (in this work, we consider $\tau_i = 1$); however, we leave the integration out of the notation, as it is straightforward to redo the derivation with it.

Defining the spatial Fourier transform as $\tilde{f}(\boldsymbol{k}) \equiv \int \mathrm{d}\boldsymbol{r} \exp(-i\boldsymbol{k}\cdot\boldsymbol{r}) f(\boldsymbol{r})$, we have the Fourier counterparts of Eqs. (3.1) and (3.2); respectively,

$$\tilde{i}(\boldsymbol{k},t) = \tilde{I}(\boldsymbol{k}) \sum_{\alpha} \tilde{\rho}^{(\alpha)}(\boldsymbol{k},t) + \tilde{\epsilon}(\boldsymbol{k},t), \tag{3.5}$$

and,

$$\tilde{\rho}^{(\alpha)}(\boldsymbol{k},t) = \sum_{m} q_{m,t}\Theta_{m,t} \exp\left(-i\boldsymbol{k}\cdot\boldsymbol{u}_{m,t}^{(\alpha)}\right). \tag{3.6}$$

In this work, we calculate the autocorrelation as:

$$\tilde{\phi}(\boldsymbol{k},\tau) \equiv \langle \delta_t\tilde{i}(\boldsymbol{k},t)\delta_t\tilde{i}^*(\boldsymbol{k},t+\tau)\rangle_t. \tag{3.7}$$

Practically, the above autocorrelation is realized by computing a time average, therefore we use the notation $\langle \ldots \rangle_t$ to denote an expectation value that only considers random variables that depend on time to be random. We also define δ_t as a fluctuation with respect to the time average, *i.e.*,

$$\delta_t\tilde{i}(\boldsymbol{k},t) \equiv \tilde{i}(\boldsymbol{k},t) - \langle\tilde{i}(\boldsymbol{k},t)\rangle_t. \tag{3.8}$$

Note in the original kICS work,[19] the autocorrelation was defined without the fluctuations. In the Supporting Information (SI), we show that the original definition leads to noisy autocorrelations affected by the immobile blinking particle positions (see SI: Comparison with original kICS method). Using the Fourier transform of an image series in Eq. (3.5), we can express the autocorrelation in Eq. (3.7) as:

$$\begin{aligned}\tilde{\phi}(\boldsymbol{k},\tau) = |\tilde{I}(\boldsymbol{k})|^2 \sum_{\alpha,\beta} \langle \delta_t\tilde{\rho}^{(\alpha)}(\boldsymbol{k},t)\delta_t\tilde{\rho}^{*(\beta)}(\boldsymbol{k},t+\tau)\rangle_t + \langle \delta_t\tilde{\epsilon}(\boldsymbol{k},t)\delta_t\tilde{\epsilon}^*(\boldsymbol{k},t+\tau)\rangle_t \\ + \left\{ \tilde{I}(\boldsymbol{k}) \sum_{\alpha} \langle \delta_t\tilde{\rho}^{(\alpha)}(\boldsymbol{k},t)\delta_t\tilde{\epsilon}^*(\boldsymbol{k},t+\tau)\rangle_t + \tilde{I}^*(\boldsymbol{k}) \sum_{\alpha} \langle \delta_t\tilde{\rho}^{*(\alpha)}(\boldsymbol{k},t+\tau)\delta_t\tilde{\epsilon}(\boldsymbol{k},t)\rangle_t \right\}.\end{aligned} \tag{3.9}$$

The terms in the curly brackets are zero, assuming noise and particle positions are independent. We show in SI: Noise autocorrelation that the autocorrelation of the noise

(*i.e.*, the second term) only affects $\tau = 0$ by a constant offset, which we will denote by $\tilde{\phi}_\epsilon$. Note $|\boldsymbol{k}|^2 = 0$ is also affected by the noise, but is omitted from the analysis.

Using Eq. (3.6), for immobile populations we have:

$$\delta_t \tilde{\rho}^{(\alpha)}_{\text{imm}}(\boldsymbol{k}, t) = q \sum_m \delta_t \Theta_{m,t} \exp\left(-i\boldsymbol{k} \cdot \boldsymbol{u}^{(\alpha)}_m\right), \tag{3.10}$$

where we have assumed all fluorophores have equal quantal brightness (*i.e.*, $q_{m,t} = q$). Note further that the time indexing is dropped for immobile particle positions so that they are unaffected by the time averaging. Conversely, for mobile populations:

$$\delta_t \tilde{\rho}^{(\alpha)}_{\text{mob}}(\boldsymbol{k}, t) = q \sum_m \Theta_{m.t} \exp\left(-i\boldsymbol{k} \cdot \boldsymbol{u}^{(\alpha)}_{m,t}\right), \tag{3.11}$$

since $\left\langle \exp\left(-i\boldsymbol{k} \cdot \boldsymbol{u}^{(\alpha)}_{m,t}\right)\right\rangle_t = 0$ for $|\boldsymbol{k}| \neq 0$, assuming the mobile particle positions are uniformly distributed in space within the chosen ROI.

Using Eqs. (3.10) and (3.11), Eq. (3.9) for one mobile and one immobile population becomes:

$$\begin{aligned}\tilde{\phi}(\boldsymbol{k}, \tau) = q^2 |\tilde{I}(\boldsymbol{k})|^2 \times \\ \Bigg\{ \underbrace{\sum_{m=n}^{N_{\text{imm}}} \langle \delta_t \Theta_{m,t} \delta_t \Theta_{n,t+\tau} \rangle_t + \sum_{m \neq n}^{N_{\text{imm}}} \langle \delta_t \Theta_{m,t} \rangle_t \langle \delta_t \Theta_{n,t+\tau} \rangle_t \exp\left(-i\boldsymbol{k} \cdot (\boldsymbol{u}_m - \boldsymbol{u}_n)\right)}_{\text{immobile}} \\ + \underbrace{\sum_{m=n}^{N_{\text{mob}}} \langle \Theta_{m,t} \Theta_{n,t+\tau} \rangle_t \left\langle \exp\left(-i\boldsymbol{k} \cdot (\boldsymbol{u}_{m,t} - \boldsymbol{u}_{n,t+\tau})\right)\right\rangle_t}_{\text{mobile}} \Bigg\} + \tilde{\phi}_\epsilon \delta_{\tau,0},\end{aligned} \tag{3.12}$$

where we have assumed non-identical particles are mutually independent, so that we can sum their individual autocorrelations, and $\delta_{\tau,0}$ is the Kronecker delta function. Note the fluctuations are not necessarily expected to vanish in the second term since, in practice, they are computed by subtracting the sample time average, which does not converge to the ensemble average in non-ergodic systems. Furthermore, subtraction by the spatial average only affects the autocorrelation at $|\boldsymbol{k}| = 0$. Notice also the second term is affected by the immobile particle positions, which is why we need to define conditions when it is approximately zero. It is clear that without photobleaching (or any other non-stationary photophysical process) the photophysical fluctuations are indeed zero on average; however, in the presence of bleaching the fluctuations need to be properly defined to make sure the second term in Eq. (3.12) is approximately zero. For this reason,

we use *local* time-averaging over a subset time-window to compute Eq. (3.8) in practice (see "Autocorrelation computation" in Materials and Methods), *i.e.*,

$$\delta_t\tilde{i}(\boldsymbol{k},t) = \tilde{i}(\boldsymbol{k},t) - \frac{1}{T_\mathrm{w}}\sum_{s=t}^{t+T_\mathrm{w}-1}\tilde{i}(\boldsymbol{k},s), \tag{3.13}$$

where T_w is the window size chosen for the local time average. If the photobleaching is slow and T_w is large enough, then Eq. (3.8) is a good approximation of Eq. (3.13). On the other hand, if the photobleaching is significant one must account for T_w in the autocorrelation (see SI: Time-windowed correction, where we provide an expression for this correction). Eq. (3.8) will also not hold when the dynamics in the system are slow and resemble immobility; in this case, the effects of time-windowing should again be accounted for (for example, see Figure 3.2 (C)). Note that if the second term in Eq. (3.12) is zero, then the autocorrelation is independent of any assumptions on immobile particle positions, making it a powerful tool to study previously inaccessible systems using image correlation. Time-windowed or moving-average subtraction has been previously used in raster ICS (RICS) as a way to filter out slow-moving fluorescent objects.[22, 37]

In order to obtain a quantity that is independent of PSF, we define the autocorrelation function (ACF) as:

$$\tilde{\Phi}(|\boldsymbol{k}|^2,\tau) \equiv \frac{\tilde{\phi}(|\boldsymbol{k}|^2,\tau)}{\tilde{\phi}(|\boldsymbol{k}|^2,\tau=0) - \lim_{|\boldsymbol{k}|^2\to\infty}\tilde{\phi}(|\boldsymbol{k}|^2,\tau=0)}. \tag{3.14}$$

The second term in the denominator removes dependence of the ACF on the noise; practically, it is computed as the large $|\boldsymbol{k}|^2$ offset in the autocorrelation. Furthermore, if the mobile components of the system being analyzed are isotropic, one can circularly average the autocorrelations for statistical sampling purposes.[19, 20, 38] Since the focus of this work will be on such systems, the dependence of the ACF in this last equation is left to be on $|\boldsymbol{k}|^2$. It should also be mentioned that this definition of the ACF leads to division by zero after sufficient decay of the PSF, so that the ACF must be appropriately trimmed in $|\boldsymbol{k}|^2$ prior to fitting. For a 2D mixture of diffusing and immobile particles, Eq. (3.14) can be written explicitly as:[19, 30, 39]

$$\tilde{\Phi}(|\boldsymbol{k}|^2,\tau) = \frac{f_D\left(\rho_\mathrm{on} + (1-\rho_\mathrm{on})e^{-K\tau}\right)e^{-|\boldsymbol{k}|^2D\tau} + (1-f_D)(1-\rho_\mathrm{on})e^{-K\tau}}{1-(1-f_D)\rho_\mathrm{on}}, \tag{3.15}$$

where D is the diffusion coefficient; $K \equiv k_\mathrm{on} + k_\mathrm{off}$ is the sum of the photoblinking rates, where k_on and k_off are the on- and off-blinking rates, respectively; ρ_on is the fraction of

time spent in the fluorescent on-state; and f_D is the fraction of particles diffusing. Note that the blinking in this last expression is assumed to follow a two-state on-off model, without photobleaching. In the SI, we include a derivation considering the effects of bleaching and detector time-integration, as well as a derivation for the 3D effects on the ACF (see SI: Autocorrelation function derivation).

3.4 Results and Discussion

3.4.1 Computer simulations

We first apply our extended kICS method on 2D computer simulations of immobile filamentous structures composed of fixed emitting particles, with a second simulated population of freely diffusing particles, as shown in Figure 3.2. The fit results from this figure are tabulated in Table 3.1. The fitted parameters demonstrate the wide range of diffusion coefficients that are measurable in heterogeneous morphologies using our extended technique.

The simulations assumed both immobile and diffusing particle populations to have the same photoblinking and photobleaching rates. Each simulation also contained simulated EMCCD noise (see Sehayek *et al.* (2019)[30] for noise model details). We note that our method is not limited to analyzing EMCCD data and could also be applied to data acquired by other camera detectors used in widefield setups. This is because we considered the exposure time of each frame when deriving the ACF (see Eq. (3.4)). Examples of other such detectors are scientific complementary metal-oxide-semiconductors (sCMOS) cameras and single-photon avalanche diode (SPAD) arrays, both of which have been used in multiplexed FCS studies.[40, 41] An extension of our method to sCMOS data would most likely require characterization of spurious correlations from hot pixels characteristic of such cameras, but this should be possible using a camera specific masking operation. As well, recent work by Mandracchia *et al.* (2020)[42] presents an adaptive algorithm approach to correct for noise characteristic of sCMOS cameras and such an approach may be useful before performing kICS.

Note the non-uniformity in the immobile particle positions placed along the simulated filaments in Figure 3.2, which confirms that the technique can be successfully applied in non-homogeneous systems. Conversely, previous image correlation techniques required ROIs to be selected where the spatial distribution of particles was homogeneous *e.g.* avoiding cell boundaries (see SI: Comparison with original kICS method where we compare our extended kICS technique to the original one).[20] It would be impossible

to select such an ROI with both diffusing and immobile particles in the simulations shown in Figure 3.2. The ability to analyze larger ROIs further enables us to increase the spatial sampling in our analyses; however, we assume that all the particles within this ROI have transport and photophysical parameters that are drawn from common distributions, *i.e.*, we assume a single diffusing population and a single photophysical population (while the extension to multiple populations with different dynamic parameters is possible, one must be mindful of the possibility of overfitting). Thus, our analysis offers a coarse-grained approach for quickly measuring these parameters within regions. SPT is beneficial when a common distribution cannot be assumed for such parameters. However, the fluorescence correlation approach can be applied to cell expression systems where high density labeling might not permit SPT. SPT is also limited by factors such as photoblinking in transport populations.

In Figure 3.2 (B), the shape of the ACF is characterized by a decay at low $|\boldsymbol{k}|^2$, and a convergence to a non-zero value at higher $|\boldsymbol{k}|^2$. The former is attributed to the diffusion coefficient, while the latter is due to the presence of an immobile particle population, as can be seen from Eq. (3.15) (note that these fits use the time-integrated version of this equation; see SI: Autocorrelation function derivation for details). The decrease in the ACF amplitude and offset with increasing time-lag is due to the photophysical processes in the system, *i.e.*, photoblinking and photobleaching.

When the ACF is characterized by an initial increase along $|\boldsymbol{k}|^2$, as is the case in Figure 3.2 (C), one needs to account for the effect of the sliding time-window (see SI: Time-windowed correction). This type of behavior occurs when the diffusion is relatively slow, or when the chosen time-window is relatively short.

In Figure 3.2 (D), we show sample images from a simulation with more noise. Specifically, we increased the simulated autofluorescence background, while decreasing the photon budget of the simulated fluorophores. To accurately analyze such an image series (Figure 3.2 (E)), we required larger ROIs than the ones used in the previous analyses. Consequently, we generated this simulation on a 256×256 pixel grid.

Note that photobleaching was not considered in the fits shown in Table 3.1. A derivation considering the effects of bleaching on the ACF is included in SI: Time-windowed correction. Although one can consider these effects, we have demonstrated that we can still obtain accurate parameters in the presence of photobleaching, without having to incorporate it into our fit model (given appropriate choice of time-window). This is beneficial as bleaching pathways of a fluorescent label are not often known.

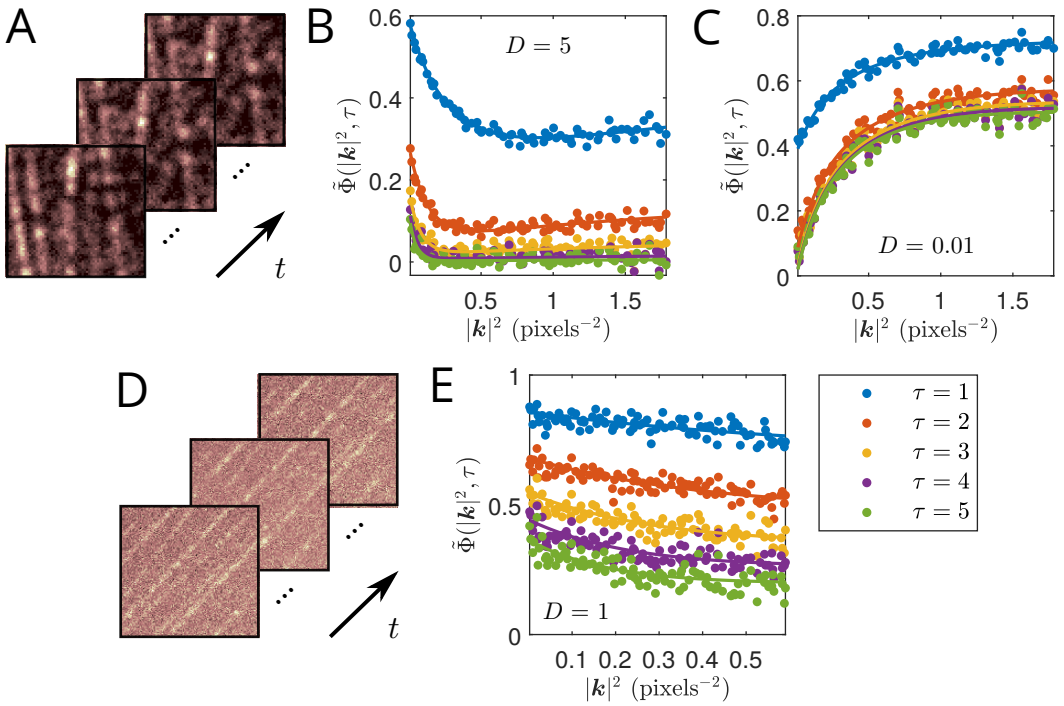

FIGURE 3.2: Example ACFs and fits computed from simulations of filamentous structures composed of static blinking particles, with a second population of freely diffusing particles. Both populations are set to have the same photophysical properties. Each simulation also contained simulated EMCCD noise. The ACF fits were all done over the first 10 time-lags; only the first 5 are shown. Time windowing was done with $T_\mathrm{w} = 200$ frames in each case. Simulation and fit details are shown in Table 3.1. (A) Example of simulated intensity images in time. (B, C) Computed ACFs (points) and corresponding simultaneous fits (lines) for simulations with $D = 5$ and 0.01 pixels^2/frame, respectively. In (C), we utilize a fit model that corrects for the chosen sliding time-window. (D) Sample simulation with higher simulated autofluorescence background and lower photon budget than simulation shown in (A). (E) Corresponding computed ACF and fit of simulation shown in (D) with $D = 1$ pixels^2/frame.

We also note that the fraction of time spent in the on-state, ρ_on, cannot be measured for a purely immobile population, *i.e.*, $f_D = 0$. This can be seen by the lack of dependence on ρ_on in Eq. (3.15) in this limit. Previous techniques have described how to measure the photoblinking rates for immobile emitters.[30, 43–46]

To perform our analysis, it is essential to choose a time-window, an ROI, a range of time-lags to fit simultaneously, and cutoff values for $|\boldsymbol{k}|^2$. As discussed in the Theory section above, the choice of time-window will mainly depend on the photobleaching rate. A value of T_w that is too small results in loss of information, but a smoother ACF. A value of T_w that is too large will result in a noisier ACF that is more influenced by the photobleaching, which may lead to poorer fits. With a simulated bleaching rate of $k_\mathrm{p} = 10^{-4}$ frames^{-1} (with a frame acquisition time of 50 ms, this corresponds to a

characteristic bleaching time of 500 s), we find a suitable choice of time-window to be $T_w = 200$ frames. We will use this value consistently throughout this work for the same value of k_p. The same value of T_w can be used for smaller bleaching rates. In general, we found from our simulations that T_w can be chosen to be about 2–5% of the characteristic bleaching time.

As mentioned above, when choosing an ROI it is necessary to select a relatively large region, in order to avoid aliasing of the ACF along $|\boldsymbol{k}|^2$. This is especially important when dealing with larger diffusion coefficients, as the decay will appear in a short range of small $|\boldsymbol{k}|^2$.

	Fig. 3.2 (B)		Fig. 3.2 (C)	
	Fit	Simulation	Fit	Simulation
D (pixels^2·frame^{-1})	4.66 ± 0.06	5	0.0113 ± 0.0001	0.01
K (frame^{-1})	1.02 ± 0.02	1	1.68 ± 0.01	1.7
ρ_{on}	0.095 ± 0.006	0.1	0.59 ± 0.01	0.59
f_D	0.68 ± 0.03	0.7	0.59 ± 0.02	0.65

	Fig. 3.2 (E)	
	Fit	Simulation
D (pixels^2·frame^{-1})	1.12 ± 0.07	1
K (frame^{-1})	0.284 ± 0.006	0.3
ρ_{on}	0.36 ± 0.03	0.33
f_D	0.36 ± 0.06	0.35

TABLE 3.1: Comparison of fitted and simulated parameters for fits shown in Figure 3.2.

Each simulation had photobleaching rate $k_p = 10^{-4}$ frame^{-1} over $T = 2048$ frames. Simulations (B) and (C) were generated on 128×128 pixel grids, while (E) was on a 256×256 pixel grid. The simulations were assigned 8130, 8411, 9048 total particles, respectively. In each case, fitted parameters and errors were obtained by splitting the simulation spatially into 4 equally sized and independent ROIs and then calculating the mean and its standard error from their analyses.

Similarly, when choosing a range of time-lags to fit, it is best to choose a wide range, in order to capture slower dynamics. If the range is too large, the simultaneous fitting will be visibly biased and a smaller range should then be used. Trying to fit a larger time-lag range can be complicated by the presence of photobleaching, for example (we show how to account for these effects in SI: Time-windowed correction). We also remark that the ACF is noisier for higher time-lags, so that it is informative to compare them with their fits to gauge whether the fitted time-lag range is too wide. We showed that we can achieve reasonable fits for our simulated parameters by fitting the 10 first time-lags in

our analyses in Table 3.1. Systematic errors were reduced when including more time-lags in the fit, or when choosing larger ROIs, but in non-simulated data, it may be difficult to make such adjustments.

Finally, we discuss choosing cutoff values for $|\boldsymbol{k}|^2$. We discard the value of the ACF at $|\boldsymbol{k}|^2 = 0$ since it is affected by the noise in the system, as was mentioned in the Theory section. Excluding a few small $|\boldsymbol{k}|^2$ is also beneficial for avoiding the autocorrelation from the time-windowing, when not using the time-window correction (see SI: Time-windowed correction for details). The maximum value for $|\boldsymbol{k}|^2$ can be selected by examining where the ACF begins to diverge due to the normalization in Eq. (3.14). It is optimal to choose the largest possible range of $|\boldsymbol{k}|^2$ to fit while avoiding points that are too noisy due to the normalization. Choice of the maximum cutoff will depend on PSF size as well as the noise in the system. As was previously mentioned, this is to avoid division by zero that occurs due to our definition of the ACF in Eq. (3.14). This occurs because the noise is subtracted from the denominator, which is then effectively zero after the PSF has sufficiently decayed. In Figure 3.2 (E), due to the higher noise in the simulation, the fit has a smaller chosen maximum cutoff of $|\boldsymbol{k}|^2$ since higher values result in a divergence of the ACF.

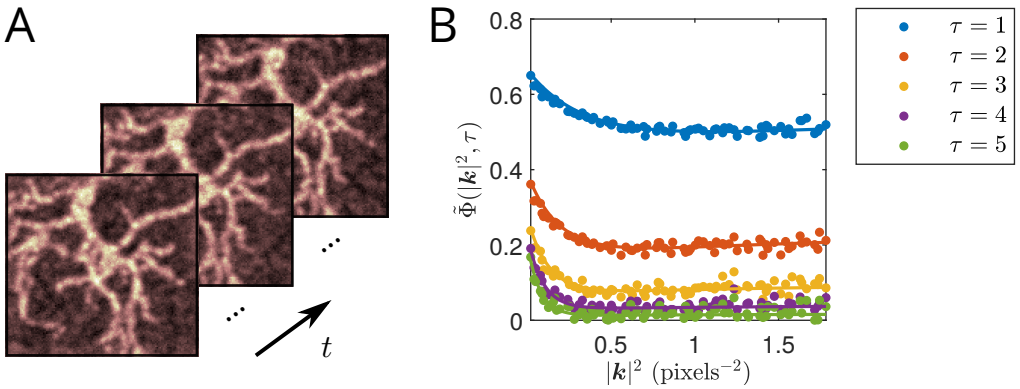

FIGURE 3.3: Example ACF computed from simulation of dendritic structures and fit. (A) Sample simulated intensity images in time. Simulations contain immobile particles on the dendrites, along with a background of freely diffusing particles. Both populations are assumed to have equal photophysical properties. (B) Computed ACF (points) and corresponding simultaneous fit (lines). The fit is done over the first 10 time-lags; only first 5 are shown. Time windowing was done with $T_\mathrm{w} = 200$ frames. Fit details are shown in Table 3.2.

In Figure 3.3, we perform the same analysis on a simulated dendritic morphology. A comparison of the simulated and fitted parameters recovered using our analysis is shown in Table 3.2. This further demonstrates the ability of the technique to be applied independently of immobile particle distribution. In this case, it would again be impossible to

select an ROI containing a uniform distribution of both diffusing and immobile populations for analysis using previous image correlation techniques. As mentioned previously, with the extended kICS technique developed in this work, we are no longer restricted by this requirement and can further benefit from large ROIs to increase the spatial sampling in our analysis.

	Fit	Simulation
D (pixels^2·frame^{-1})	2.80 ± 0.08	3
K (frame^{-1})	0.86 ± 0.01	0.9
ρ_{on}	0.38 ± 0.03	0.44
f_D	0.26 ± 0.02	0.3

TABLE 3.2: Comparison of fitted and simulated parameters for fits shown in Figure 3.3.

Simulation had photobleaching rate $k_{\text{p}} = 10^{-4}$ frame^{-1} and was generated on 128×128 pixel grid with 10744 total particles and $T = 2048$ frames. Fitted parameters and errors were obtained by splitting the simulation spatially into 5 64×64 ROIs, with some overlap between different parts, and then calculating the mean and its standard error from their analyses. The ROIs were chosen so that a significant portion of the simulated dendritic structure was encompassed, overall.

3.4.2 Live NIH/3T3 cell data

Using a widefield fluorescence microscope equipped with an EMCCD camera detector, we imaged β-actin labled with Dronpa-C12 in an NIH/3T3 fibroblast cell line expression system. The Dronpa-C12 exhibited blinking and photobleaching during image aquisition and the β-actin pool was both diffusively mobile within the cell and immobile in actin filaments. A sample of our analysis from the data is shown in Figure 3.4.

In Figure 3.4 (C), we reconfirm that the blinking of immobile fluorophores can be used to obtain a SOFI[8] image using SOFI 2.0[47, 48] (see GitHub code for SOFI 2.0). Along with our dynamic analysis of this data, we demonstrate that we can extract both static and dynamic information from our system with careful selection of correlation analysis approaches.

Since the data was acquired using a widefield fluorescence microscope with actin monomers diffusing in the cytoplasm, we needed to employ a 3D model for the ACF fit (see SI: Diffusing and immobile populations (3D) for more details). The extension to a 3D model (without considering integration time effects) is achieved through a scaling factor that depends on τ, and consequently, does not affect the behavior of the ACF along $|\boldsymbol{k}|^2$. Using the 2D fit model for the ACF yielded visibly inconsistent fits to the data. Notably, our reported value for the apparent diffusion coefficient (9.2 ± 0.4 µm$^2 \cdot$ s^{-1}) is

within range of the simulated and experimentally verified diffusion coefficient of globular actin (G-actin) in the cytoplasm of $\sim$ 3–30 $\mu m^2 \cdot s^{-1}$.[49–53] This is also in reasonable agreement with the diffusion coefficient of Dronpa-labeled actin in an MCF-7 cell of 13.7 $\mu m^2 \cdot s^{-1}$, reported by Kiuchi *et al.* (2011)[52] Our measurement of a relatively rapid diffusion coefficient is further confirmed by the behavior of the ACF, which exhibits a characteristic initial decay in $|\boldsymbol{k}|^2$, as in Figure 3.2 (B). This is in contrast to systems with lower diffusion coefficients, which exhibit an initial increase in $|\boldsymbol{k}|^2$, as in Figure 3.2 (C). As can also be seen from Figure 3.4, our assumption of a single diffusing population provides a reasonable fit to the data. Therefore, we argue that it would not be advantageous to include more diffusing components in our fit model since it would risk overfitting our data.

In order to account for 3D effects, we needed to first estimate the e^{-2} radius along the axial direction from the data. To this end, we used the Abbe resolution criterion to determine the full width at half maximum of the PSF in z, *i.e.*, $2\lambda/\mathrm{NA}^2$, which was then converted to an e^{-2} radius.

McGrath *et al.* (1998)[49] demonstrated that they can simultaneously measure actin filament turnover rate, fraction of actin in filaments and actin diffusion using either fluorescence recovery after photobleaching (FRAP) or photoactivation of fluorescence (PAF). In their model, the filamentous actin is not necessarily immobile, but not diffusing. We show that on the time and spatial scales we considered in our analysis, the actin flow is negligible. Furthermore, filament turnover rate is an important parameter at filament ends, but we chose ROIs away from these ends, so that we would not have to consider such effects.

Since flow appears as an imaginary component in the autocorrelation,[19] we compared the magnitude of the imaginary part to that of the modulus of the autocorrelation, *i.e.*,

$$\frac{\left|\Im\left(\tilde{\phi}(\boldsymbol{k},\tau)\right)\right|}{\left|\tilde{\phi}(\boldsymbol{k},\tau)\right|}. \tag{3.16}$$

This quantity was determined to be very small (close to machine precision), confirming that the flow is negligible relative to other dynamics over the time and spatial scales examined.

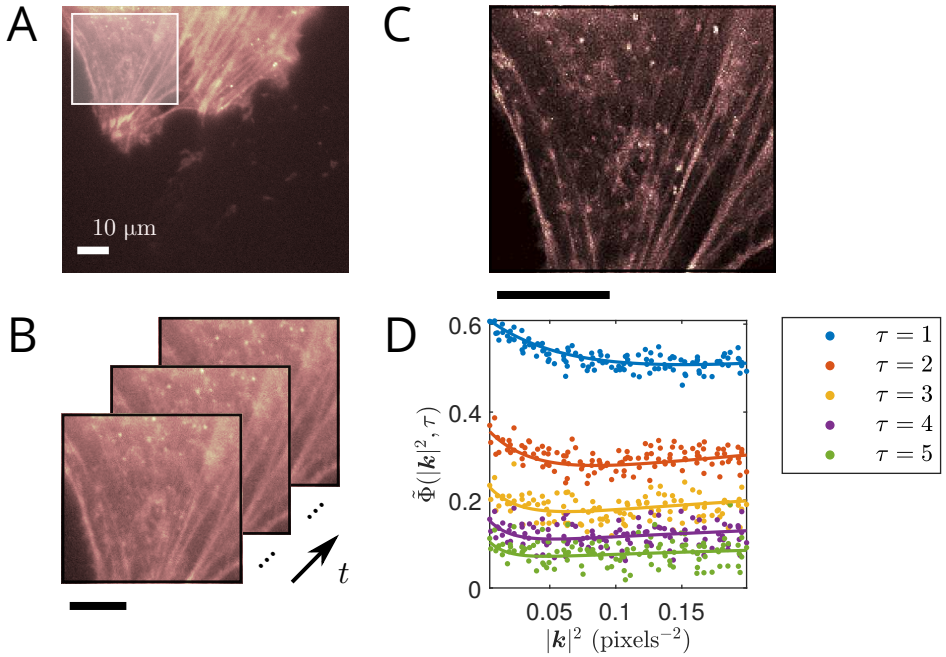

FIGURE 3.4: ACF computed from Dronpa-C12 labeled actin in a live NIH/3T3 cell and fit. (A) Fluorescence image of Dronpa-C12 labeled actin in a live NIH/3T3 cell, with ROI used in analysis highlighted. (B) Sample fluorescence images in time of ROI shown in (A). (C) SOFI image generated from immobile blinking fluorophores (see GitHub code for SOFI 2.0). (D) Computed ACF from ROI shown in (A) (points) and corresponding simultaneous fit (lines). The fit was done over the first 5 time-lags. Time-windowing was done with $T_w = 100$ frames. Fitted parameters: $D = 9.2 \pm 0.4\ \mu m^2 \cdot s^{-1}$, $K = 7.6 \pm 0.4\ s^{-1}$ and $f_D = 0.58 \pm 0.03$. Fit for ρ_{on} omitted due to inconsistent values between different ROIs and TOIs. Pixel size: 177.78 nm. Frame time: 50 ms. Analysis details: Two spatially independent ROIs (each about $30 \times 30\ \mu m^2$) over two temporally independent TOIs (each about 50 s in length) were considered in the analysis. The reported fitted parameters and errors are given as the mean and its standard error from these analyses.

From our analysis of the data shown in Figure 3.4, we also found a diffusing fraction of $f_D = 0.58 \pm 0.03$. Gasilina *et al.* (2019)[54] reported a percentage of filamentous actin (F-actin) of $48 \pm 4\%$ from their immunoblotting-based analysis of wild type NIH/3T3 fibroblast cells. If we assume F-actin to be immobile and G-actin to be diffusing, then this value corresponds to $f_D = 0.52 \pm 0.04$.

We further tested whether the G-actin was undergoing anomalous subdiffusion in the cell. This can approximately be done by replacing the dependence of the ACF from $\tau \to \tau^\alpha$ (ignoring detector time integration), where α is the degree of subdiffusion.[34] A fit including α as a free parameter yielded a fitted value of $\alpha \sim 1$, indicating that the diffusion of the G-actin within this non-migrating cell was mainly free diffusion.

3.4.3 Live HeLa cell data

We proceeded to analyze Dronpa-C12 labeled β-actin in live HeLa cells imaged under different excitation intensities. Our analyses are shown in Figure 3.5, with results given in Table 3.3 below.

Measurements of the apparent diffusion coefficient from the HeLa cells are again within the range of $\sim$ 3–30 $\mu m^2 \cdot s^{-1}$ for G-actin diffusion in cytoplasm. Furthermore, the diffusion coefficients are about the same as we measured in the 3T3 fibroblast cell. The diffusion coefficient measured from the low power dataset, however, is lower than the ones measured at higher powers. One possible explanation for this observation is the lower excitation power would lead to lower excitation probabilities, especially outside of the focal plane. As such, the signal-to-noise ratio (SNR) may not be sufficient to detect as many of the fluorescent proteins diffusing in 3D away from the focal plane, thus reducing the measured apparent diffusion coefficient (these events might be characterized by our analysis as photoblinking, for instance).

We also observed that the sum of the photoblinking rates, K, decreased and on-time fraction, ρ_{on}, increased consistently with decreasing excitation intensity. Computing the mean on-time residency from Table 3.3 we obtained $t_{\text{on}} = 81 \pm 3$ ms at full excitation power and $t_{\text{on}} = 118 \pm 1$ ms at medium excitation power (note, we use the convention $k_{\text{off}} \equiv 1/t_{\text{on}}$). We also calculated the mean off-time to be $t_{\text{off}} = 99 \pm 6$ ms at full excitation and $t_{\text{off}} = 113 \pm 7$ ms at medium excitation. The increasing on-time with decreasing excitation intensity, as well as the roughly constant off-time, is characteristic behavior of any fluorophore because of the long-lived triplet state (or any similar dark state that depletes the ground singlet state).[55] This effect on the photoblinking rates as a function of excitation power was also observed in wild type Dronpa.[56]

We point out that Dronpa is expected to have a non-emissive state with a longer off-time,[56] while we found $t_{\text{on}} \simeq t_{\text{off}}$. In fact, Habuchi et al. (2005)[56] found that wild type Dronpa has three distinct dark states, of which one is significantly longer than the others. The t_{off} values we measured can, therefore, depend on the residency times of multiple off-states. We make a simplifying argument to illustrate why our measurement may not be able to detect a much longer off-time. In our technique, we explicitly have $\rho_{\text{on}} \equiv k_{\text{on}}/K$. If we now assume that k_{on} is a sum of two rates, say $k_{\text{on}}^{\text{slow}}$ and $k_{\text{on}}^{\text{fast}}$, such that $k_{\text{on}}^{\text{slow}} \ll k_{\text{on}}^{\text{fast}}$, then we have $\rho_{\text{on}} \simeq k_{\text{on}}^{\text{fast}}/K$. In other words, the rate corresponding to the longer time does not contribute to ρ_{on} and is thus not detected by our analysis.

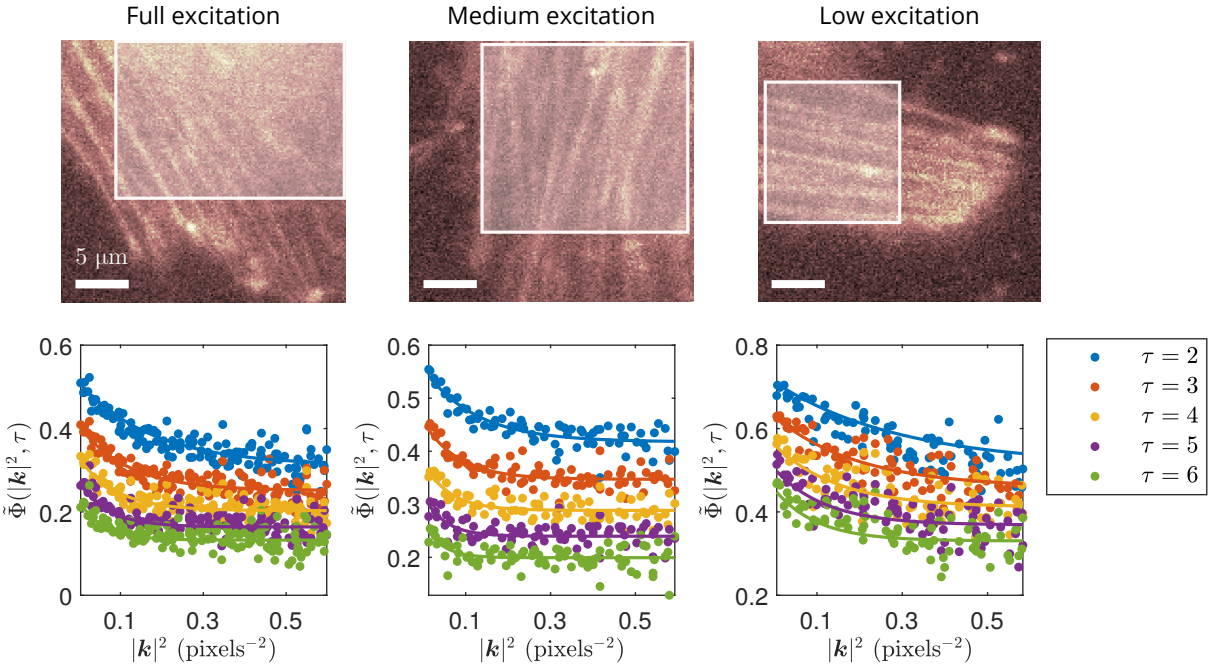

FIGURE 3.5: Example ACF analyses of independent HeLa cells irradiated at different excitation powers. Fluorescence images of Dronpa-C12 labeled actin in live HeLa cells, with ROI used in analyses highlighted, are shown on top part of figure. Corresponding computed ACFs from ROIs (points) and respective simultaneous fits (lines) are shown on bottom part of figure. The time lag ranges for the fits varied from $\tau = 2$ to either $\tau = 10$ or $\tau = 20$. Time-windowing was done with $T_{\mathrm{w}} = 100$ frames. Pixel size: 177.78 nm. Frame time: 10 ms. Image series length: 50 s.

At low power, the measured K is consistent with a longer on-time, assuming t_{on} is the only characteristic time that is a function of excitation intensity. Note we could not properly measure ρ_{on} and f_D for the low-power data as different fitting ranges of τ and $|\boldsymbol{k}|^2$ would significantly affect these fitted parameters. This is, once more, likely due to the lower SNR, causing the ACF to be noisier. In general, ρ_{on} and f_D varied most among the fitted parameters when fitting the ACF over different ranges.

We also found a mean value for the diffusing fraction of $f_D = 0.30 \pm 0.02$. Blikstad and Carlsson (1982)[57] have previously reported values of unpolymerized actin measured from HeLa cell homogenates between 35–45%.

Note the time-integrated 3D diffusion model did not fit our HeLa cell data well. This is possibly due to the non-negligible dead time ($\sim$ 1 ms) of the EMCCD camera detector relative to the shorter frame times used for imaging this data (10 ms). Instead of accounting for this effect in our model, we found that simply excluding the first time-lag from our analyses gave reasonable fits.

		D ($\mu m^2 \cdot s^{-1}$)	K (s^{-1})	ρ_{on}	f_D
Excitation Power	Full ($\sim$ 24 mW)	10.9	23.6	0.490	0.252
		8.89	21.4	0.451	0.376
		12.8	22.8	0.416	0.322
	Medium ($\sim$ 19 mW)	12.8	18.5	0.545	0.230
		10.9	16.6	0.495	0.323
		7.39	17.2	0.501	0.290
	Low ($\sim$ 14 mW)	5.31	10.9	—	—

TABLE 3.3: Fit parameters measured from independent HeLa cells at different excitation powers.

Different rows are ROI analyses of independent cells. Fits for ρ_{on} and f_D at low power were omitted due to inconsistent fitted values when using different τ and $|\boldsymbol{k}|^2$ fitting ranges.

3.5 Conclusions

We have presented an extended kICS fluorescence fluctuation rapid analysis method that simultaneously fits for the diffusion coefficient, photoblinking rates and fraction of diffusing particles from a fluorescence image series. This is done independently from any other parameters. Unlike other image correlation techniques, our current approach can be applied to regions with non-uniform fluorophore distributions, including complex cellular morphologies. This enables us to increase spatial sampling across areas of the cell, which improves the statistical precision of the ACF and extends the dynamic range for transport coefficient measurement. Furthermore, we have shown through physically realistic simulations that we can obtain accurate fit results in the presence of photobleaching, without having to consider its effects. We also demonstrated that our method can measure an apparent diffusion coefficient of Dronpa-C12 labeled actin in live NIH/3T3 and HeLa cell data that is consistent with previous literature values. We further observed that the fitted photoblinking parameters, measured from several independent HeLa cells, gave the expected trend as a function of excitation power. Lastly, our reported values for the diffusing fractions in both 3T3 and HeLa cells agree well with literature values. We anticipate that our technique will be useful in the study of dynamics in super-resolution, due to its ability to analyze more intricate systems than previous image correlation methods.

In the future, we plan to apply our method to measure biomolecular binding kinetics since photoblinking and mean-field binding/unbinding are virtually analogous processes mathematically (under certain assumptions). Another potential application could be to

use the measured photoblinking rates as probes for sensing changes in a cellular environment.

3.6 Materials and Methods

Live cell imaging

The NIH/3T3 fibroblast and Hela cells were transfected with plasmids containing either the Dronpa-C12 β-actin fusion protein or with Lipofectamine 2000 using the standard protocol. Prior to imaging, cell culture media was gently replaced into 1x PBS buffer warmed to 37°C. The cells with prominent actin stress fibers were empirically identified for imaging. The NIH/3T3 fibroblast cell data was imaged with acquisition time of 50 ms per frame and we observed slow detaching of its focal adhesion sites during the imaging time course. The same data appeared in previous work.[47] The HeLa cells were imaged at 10 ms per frame under excitation powers of ~ 14, ~ 19 and ~ 24 mW.

Imaging was performed with an inverted fluorescence microscope using widefield imaging mode (Nikon Eclipse Ti, Tokyo) equipped with an EMCCD camera (Andor iXon, model no. DU-897E-CSO-#BV) and a standard EGFP filter cube (460/60 nm band pass excitation filter, 495 nm long pass dichroic and 520/40 nm band pass emission filter). Excitation of 485/25 nm was used (cyan option, AURA light engine, ©Lumencor, Inc., Beaverton, OR, UCA). A 60x oil immersion objective (NA=1.4) was combined with an extra 1.5x magnification module integrated into the microscope body.

Computer simulations

Simulations were created and analyzed using MATLAB R2020a on a Dell XPS 9530 (Intel(R) Core™ i7 @ 2.3 GHz, 16 GB RAM) running Windows 10. Simulations were also created using MATLAB R2020a on a dedicated research server (Intel(R) Core™ i7 @ 3.2 GHz, 64 GB RAM) running Ubuntu version 18.04.

To simulate fluorophores on filaments, we first drew angles from a normal distribution with specified mean and standard deviation. This determined the direction of each filament in the synthetic image series. Then, starting from a filament's endpoint (randomly distributed along simulated image edges), particles were iteratively placed along the filaments with incremental distance (in pixels) drawn from a uniform distribution on $(0, 1)$. This process was repeated until the edge of the synthetic image was reached. Each time a simulated emitter was placed, a predefined probability determined whether the position

was occupied by an aggregate. Each simulated aggregate had an assigned mean number of fluorophores following a Poisson distribution, as well as a random distance from the aggregate center (mean position) following a normal distribution with a chosen standard deviation. Simulated diffusing particles were initialized randomly within the pixel grid and allowed to diffuse with periodic boundaries.

Synthetic emitters were subject to stochastic switching between on- and off-states at specified rates to simulate photoblinking. Photobleaching was assumed to be equal from the on/off-states in all simulations. Both populations of immobile and diffusing particles were simulated to have the same photoblinking and photobleaching rates.

We then convolved the simulated image series with a 2D Gaussian function (integrated over pixel dimensions) to simulate the optical PSF. To emulate the effect of the detector integration time, we split each frame into 50 "subframes", so that a single frame was comprised of a sum of its constituent "subframes". For more simulation details, we refer the reader to SI: Simulation details.

Synthetic pixel intensity values were assigned using the EMCCD model presented by Hirsch et al.,[58] as was previously described in Sehayek et al.[30]

The ACF was fitted to Eq. (3.24) in the SI, unless otherwise stated. The fitting model assumed one diffusing and one immobile population. The global fitting of the ACF was done using the built-in MATLAB object `GlobalSearch` with `fmincon` as a local solver. The fitted parameters were chosen according to the least-squares method across the specified domain of the ACF. All fitted parameters were constrained to be greater than zero, with the added conditions $\rho_{\text{on}}, p_D \leq 1$. We used uniformly drawn random numbers in the interval $(0, 1)$ as an initial guess for all fitted parameters to demonstrate the robustness of our method. In the case where the fit did not visually match the data, we repeated the fitting process until reasonable agreement was achieved. The fits always excluded the points $|\boldsymbol{k}|^2 = 0$, as they are affected by the noise in the system. The $\tau = 0$ curve was also excluded from our fits, as it does not contain any useful information when using the definition in Eq. (3.14). Our analyses were performed on several ROIs and/or TOIs. The reported fitted parameters and their errors were then taken to be the mean and the standard error on the mean from these analyses.

Autocorrelation computation

The autocorrelation was calculated as:

$$\tilde{\phi}(\boldsymbol{k}, \tau) = \frac{1}{T - \tau} \mathcal{F}_t^{-1} \left(\left| \mathcal{F}_t(\delta_{t,T_{\text{w}}} \tilde{i}(\boldsymbol{k}, t)) \right|^2 \right), \tag{3.17}$$

where $\mathcal{F}_t$ is the fast Fourier transform in time, and δ_{t,T_w} denotes the time-windowed fluctuation, as in Eq. (3.13); that is, at pixel (x, y) and frame t, we subtract the mean intensity of T_w subsequent frames, including frame t (we used MATLAB `movmean` function to do this). Defining the fluctuations in this way diminishes the oscillations caused by photobleaching (see SI: Comparison with original kICS method). The choice of T_w should, ultimately, depend on the photobleaching rate. Note that the Wiener-Khinchin theorem is used in Eq. (3.17) to minimize autocorrelation computation time *via* Fourier (reciprocal) space calculations.

The autocorrelation in Eq. (3.17) was then circularly averaged. This was done by averaging all autocorrelation points with the same value of $|\boldsymbol{k}|^2$. Finally, the ACF was computed as shown in Eq. (3.14). To determine the "large" $|\boldsymbol{k}|^2$ offset in the denominator of the equation, a range of $|\boldsymbol{k}|^2$ values were chosen after the $\tau = 0$ autocorrelation had sufficiently decayed and averaged over.

Supporting Material

- Comparison with original kICS method; autocorrelation function derivation: 2D, 3D, with time-windowed correction; simulation details; noise autocorrelation.
- kICS GitHub repository: `https://github.com/ssehayek/kics-project.git`
- SOFI 2.0 GitHub repository: `https://github.com/xiyuyi-at-LLNL/pysofi.git`

Author Contributions

- S.S. and P.W.W.: designed research, wrote the manuscript
- S.S.: developed theory for method, analyzed data, generated simulations
- X.Y. and S.W.: provided experimental data, provided SOFI analysis, contributed to method development

Acknowledgments

P.W.W. kindly acknowledges support of a Natural Sciences and Engineering Research Council of Canada (NSERC) Discovery Grant. S.W. was funded by the STROBE National Science Foundation Science and Technology Center, Grant No. DMR-1548924 and

by the National Science Foundation, Grant No. CMI-1808766. The work from X.Y. was performed under the auspices of the U.S. Department of Energy by Lawrence Livermore National Laboratory under Contract DE-AC52-07NA27344. Release number: LLNL-JRNL-816054. Special thanks to Paul De Konick (Laval University) for providing us with an image of a branched neuron, which was used for generating simulations.

3.7 Supporting Information

Comparison with original kICS method

As discussed in the main text, applying the original kICS method[19] to an image series with an immobile blinking population yields oscillations in the ACF. The original technique defined the kICS autocorrelation without the temporal fluctuations, *i.e.*,

$$\tilde{\phi}_{\text{orig}}(\boldsymbol{k},\tau) \equiv \langle \tilde{i}(\boldsymbol{k},t)\tilde{i}^{*}(\boldsymbol{k},t+\tau)\rangle_{t}. \tag{3.18}$$

Using this definition, one can follow the same steps used to derive Eq. (3.12) in the main text to instead obtain:

$$\begin{aligned}\tilde{\phi}_{\text{orig}}(\boldsymbol{k},\tau) = q^{2}|\tilde{I}(\boldsymbol{k})|^{2}\times \\ \Bigg\{ \underbrace{\sum_{m=n}^{N_{\text{imm}}} \langle \Theta_{m,t}\Theta_{n,t+\tau}\rangle_{t} + \sum_{m\neq n}^{N_{\text{imm}}} \langle \Theta_{m,t}\rangle_{t}\langle \Theta_{n,t+\tau}\rangle_{t} \exp\left(-i\boldsymbol{k}\cdot(\boldsymbol{u}_{m}-\boldsymbol{u}_{n})\right)}_{\text{immobile}} \\ + \underbrace{\sum_{m=n}^{N_{\text{mob}}} \langle \Theta_{m,t}\Theta_{n,t+\tau}\rangle_{t} \left\langle \exp\left(-i\boldsymbol{k}\cdot(\boldsymbol{u}_{m,t}-\boldsymbol{u}_{n,t+\tau})\right)\right\rangle_{t}}_{\text{mobile}} \Bigg\} + \tilde{\phi}_{\epsilon}\delta_{\tau,0}.\end{aligned} \tag{3.19}$$

Notice that the cross-term in this last equation (*i.e.*, the second term) is non-zero, in general. Furthermore, there is no prospect of making it zero, as was the case when introducing the time-windowed mean subtraction. Thus, the original kICS technique is affected by oscillations caused by the individual immobile particle positions. We demonstrate this effect in Fig. 3.6.

In part (a) of the figure below, oscillations are caused by the immobile particle positions and the presence of photobleaching. Part (b) further demonstrates that it is, in general, insufficient to define the intensity fluctuations by simply subtracting the time average, as photobleaching will still affect the ACF, in this case. Finally, part (c) shows that using an appropriate choice of time-windowed intensity fluctuations can significantly lessen the oscillatory effect.

Note we are not claiming that the extended kICS technique developed in the main text is superior to the original one. The original method allowed one to separate transport kinetics from photophysical processes in systems without an immobile blinking population of fluorophores. In this work, we extended the analysis to systems with these populations

and aimed to measure diffusion coefficients, as well as photophysical rates and diffusing particle fractions.

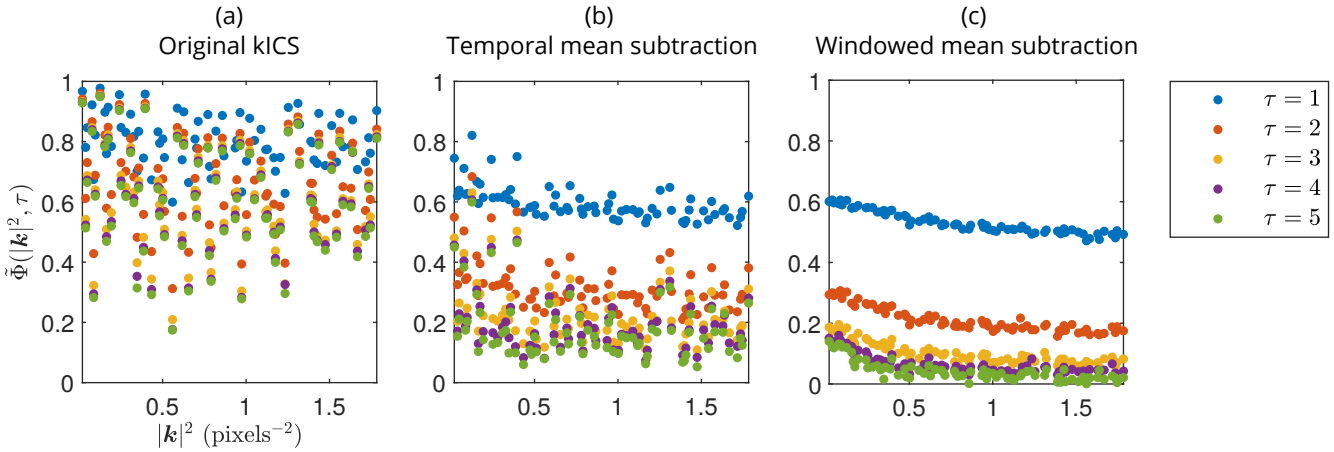

FIGURE 3.6: Comparison of ACF (a) without temporal mean subtraction (original kICS method), (b) with temporal mean subtraction, and (c) with time-windowed mean subtraction. Time-window used in (c) is $T_{\mathrm{w}} = 200$ frames. Simulation parameters: $D = 1$ pixels^2·frame^{-1}, $K = 1$ frame^{-1}, $\rho_{\mathrm{on}} = 0.3$, $p_D = 0.35$ and $k_{\mathrm{p}} = 5 \times 10^{-4}$ frame^{-1}.

Autocorrelation function derivation

Diffusing and immobile populations (2D)

Here we explicitly provide the ACF for a combination of immobile and diffusing particles. We assume the fluorophores are undergoing a simple two-state, on-off photoblinking process, in the absence of photobleaching. However, we will use the expression derived here to fit for ACFs computed from systems with photobleaching. This can be a good approximation for such systems when using the time-windowed subtraction in Eq. (3.13) to compute the fluctuations, as discussed in the main text. In the later subsection titled "Time-windowed correction", we present a derivation that explicitly accounts for photobleaching. The fit function for the expression supplied here will also be included in the provided GitHub repository as Matlab code.

Accounting for the effect of detector time-integration in Eq. (3.4), the autocorrelation in Eq. (3.7) is re-expressed as:

$$\tilde{\phi}(\boldsymbol{k},\tau) \equiv \begin{cases} \int_{\tau}^{\tau+1} \mathrm{d}t_2 \int_0^1 \mathrm{d}t_1 \langle \delta_t \tilde{i}(\boldsymbol{k},t_1) \delta_t \tilde{i}^*(\boldsymbol{k},t_2) \rangle_t & \tau \neq 0 \\ 2 \times \int_0^1 \mathrm{d}t_2 \int_0^{t_2} \mathrm{d}t_1 \langle \delta_t \tilde{i}(\boldsymbol{k},t_1) \delta_t \tilde{i}^*(\boldsymbol{k},t_2) \rangle_t & \tau = 0 \end{cases}. \tag{3.20}$$

Using the mobile component from Eq. (3.12), the autocorrelation for a diffusing particle is then (see Sehayek *et al.*[30] for photophysical autocorrelation details; also see Kolin *et al.*,[19] as well as Berne and Pecora[39] for the Fourier autocorrelation of diffusing particles),

$$\tilde{\phi}_{\text{diff}}(Q,\tau) \equiv \rho_{\text{on}} \begin{cases} e^{-Q(\tau-1)}\left(\frac{\left(1-e^{-Q}\right)^2\rho_{\text{on}}}{Q^2}+\frac{(1-\rho_{\text{on}})\left(1-e^{-(Q+K)}\right)^2 e^{-K(\tau-1)}}{(Q+K)^2}\right) & \tau\neq 0 \\ 2\frac{1}{Q(Q+K)}\times & \\ \quad\left(Q-\frac{Q(1-\rho_{\text{on}})\left(1-e^{-(Q+K)}\right)}{Q+K}+\frac{\left(Q+e^{-Q}-1\right)K\rho_{\text{on}}}{Q}-\left(1-e^{-Q}\right)\rho_{\text{on}}\right) & \tau=0 \end{cases}, \tag{3.21}$$

where we define,

$$Q \equiv D|\boldsymbol{k}|^2. \tag{3.22}$$

Note that in Eq. (3.21), we have left out dependence on the PSF and q, as they are ultimately divided out by the normalization in Eq. (3.14).

Likewise, we obtain the autocorrelation for an immobile particle by explicitly expressing the immobile component in Eq. (3.12),[30]

$$\tilde{\phi}_{\text{imm}}(\tau) \equiv \frac{1}{K^2}\rho_{\text{on}}(1-\rho_{\text{on}}) \times \begin{cases} \left(1-e^{-K}\right)^2 e^{-K(\tau-1)} & \tau\neq 0 \\ 2\times\left(e^{-K}+K-1\right) & \tau=0 \end{cases}, \tag{3.23}$$

where we again omit PSF and q dependence.

It follows that the ACF, defined in Eq. (3.14) (including camera time-integration), for a mixture of diffusing and immobile particles is:

$$\tilde{\phi}(Q,\tau) = \frac{p_D\tilde{\phi}_{\text{diff}}(Q,\tau)+(1-p_D)\tilde{\phi}_{\text{imm}}(\tau)}{p_D\tilde{\phi}_{\text{diff}}(Q,0)+(1-p_D)\tilde{\phi}_{\text{imm}}(0)}. \tag{3.24}$$

Diffusing and immobile populations (3D)

Here we discuss the analysis of 3D systems. We again consider the combination of immobile and diffusing populations. A full expression for the 3D ACF will be included in the provided GitHub repository as Matlab code. In the work of Kolin *et al.*,[19] it was shown that for an LSM, the 3D contribution to the kICS autocorrelation appears as a multiplying factor to its 2D counterpart. Namely, for a diffusing population, the factor is:

$$\frac{z_0^2}{4\sqrt{\pi}\sqrt{4D\tau+z_0^2}}, \tag{3.25}$$

where z_0 is the e^{-2} PSF radius in the axial direction.

Considering detector time-integration in the autocorrelation, as in Eq. (3.20), the autocorrelation of a blinking, diffusing particle in 3D then has the form (in the absence of bleaching):

$$\tilde{\phi}_{\text{diff,3D}}(A,\tau) \propto \int_{\tau}^{\tau+1} \mathrm{d}t_2 \int_{0}^{1} \mathrm{d}t_1 \frac{1}{\sqrt{4D(t_2-t_1)+z_0^2}} e^{-A(t_2-t_1)} \qquad (\tau \neq 0). \tag{3.26}$$

This integral can be done by substituting:

$$u = \sqrt{4D(t_2-t_1)+z_0^2}. \tag{3.27}$$

Eq. (3.26) is then reduced to:

$$\tilde{\phi}_{\text{diff,3D}}(B,\tau) \propto \frac{1}{2} e^{Bz_0^2} \int_{\tau}^{\tau+1} \mathrm{d}t_2 \int_{\sqrt{4D(t_2-1)+z_0^2}}^{\sqrt{4Dt_2+z_0^2}} \mathrm{d}u\, e^{-Bu^2} \qquad (\tau \neq 0), \tag{3.28}$$

with

$$B \equiv A/4D. \tag{3.29}$$

A similar calculation can be performed when $\tau = 0$.

For immobile populations, the 3D multiplying factor is simply $1/z_0$, as can be seen by setting $D = 0$ in Eq. (3.25).

Time-windowed correction

Here we derive the theoretical expression for the ACF while considering the effect of the time-windowed mean subtraction. A full expression will be made available in the provided GitHub code repository. For generality, we assume the processes considered are non-stationary in time (as is the case with photobleaching, for example). Given the complexity of this expression, it is best used when the photobleaching is prominent and when Eq. (3.24) cannot produce a reasonable fit to the data.

We begin by averaging the autocorrelation in Eq. (3.7) of the main text over all frame pairs for lag τ while using the definition of the local temporal fluctuation in Eq. (3.13)

to obtain:

$$\tilde{\phi}(\boldsymbol{k},\tau) = \frac{1}{T-\tau}\sum_{t=0}^{T-\tau-1}\Bigg\{\tilde{g}_i(\boldsymbol{k};t,t+\tau) - \frac{1}{T_\mathrm{w}}\sum_{s=t}^{t+T_\mathrm{w}-1}\Bigg[\tilde{g}_i(\boldsymbol{k};t,s+\tau)+\tilde{g}_i(\boldsymbol{k};s,t+\tau) - \frac{1}{T_\mathrm{w}}\sum_{s'=t}^{t+T_\mathrm{w}-1}\tilde{g}_i(\boldsymbol{k};s,s'+\tau)\Bigg]\Bigg\}, \tag{3.30}$$

where we have defined (accounting for detector time-integration in Eq. (3.4)):

$$\tilde{g}_i(\boldsymbol{k};u,v) \equiv \begin{cases} \int_v^{v+1}\mathrm{d}v'\int_u^{u+1}\mathrm{d}u'\left\langle\tilde{i}(\boldsymbol{k},u')\tilde{i}^*(\boldsymbol{k},v')\right\rangle_t & u\neq v \\ 2\times\int_u^{u+1}\mathrm{d}v'\int_u^{v'}\mathrm{d}u'\left\langle\tilde{i}(\boldsymbol{k},u')\tilde{i}^*(\boldsymbol{k},v')\right\rangle_t & u=v \end{cases}. \tag{3.31}$$

The simplest way to carry out the sums in Eq. (3.30) is to rewrite them using time-lags (see Fig. 3.7). We can then rewrite the first term in the square brackets of Eq. (3.30) as:

$$\sum_{t=0}^{T-\tau-1}\sum_{s=t}^{t+T_\mathrm{w}-1}\tilde{g}_i(\boldsymbol{k};t,s+\tau) = \sum_{t=0}^{T-\tau-1}\sum_{\nu=0}^{T_w-1}\tilde{\phi}_i(\boldsymbol{k},\tau+\nu;t), \tag{3.32}$$

where we define:

$$\tilde{\phi}_i(\boldsymbol{k},\tau;t) \equiv \tilde{g}_i(\boldsymbol{k};t,t+\tau). \tag{3.33}$$

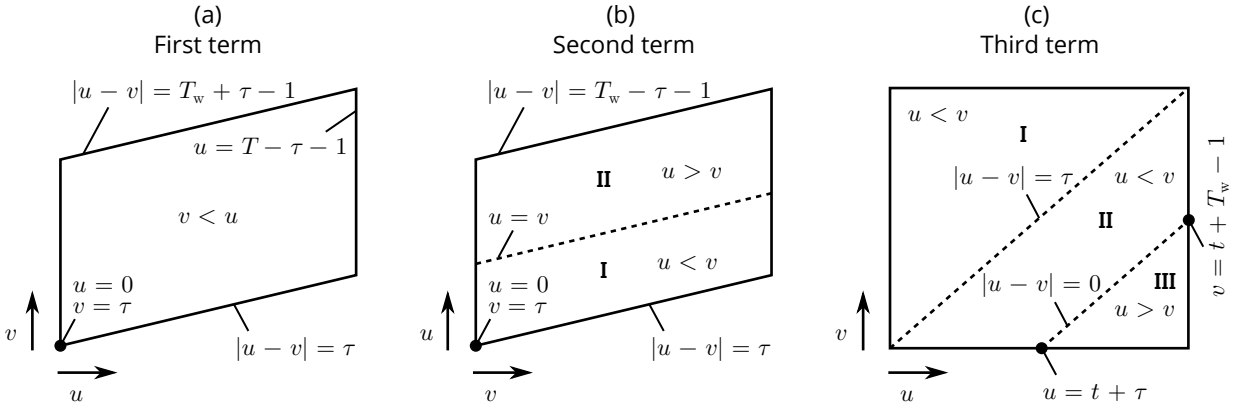

FIGURE 3.7: Illustration of sums in square brackets of Eq. (3.30). Diagonal lines within regions represent fixed time-lags, *i.e.*, constant $|u-v|$ in Eq. (3.31). Sums are, therefore, simpler when carried out over and along diagonals. Time ordering of u and v is also shown within different subregions. Depiction of third term in (c) only shows the two innermost sums from Eq. (3.30).

Using this last definition, the time-index, t, must follow $t \equiv \min(u, v)$, such that,

$$\tilde{g}_i(\boldsymbol{k}; u, v) \to \tilde{\phi}_i\left(\boldsymbol{k}, \tau \equiv |u - v|; t \equiv \min(u, v)\right). \tag{3.34}$$

We continue to rewrite the second term (according to the subregions depicted in Fig. 3.7),

$$\sum_{t=0}^{T-\tau-1} \sum_{s=t}^{t+T_\mathrm{w}-1} \tilde{g}_i(\boldsymbol{k}; s, t+\tau) = \underbrace{\sum_{\nu=0}^{\tau} \sum_{t=\tau-\nu}^{T-\nu-1} \tilde{\phi}_i(\boldsymbol{k}, \nu; t)}_{\mathrm{I}} + \underbrace{\sum_{\nu=1}^{T_\mathrm{w}-\tau-1} \sum_{t=\tau}^{T-1} \tilde{\phi}_i(\boldsymbol{k}, \nu; t)}_{\mathrm{II}}. \tag{3.35}$$

Finally, the third term in the square brackets of Eq. (3.30) can be re-expressed as:

$$\begin{aligned}
&\sum_{t=0}^{T-\tau-1} \sum_{s=t}^{t+T_\mathrm{w}-1} \sum_{s'=t}^{t+T_\mathrm{w}-1} \tilde{g}_i(\boldsymbol{k}; s, s'+\tau) = \\
&\quad \sum_{t=0}^{T-\tau-1} \Bigg(\underbrace{\sum_{\nu=0}^{T_\mathrm{w}-1} \sum_{t'=t}^{t+T_\mathrm{w}-\nu-1} \tilde{\phi}_i(\boldsymbol{k}, \tau+\nu; t')}_{\mathrm{I}} + \underbrace{\sum_{\nu=1}^{\tau} \sum_{t'=t+\nu}^{t+T_\mathrm{w}-1} \tilde{\phi}_i(\boldsymbol{k}, \tau-\nu; t')}_{\mathrm{II}} \\
&\qquad + \underbrace{\sum_{\nu=\tau+1}^{T_\mathrm{w}-1} \sum_{t'=t}^{t+T_\mathrm{w}-\nu-1} \tilde{\phi}_i(\boldsymbol{k}, \nu-\tau; t'+\tau)}_{\mathrm{III}} \Bigg).
\end{aligned} \tag{3.36}$$

Notice the number of terms in different diagonals is not constant for the third term, as was the case with the other terms.

For a mixture of immobile and diffusing populations with the same photophysical properties,[19, 30, 39]

$$\left\langle \tilde{i}(\boldsymbol{k}, u) \tilde{i}^*(\boldsymbol{k}, v) \right\rangle_t \equiv e^{-k_\mathrm{p} \max(u,v)} \rho_\mathrm{on} \left(\rho_\mathrm{on} + (1-\rho_\mathrm{on}) e^{-K|u-v|}\right) \left(N_\mathrm{imm} + N_\mathrm{diff} e^{-|\boldsymbol{k}|^2 D|u-v|}\right), \tag{3.37}$$

where k_p is the photobleaching rate, assumed to be equal from both on- and off-states. Note the last equation assumes the cross-terms due to non-identical particles in Eq. (3.12) are effectively zero for reasonable choice of T_w. We also omit the PSF and q from this equation as they cancel out when using the normalization in Eq. (3.14).

The time-window correction to the ACF must be used when the diffusion is relatively slow, as was demonstrated in Figure 3.2 (C). Using the time-window correction can also allow for choosing smaller windows, which is necessary when the photobleaching is more

prominent. See the main text for more details.

We compare fits with and without the time-window correction in Fig. 3.8 and Table 3.4 below. Photobleaching was not accounted for in either fit model. As we expect, the fits are more accurate when using the time-window correction. Furthermore, from this figure, one can see the effect of choosing a small time-window on the ACF at small $|\boldsymbol{k}|^2$.

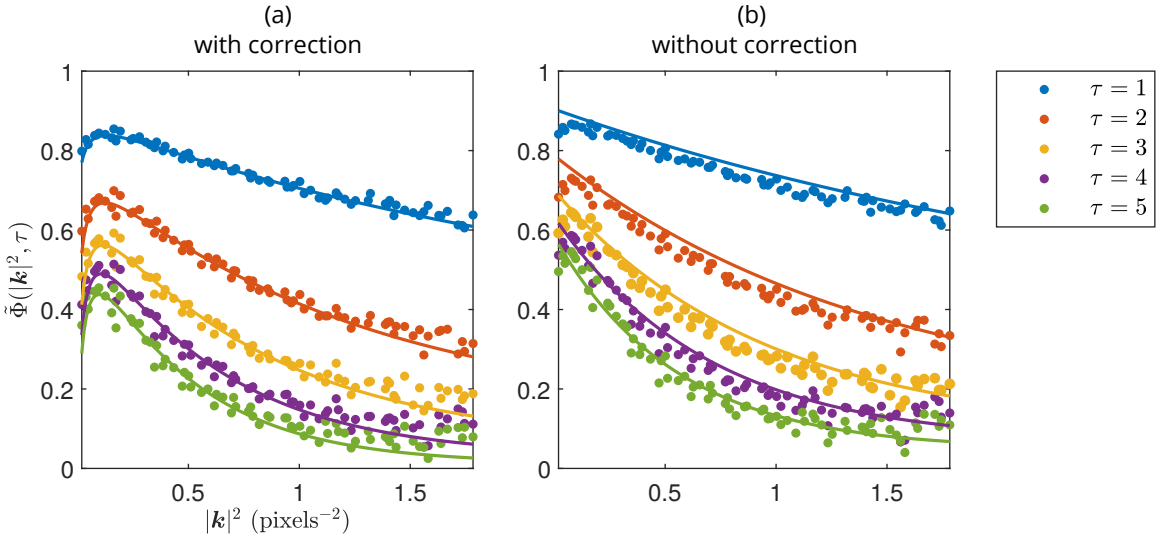

FIGURE 3.8: Comparison of fits (a) with and (b) without time-window correction. The "bump" seen at early $|\boldsymbol{k}|^2$ is caused by the correlation of the time-window. Time windows used were (a) 50 frames and (b) 100 frames. Fit was done over first 25 time-lags, in both cases; only first 5 are shown. Photobleaching rate was set to $k_\mathrm{p} = 5 \times 10^{-4}$ frame^{-1}.

	With correction	Without correction	Simulation
D (pixels^2·frame^{-1})	0.447 ± 0.007	0.39 ± 0.02	0.5
K (frame^{-1})	0.60 ± 0.02	0.474 ± 0.003	0.6
ρ_on	0.84 ± 0.02	0.29 ± 0.03	0.833
f_D	0.27 ± 0.03	0.73 ± 0.03	0.3

TABLE 3.4: Comparison of fitted and simulated parameters for fits shown in Figure 3.8.

Simulation was generated with $T = 2048$ frames on a 128×128 pixel grid with 4813 total particles. Fitted parameters and errors were obtained by splitting the simulation spatially into 4 equally sized and independent ROIs, and then calculating the mean and its standard error from their analyses.

Simulation details

This section provides the default parameters used in our simulations (see Table 3.5). More details about the noise model and how we assign synthetic intensity values to the pixels in our simulations can be found in Sehayek *et al.* (2019).[30]

Parameter description	Value
Analogue to digital conversion factor	12
Autofluorescent photon rate	5% of mean simulated image series intensity
Average photon rate per molecule	$5,000$ frame^{-1}
Clock induced charge	5×10^{-3} frame^{-1} pixel^{-1}
Dark noise photon rate	8×10^{-4} frame^{-1} pixel^{-1}
Detector quantum efficiency	0.9
EM Gain	200
Exposure time (τ_i)	0.05 s frame^{-1}
Image dimensions	128×128 pixels^2
Laser e^{-2} radius	$2 \times \sqrt{\text{number of pixels}}$
PSF e^{-2} radius	3 pixels
Probability of aggregation	0.3
Mean number of monomers *per* aggregate	2
Number of filaments (where applicable)	20
Standard deviation of distance between aggregate center and monomers	0.3 pixels

TABLE 3.5: Default simulation parameters.
These parameters were used in our simulations, unless otherwise stated. Some synthetic noise parameter values are negligible, but are included for the purpose of completeness.

Noise autocorrelation

Here we derive an expression for the autocorrelation of the Fourier transform of the noise. Assuming $\langle \epsilon(\boldsymbol{r}, t) \rangle_t \equiv \mu_\epsilon$, it follows that:

$$\langle \tilde{\epsilon}(\boldsymbol{k}, t) \rangle_t = \int_{\text{ROI}} \mathrm{d}\boldsymbol{r} \underbrace{\langle \epsilon(\boldsymbol{r}, t) \rangle_t}_{\mu_\epsilon} e^{-i\boldsymbol{k}\cdot\boldsymbol{r}} \overset{A_{\text{ROI}} \to \infty}{\propto} \delta(\boldsymbol{k}). \tag{3.38}$$

In this last equation, A_{ROI} denotes the area of the chosen ROI. Therefore, we have:

$$\langle \delta_t \tilde{\epsilon}(\boldsymbol{k}, t) \delta_t \tilde{\epsilon}^*(\boldsymbol{k}, t+\tau) \rangle_t = \langle \epsilon(\boldsymbol{k}, t) \tilde{\epsilon}^*(\boldsymbol{k}, t+\tau) \rangle_t, \text{ for } |\boldsymbol{k}| \neq 0. \tag{3.39}$$

Furthermore, by definition of white-noise:

$$\langle \tilde{\epsilon}(\boldsymbol{r}', t) \tilde{\epsilon}^*(\boldsymbol{r}'', t+\tau) \rangle_t \equiv \sigma_\epsilon^2 \delta_{\tau,0} \delta(|\boldsymbol{r}'' - \boldsymbol{r}'|), \tag{3.40}$$

where σ_ϵ^2 is the variance of the white-noise. Using Eqs. (3.39) and (3.40), we obtain:

$$\begin{aligned}\langle \epsilon(\boldsymbol{k},t)\tilde{\epsilon}^*(\boldsymbol{k},t+\tau)\rangle_t &= \int_{\mathrm{ROI}} \mathrm{d}\boldsymbol{r}' \int_{\mathrm{ROI}} \mathrm{d}\boldsymbol{r}'' \langle \tilde{\epsilon}(\boldsymbol{r}',t)\tilde{\epsilon}^*(\boldsymbol{r}'',t+\tau)\rangle_t e^{-i\boldsymbol{k}\cdot(\boldsymbol{r}''-\boldsymbol{r}')} \\ &= \sigma^2\delta_{\tau,0} \int_{\mathrm{ROI}} \mathrm{d}\boldsymbol{r}' \int_{\mathrm{ROI}} \mathrm{d}\boldsymbol{r}'' \delta(|\boldsymbol{r}''-\boldsymbol{r}'|) e^{-i\boldsymbol{k}\cdot(\boldsymbol{r}''-\boldsymbol{r}')} \\ &= A_{\mathrm{ROI}}\sigma^2\delta_{\tau,0}. \end{aligned} \tag{3.41}$$

References for Chapter 3

[1] B. Huang, H. Babcock, and X. Zhuang. Breaking the Diffraction Barrier: Super-Resolution Imaging of Cells. *Cell* **143**,7 (2010), pp. 1047–1058.

[2] E. Sezgin. Super-resolution optical microscopy for studying membrane structure and dynamics. *J. Condens. Matter Phys.* **29**,27 (2017), p. 273001.

[3] M. B. Stone, S. A. Shelby, and S. L. Veatch. Super-Resolution Microscopy: Shedding Light on the Cellular Plasma Membrane. *Chem. Rev.* **117**,11 (2017), pp. 7457–7477.

[4] B. O. Leung and K. C. Chou. Review of Super-Resolution Fluorescence Microscopy for Biology. *Appl. Spectrosc.* **65**,9 (2011), pp. 967–980.

[5] A. Gahlmann and W. E. Moerner. Exploring bacterial cell biology with single-molecule tracking and super-resolution imaging. *Nat. Rev. Microbiol.* **12**,1 (2014), pp. 9–22.

[6] M. J. Rust, M. Bates, and X. Zhuang. Sub-diffraction-limit imaging by stochastic optical reconstruction microscopy (STORM). *Nat. Methods* **3**,10 (2006), pp. 793–796.

[7] E. Betzig et al. Imaging Intracellular Fluorescent Proteins at Nanometer Resolution. *Science* **313**,5793 (2006), pp. 1642–1645.

[8] T. Dertinger et al. Fast, background-free, 3D super-resolution optical fluctuation imaging (SOFI). *Proc. Natl. Acad. Sci. U.S.A.* **106**,52 (2009), pp. 22287–22292.

[9] C. Eggeling et al. Direct observation of the nanoscale dynamics of membrane lipids in a living cell. *Nature* **457**,7233 (2009), pp. 1159–1162.

[10] A. Honigmann et al. Scanning STED-FCS reveals spatiotemporal heterogeneity of lipid interaction in the plasma membrane of living cells. *Nat. Commun.* **5**,1 (2014), pp. 1–12.

[11] P. N. Hedde et al. Stimulated emission depletion-based raster image correlation spectroscopy reveals biomolecular dynamics in live cells. *Nat. Commun.* **4**,1 (2013), pp. 1–8.

[12] S. Manley et al. High-density mapping of single-molecule trajectories with photoactivated localization microscopy. *Nat. Methods* **5**,2 (2008), pp. 155–157.

[13] F. Balzarotti et al. Nanometer resolution imaging and tracking of fluorescent molecules with minimal photon fluxes. *Science* **355**,6325 (2017), pp. 606–612.

[14] L. Kisley et al. Characterization of Porous Materials by Fluorescence Correlation Spectroscopy Super-resolution Optical Fluctuation Imaging. *ACS Nano* **9**,9 (2015), pp. 9158–9166.

[15] D. Magde, E. Elson, and W. W. Webb. Thermodynamic Fluctuations in a Reacting System—Measurement by Fluorescence Correlation Spectroscopy. *Phys. Rev. Lett.* **29**, (11 Sept. 1972), pp. 705–708.

[16] E. L. Elson and D. Magde. Fluorescence correlation spectroscopy. I. Conceptual basis and theory. *Biopolymers* **13**,1 (1974), pp. 1–27.

[17] D. Magde, E. L. Elson, and W. W. Webb. Fluorescence correlation spectroscopy. II. An experimental realization. *Biopolymers* **13**,1 (1974), pp. 29–61.

[18] J. W. Krieger et al. Imaging fluorescence (cross-) correlation spectroscopy in live cells and organisms. *Nature Protoc.* **10**,12 (2015), pp. 1948–1974.

[19] D. L. Kolin, D. Ronis, and P. W. Wiseman. k-Space Image Correlation Spectroscopy: A Method for Accurate Transport Measurements Independent of Fluorophore Photophysics. *Biophys. J.* **91**,8 (2006), pp. 3061–3075.

[20] D. L. Kolin and P. W. Wiseman. Advances in image correlation spectroscopy: measuring number densities, aggregation states, and dynamics of fluorescently labeled macromolecules in cells. *Cell Biochem. Biophys.* **49**,3 (2007), pp. 141–164.

[21] B. Hebert, S. Costantino, and P. W. Wiseman. Spatiotemporal image correlation spectroscopy (STICS) theory, verification, and application to protein velocity mapping in living CHO cells. *Biophys. J.* **88**,5 (2005), pp. 3601–3614.

[22] M. A. Digman et al. Measuring Fast Dynamics in Solutions and Cells with a Laser Scanning Microscope. *Biophys. J.* **89**,2 (2005), pp. 1317–1327.

[23] R. Hoebe et al. Controlled light-exposure microscopy reduces photobleaching and phototoxicity in fluorescence live-cell imaging. *Nat. Biotechnol.* **25**,2 (2007), pp. 249–253.

[24] G. Donnert, C. Eggeling, and S. W. Hell. Major signal increase in fluorescence microscopy through dark-state relaxation. *Nat. Methods* **4**,1 (2007), pp. 81–86.

[25] P. P. Mondal, R. J. Gilbert, and P. T. C. So. Photobleaching reduced fluorescence correlation spectroscopy. *Appl. Phys. Lett.* **97**,10 (2010), p. 103704.

[26] L. Song et al. Photobleaching kinetics of fluorescein in quantitative fluorescence microscopy. *Biophys. J.* **68**,6 (1995), pp. 2588–2600.

[27] J. Widengren and R. Rigler. Mechanisms of photobleaching investigated by fluorescence correlation spectroscopy. *Bioimaging* **4**,3 (1996), pp. 149–157.

[28] D. L. Kolin, S. Costantino, and P. W. Wiseman. Sampling effects, noise, and photobleaching in temporal image correlation spectroscopy. *Biophys. J.* **90**,2 (2006), pp. 628–639.

[29] M. A. Digman et al. Mapping the Number of Molecules and Brightness in the Laser Scanning Microscope. *Biophys. J.* **94**,6 (2008), pp. 2320–2332.

[30] S. Sehayek et al. A High-Throughput Image Correlation Method for Rapid Analysis of Fluorophore Photoblinking and Photobleaching Rates. *ACS Nano* **13**,10 (2019), pp. 11955–11966.

[31] M. Wachsmuth, W. Waldeck, and J. Langowski. Anomalous diffusion of fluorescent probes inside living cell nuclei investigated by spatially-resolved fluorescence correlation spectroscopy. *J. Mol. Biol.* **298**,4 (2000), pp. 677–689.

[32] P. Sengupta et al. Measuring Size Distribution in Highly Heterogeneous Systems with Fluorescence Correlation Spectroscopy. *Biophys. J.* **84**,3 (2003), pp. 1977–1984.

[33] M. Weiss, H. Hashimoto, and T. Nilsson. Anomalous Protein Diffusion in Living Cells as Seen by Fluorescence Correlation Spectroscopy. *Biophys. J.* **84**,6 (2003), pp. 4043–4052.

[34] M. Weiss et al. Anomalous Subdiffusion Is a Measure for Cytoplasmic Crowding in Living Cells. *Biophys. J.* **87**,5 (2004), pp. 3518–3524.

[35] D. S. Banks and C. Fradin. Anomalous Diffusion of Proteins Due to Molecular Crowding. *Biophys. J.* **89**,5 (2005), pp. 2960–2971.

[36] K. Tsekouras et al. Inferring diffusion dynamics from FCS in heterogeneous nuclear environments. *Biophys. J.* **109**,1 (2015), pp. 7–17.

[37] C. M. Brown et al. Raster image correlation spectroscopy (RICS) for measuring fast protein dynamics and concentrations with a commercial laser scanning confocal microscope. *J. Microsc.* **229**,1 (2008), pp. 78–91.

[38] H. B. Brandão et al. Measuring ligand–receptor binding kinetics and dynamics using k-space image correlation spectroscopy. *Methods* **66**,2 (2014), pp. 273–282.

[39] B. Berne and R. Pecora. Dynamic Light Scattering: With Applications to Chemistry, Biology, and Physics. In: Dover Books on Physics Series. Dover Publications, 2000. Chap. 5.4.

[40] A. P. Singh et al. The performance of 2D array detectors for light sheet based fluorescence correlation spectroscopy. *Opt. Express* **21**,7 (Apr. 2013), pp. 8652–8668.

[41] R. A. Colyer et al. High-throughput FCS using an LCOS spatial light modulator and an 8 × 1 SPAD array. *Biomed. Opt. Express* **1**,5 (Dec. 2010), pp. 1408–1431.

[42] B. Mandracchia et al. Fast and accurate sCMOS noise correction for fluorescence microscopy. *Nat. Commun.* **11**,1 (2020), pp. 1–12.

[43] W.-T. Yip et al. Classifying the Photophysical Dynamics of Single- and Multiple-Chromophoric Molecules by Single Molecule Spectroscopy. *J. Phys. Chem. A* **102**,39 (1998), pp. 7564–7575.

[44] E. K. L. Yeow et al. Characterizing the Fluorescence Intermittency and Photobleaching Kinetics of Dye Molecules Immobilized on a Glass Surface. *J. Phys. Chem. A* **110**,5 (2006), pp. 1726–1734.

[45] J. Widengren, U. Mets, and R. Rigler. Fluorescence correlation spectroscopy of triplet states in solution: a theoretical and experimental study. *J. Phys. Chem.* **99**,36 (1995), pp. 13368–13379.

[46] S. Geissbuehler et al. Mapping molecular statistics with balanced super-resolution optical fluctuation imaging (bSOFI). *Opt. Nanoscopy* **1**,1 (2012), pp. 1–7.

[47] X. Yi. Super resolution of Optical Fluctuation Imaging 2.0 (SOFI-2.0): Towards fast super resolved imaging of live cells. PhD thesis. UCLA, 2017.

[48] X. Yi et al. Moments reconstruction and local dynamic range compression of high order superresolution optical fluctuation imaging. *Biomed. Opt. Express* **10**,5 (May 2019), pp. 2430–2445.

[49] J. McGrath et al. Simultaneous Measurements of Actin Filament Turnover, Filament Fraction, and Monomer Diffusion in Endothelial Cells. *Biophys. J.* **75**,4 (1998), pp. 2070–2078.

[50] D. Zicha et al. Rapid Actin Transport During Cell Protrusion. *Science* **300**,5616 (2003), pp. 142–145.

[51] D. McDonald et al. Nucleoplasmic β-actin exists in a dynamic equilibrium between low-mobility polymeric species and rapidly diffusing populations. *J. Cell. Biol.* **172**,4 (2006), pp. 541–552.

[52] T. Kiuchi et al. Measurements of spatiotemporal changes in G-actin concentration reveal its effect on stimulus-induced actin assembly and lamellipodium extension. *J. Cell Biol.* **193**,2 (2011), pp. 365–380.

[53] I. L. Novak, B. M. Slepchenko, and A. Mogilner. Quantitative analysis of G-actin transport in motile cells. *Biophys. J.* **95**,4 (2008), pp. 1627–1638.

[54] A. Gasilina et al. The ArfGAP ASAP1 Controls Actin Stress Fiber Organization via Its N-BAR Domain. *iScience* **22**, (2019), pp. 166–180.

[55] S. Bretschneider, C. Eggeling, and S. W. Hell. Breaking the Diffraction Barrier in Fluorescence Microscopy by Optical Shelving. *Phys. Rev. Lett.* **98**, (21 May 2007), p. 218103.

[56] S. Habuchi et al. Reversible single-molecule photoswitching in the GFP-like fluorescent protein Dronpa. *Proc. Natl. Acad. Sci. U.S.A.* **102**,27 (2005), pp. 9511–9516.

[57] I. Blikstad and L. Carlsson. On the dynamics of the microfilament system in HeLa cells. *J. Cell Biol.* **93**,1 (Apr. 1982), pp. 122–128.

[58] M. Hirsch et al. A Stochastic Model for Electron Multiplication Charge-Coupled Devices – From Theory to Practice. *PLOS ONE* **8**,1 (Jan. 2013), pp. 1–13.

Chapter 4

Conclusion

In this work, we showed that image correlation methods can be used to rapidly, simultaneously and accurately measure multiple dynamic or kinetic parameters from noisy fluorescence image series.

In Chapter 2, we developed an image correlation method for rapidly measuring the photophysical rates of immobile fluorophores. We demonstrated that this technique can measure photoblinking rates that are faster than the camera detector sampling rate, while the traditionally used single-molecule thresholding methods cannot. Furthermore, the latter methods take at least hours to implement and cannot be used at high particle densities, while our method can perform the same analysis in seconds and can be used at very high densities. Our method's capability to rapidly measure fluorophore photoblinking rates can be useful for quickly screening fluorescent probes for application in STORM or SOFI. An extension of the method could possibly be used to map different cellular environments if the probe fluorophores have different photophysical rates in different compartments. Some drawbacks of this method are its requirement for the fluorophores to be uniformly distributed in the analyzed ROI and the large number of blinking events needed to correctly measure photoblinking rates relevant to STORM. Perhaps the former issue could be corrected by recomputing the ACF assuming a specific non-uniform distribution of particles, *e.g.*, uniformly distributed aggregates in space, with monomers uniformly distributed among the aggregates.

In Chapter 3, we presented a method for analyzing systems with both mobile and immobile populations subject to photophysical processes. We showed the technique can be rapidly utilized to measure the diffusion rate, photoblinking rates and fraction of diffusing particles. Unlike other image correlation methods, we also showed that the technique could analyze ROIs with non-uniformly distributed immobile fluorophores in space that are subject to blinking and bleaching. This is especially useful for studying systems relevant to STORM and SOFI. Moreover, our method can in principle be used in tandem with these super-resolution techniques to recover both static and dynamic

information from a system. On the other hand, while we were able to select larger ROIs to increase spatial sampling in our analysis, our technique also required these larger ROIs to avoid aliasing in the ACF, so that it is probably not suited for generating spatial maps of the fitted parameters. A more fine-tuned approach would be to use an SPT technique, such as sptPALM.[82]

While image correlation methods can measure parameters of interest rapidly and accurately, they only offer single point estimates of these parameters. Therefore, obtaining the errors on parameters measured with correlation methods is not always straightforward. Conversely, single-molecule approaches typically extract parameter distributions, but cannot be utilized at high densities and are difficult to implement in certain systems (*e.g.* with both blinking and transport). Furthermore, correlation methods need to assume a given theoretical model and it is not trivial to compare accuracy with other models. To overcome the model selection problem, some recently developed methods use non-parametric Bayesian inference (*e.g.* see [83, 84]) to determine posterior parameter distributions by analyzing photon counts within a confocal volume (most parameters are still determined with the standard Bayesian inference approach, though); however, these methods have significantly slower analysis times and have yet to be applied to real biological systems.

The techniques presented in the main chapters of this work were defined with alternative ACF normalizations to the traditional FCS and ICS normalization, which is used to determine particle density information. On the other hand, the normalizations that we employed were used to yield ACF definitions that were independent of any microscope parameters (under certain assumptions), and only dependent on photophysical and transport dynamics. Furthermore, we defined the fluorescence intensity fluctuations in the ACF of both these techniques through subtractions of local spatial/temporal averages. This allowed us to accurately extract information from systems that are not ergodic in space or time. Therefore, examining alternative ICS ACF definitions in the future can be beneficial depending on which parameters one would like to measure. In other words, in certain cases it may be beneficial to deviate from the traditional mean square intensity normalization and global mean subtracted intensity fluctuations that underpin most applications of FCS and ICS.

It would also be interesting to study the dynamic range of the extended kICS technique presented in Chapter 3 to see the limits of diffusion and photoblinking rates that can be accurately measured, similar to what was done in Chapter 2. Since we accounted for the effect of the camera detector time-integration in the extended kICS method (as was also done for the method developed in Chapter 2), we expect that it can measure faster

diffusion and photoblinking rates. It would also be of interest to compare this technique with sptPALM,[82] for example, which collects truncated diffusing particle trajectories that are intermittently in the fluorescent "on"-state.

Another potential application of our methods would be to utilize them to measure binding rates. Similar to STORM and PALM, binding kinetics can be used to form super-resolution images with a technique known as point accumulation for imaging in nanoscale topography (PAINT).[85] DNA-PAINT[86] is a popular variation of this technique that utilizes dye-labeled DNA oligomers that bind to complimentary strands bound to a target object. A recent implementation used peptide-protein interactions to employ PAINT in live cells.[87] When using imaging modalities like TIRFM, that illuminate only a thin section of the sample in the axial direction, the binding of the fluorophore complexes to the target object resembles blinking and the unbound molecules only appear as fluorescence background. Therefore, the rapid analysis capabilities of our techniques could be utilized to screen for optimal characteristic binding times for SMLM localization.

Finally, we propose to improve our method presented in Chapter 2 by estimating the bias of the ACF, similar to what was done in Chapter 3 to account for the finite time-windowed mean subtraction. This can be particularly useful for correcting the discrepancy in the measured blinking rates that we encountered for low sampling of the STORM data. Further statistical properties of the ACF, such as the variance, can also be computed to characterize its convergence at these low sampling limits. Note that these statistical properties, however, cannot be computed exactly due to the ACF normalization.

The methods we presented show promise for characterization of complex dynamic and kinetic parameters for blinking dyes imaged *in vitro* and in living cells. We anticipate our method in Chapter 2 will be useful for optimization of probe development pipelines for photoblinking fluorophores needed for SMLM. The method presented in Chapter 3 opens the door for rapidly studying the dynamics in complex cellular structures, encountered in SMLM, using image correlation.

References

[1] S. Sehayek et al. A High-Throughput Image Correlation Method for Rapid Analysis of Fluorophore Photoblinking and Photobleaching Rates. *ACS Nano* **13**,10 (2019), pp. 11955–11966.

[2] T. Novák et al. TestSTORM: Versatile simulator software for multimodal super-resolution localization fluorescence microscopy. *Sci. Rep.* **7**,1 (2017), pp. 1–8.

[3] S. Sehayek et al. Rapid ensemble measurement of protein diffusion and probe blinking dynamics in cells. *Biophys. Rep.* **1**,2 (2021), p. 100015.

[4] J. Requejo-Isidro. Fluorescence nanoscopy. Methods and applications. *J. Chem. Biol.* **6**,3 (2013), pp. 97–120.

[5] L. Schermelleh et al. Super-resolution microscopy demystified. *Nat. Cell Biol.* **21**,1 (2019), pp. 72–84.

[6] A. Gahlmann and W. E. Moerner. Exploring bacterial cell biology with single-molecule tracking and super-resolution imaging. *Nat. Rev. Microbiol.* **12**,1 (2014), pp. 9–22.

[7] B. Huang, H. Babcock, and X. Zhuang. Breaking the Diffraction Barrier: Super-Resolution Imaging of Cells. *Cell* **143**,7 (2010), pp. 1047–1058.

[8] B. O. Leung and K. C. Chou. Review of Super-Resolution Fluorescence Microscopy for Biology. *Appl. Spectrosc.* **65**,9 (2011), pp. 967–980.

[9] S. J. Sahl, S. W. Hell, and S. Jakobs. Fluorescence nanoscopy in cell biology. *Nat. Rev. Mol. Cell Biol.* **18**,11 (2017), pp. 685–701.

[10] E. Sezgin. Super-resolution optical microscopy for studying membrane structure and dynamics. *J. Condens. Matter Phys.* **29**,27 (2017), p. 273001.

[11] M. B. Stone, S. A. Shelby, and S. L. Veatch. Super-Resolution Microscopy: Shedding Light on the Cellular Plasma Membrane. *Chem. Rev.* **117**,11 (2017), pp. 7457–7477.

[12] D. Magde, E. Elson, and W. W. Webb. Thermodynamic Fluctuations in a Reacting System—Measurement by Fluorescence Correlation Spectroscopy. *Phys. Rev. Lett.* **29**, (11 Sept. 1972), pp. 705–708.

[13] E. L. Elson and D. Magde. Fluorescence correlation spectroscopy. I. Conceptual basis and theory. *Biopolymers* **13**,1 (1974), pp. 1–27.

[14] D. Magde, E. L. Elson, and W. W. Webb. Fluorescence correlation spectroscopy. II. An experimental realization. *Biopolymers* **13**,1 (1974), pp. 29–61.

[15] N. O. Petersen et al. Quantitation of membrane receptor distributions by image correlation spectroscopy: concept and application. *Biophys. J.* **65**,3 (1993), pp. 1135–1146.

[16] D. L. Kolin and P. W. Wiseman. Advances in image correlation spectroscopy: measuring number densities, aggregation states, and dynamics of fluorescently labeled macromolecules in cells. *Cell Biochem. Biophys.* **49**,3 (2007), pp. 141–164.

[17] C. Manzo and M. F. Garcia-Parajo. A review of progress in single particle tracking: from methods to biophysical insights. *Rep. Prog. Phys.* **78**,12 (2015), p. 124601.

[18] H. Shen et al. Single Particle Tracking: From Theory to Biophysical Applications. *Chem. Rev.* **117**,11 (2017), pp. 7331–7376.

[19] Introduction to Fluorescence. In: *Principles of Fluorescence Spectroscopy*. Ed. by J. R. Lakowicz. Boston, MA: Springer US, 2006, pp. 1–26.

[20] R. Y. Tsien, L. Ernst, and A. Waggoner. Fluorophores for Confocal Microscopy: Photophysics and Photochemistry. In: *Handbook Of Biological Confocal Microscopy*. Ed. by J. B. Pawley. Boston, MA: Springer US, 2006, pp. 338–352.

[21] P. Mondal and A. Diaspro. Basics of Fluorescence and Photophysics. In: *Fundamentals of Fluorescence Microscopy*. Springer, Dordrecht, 2014. Chap. 6, pp. 111–134.

[22] Q. Zheng, A. Pati, and S. Blanchard. Single Fluorophore Blinking. In: *Encyclopedia of Biophysics*. Ed. by G. Roberts and A. Watts. Springer Berlin Heidelberg, 2018.

[23] Q. Zheng, A. Pati, and S. Blanchard. Single Fluorophore Bleaching. In: *Encyclopedia of Biophysics*. Ed. by G. Roberts and A. Watts. Springer Berlin Heidelberg, 2018.

[24] Q. Zheng et al. Ultra-stable organic fluorophores for single-molecule research. *Chem. Soc. Rev.* **43**, (4 2014), pp. 1044–1056.

[25] C. Eggeling et al. Photobleaching of Fluorescent Dyes under Conditions Used for Single-Molecule Detection: Evidence of Two-Step Photolysis. *Anal. Chem.* **70**,13 (1998), pp. 2651–2659.

[26] C. Eggeling et al. Photostability of Fluorescent Dyes for Single-Molecule Spectroscopy: Mechanisms and Experimental Methods for Estimating Photobleaching in Aqueous Solution. In: *Applied Fluorescence in Chemistry, Biology and Medicine*. Berlin, Heidelberg: Springer Berlin Heidelberg, 1999, pp. 193–240.

[27] M. Y. Berezin and S. Achilefu. Fluorescence Lifetime Measurements and Biological Imaging. *Chem. Rev.* **110**,5 (2010), pp. 2641–2684.

[28] Time-Domain Lifetime Measurements. In: *Principles of Fluorescence Spectroscopy*. Ed. by J. R. Lakowicz. Boston, MA: Springer US, 2006, pp. 97–155.

[29] S. Inoué. Foundations of Confocal Scanned Imaging in Light Microscopy. In: *Handbook Of Biological Confocal Microscopy*. Ed. by J. B. Pawley. Boston, MA: Springer US, 2006, pp. 1–19.

[30] E. Sezgin et al. Measuring nanoscale diffusion dynamics in cellular membranes with super-resolution STED–FCS. *Nat. Protoc.* **14**,4 (2019), pp. 1054–1083.

[31] R. P. Nieuwenhuizen et al. Measuring image resolution in optical nanoscopy. *Nat. Methods* **10**,6 (2013), pp. 557–562.

[32] M. J. Sanderson et al. Fluorescence Microscopy. *Cold Spring Harb. Protoc.* **2014**,10 (2014).

[33] N. Naredi-Rainer et al. Confocal Microscopy. In: *Fluorescence Microscopy*. Ed. by U. Kubitscheck. John Wiley & Sons, Ltd, 2017. Chap. 5, pp. 165–202.

[34] J. Oreopoulos, R. Berman, and M. Browne. Chapter 9 - Spinning-disk confocal microscopy: present technology and future trends. In: *Quantitative Imaging in Cell Biology*. Ed. by J. C. Waters and T. Wittman. Vol. 123. Methods in Cell Biology. Academic Press, 2014, pp. 153–175.

[35] C. M. St. Croix, S. H. Shand, and S. C. Watkins. Confocal microscopy: comparisons, applications, and problems. *BioTechniques* **39**,6S (2005), S2–S5.

[36] K. N. Fish. Total Internal Reflection Fluorescence (TIRF) Microscopy. *Curr. Protoc. Cytom.* **50**,1 (2009), pp. 12.18.1–12.18.13.

[37] *EMCCD vs sCMOS - Cameras For Spinning Disk Confocal Microscopy*. `https://andor.oxinst.com/learning/view/article/emccd-vs-scmos-cameras-for-spinning-disk-confocal-microscopy`.

[38] H. T. Beier and B. L. Ibey. Experimental Comparison of the High-Speed Imaging Performance of an EM-CCD and sCMOS Camera in a Dynamic Live-Cell Imaging Test Case. *PLOS ONE* **9**,1 (Jan. 2014), pp. 1–6.

[39] M. G. Gustafsson et al. Three-dimensional resolution doubling in wide-field fluorescence microscopy by structured illumination. *Biophys. J.* **94**,12 (2008), pp. 4957–4970.

[40] S. W. Hell and J. Wichmann. Breaking the diffraction resolution limit by stimulated emission: stimulated-emission-depletion fluorescence microscopy. *Opt. Lett.* **19**,11 (June 1994), pp. 780–782.

[41] E. Betzig et al. Imaging Intracellular Fluorescent Proteins at Nanometer Resolution. *Science* **313**,5793 (2006), pp. 1642–1645.

[42] S. T. Hess, T. P. Girirajan, and M. D. Mason. Ultra-High Resolution Imaging by Fluorescence Photoactivation Localization Microscopy. *Biophys. J.* **91**,11 (2006), pp. 4258–4272.

[43] M. Heilemann et al. Subdiffraction-Resolution Fluorescence Imaging with Conventional Fluorescent Probes. *Angew. Chem. Int. Ed.* **47**,33 (2008), pp. 6172–6176.

[44] M. J. Rust, M. Bates, and X. Zhuang. Sub-diffraction-limit imaging by stochastic optical reconstruction microscopy (STORM). *Nat. Methods* **3**,10 (2006), pp. 793–796.

[45] K. I. Mortensen et al. Optimized localization analysis for single-molecule tracking and super-resolution microscopy. *Nat. Methods* **7**,5 (2010), pp. 377–381.

[46] R. E. Thompson, D. R. Larson, and W. W. Webb. Precise Nanometer Localization Analysis for Individual Fluorescent Probes. *Biophys. J.* **82**,5 (2002), pp. 2775–2783.

[47] B. Huang et al. Three-Dimensional Super-Resolution Imaging by Stochastic Optical Reconstruction Microscopy. *Science* **319**,5864 (2008), pp. 810–813.

[48] S. R. P. Pavani et al. Three-dimensional, single-molecule fluorescence imaging beyond the diffraction limit by using a double-helix point spread function. *Proc. Natl. Acad. Sci. U.S.A.* **106**,9 (2009), pp. 2995–2999.

[49] M. F. Juette et al. Three-dimensional sub–100 nm resolution fluorescence microscopy of thick samples. *Nat. Methods* **5**,6 (2008), pp. 527–529.

[50] T. Dertinger et al. Fast, background-free, 3D super-resolution optical fluctuation imaging (SOFI). *Proc. Natl. Acad. Sci. U.S.A.* **106**,52 (2009), pp. 22287–22292.

[51] S. Geissbuehler et al. Mapping molecular statistics with balanced super-resolution optical fluctuation imaging (bSOFI). *Opt. Nanoscopy* **1**,1 (2012), pp. 1–7.

[52] F. Balzarotti et al. Nanometer resolution imaging and tracking of fluorescent molecules with minimal photon fluxes. *Science* **355**,6325 (2017), pp. 606–612.

[53] M. Weber et al. MINSTED fluorescence localization and nanoscopy. *Nat. Photonics* (2021), pp. 1–6.

[54] J. Engelhardt et al. Molecular Orientation Affects Localization Accuracy in Superresolution Far-Field Fluorescence Microscopy. *Nano Lett.* **11**,1 (2011), pp. 209–213.

[55] M. D. Lew, M. P. Backlund, and W. E. Moerner. Rotational Mobility of Single Molecules Affects Localization Accuracy in Super-Resolution Fluorescence Microscopy. *Nano Lett.* **13**,9 (2013), pp. 3967–3972.

[56] D. T. Gillespie. *Markov processes: an introduction for physical scientists*. Elsevier, 1991.

[57] M. Kuno et al. Nonexponential "blinking" kinetics of single CdSe quantum dots: A universal power law behavior. *J. Chem. Phys.* **112**,7 (2000), pp. 3117–3120.

[58] K. T. Shimizu et al. Blinking statistics in single semiconductor nanocrystal quantum dots. *Phys. Rev. B* **63**, (20 May 2001), p. 205316.

[59] P. J. Brockwell and R. A. Davis. Estimation of the Mean and the Autocovariance Function. In: *Time Series: Theory and Methods*. New York, NY: Springer New York, 1991, pp. 218–237.

[60] J. Cooley, P. Lewis, and P. Welch. The finite Fourier transform. *IEEE Transactions on Audio and Electroacoustics* **17**,2 (1969), pp. 77–85.

[61] D. G. Lampard. Generalization of the Wiener-Khintchine Theorem to Nonstationary Processes. *J. Appl. Phys.* **25**,6 (1954), pp. 802–803.

[62] D. T. Gillespie. Exact stochastic simulation of coupled chemical reactions. *J. Phys. Chem.* **81**,25 (1977), pp. 2340–2361.

[63] P. J. Shaw. Comparison of Widefield/Deconvolution and Confocal Microscopy for Three-Dimensional Imaging. In: *Handbook Of Biological Confocal Microscopy*. Ed. by J. B. Pawley. Boston, MA: Springer US, 2006, pp. 453–467.

[64] E. E. Diel, J. W. Lichtman, and D. S. Richardson. Tutorial: avoiding and correcting sample-induced spherical aberration artifacts in 3D fluorescence microscopy. *Nat. Protoc.* **15**,9 (2020), pp. 2773–2784.

[65] I. Khaw et al. Flat-field illumination for quantitative fluorescence imaging. *Opt. Express* **26**,12 (June 2018), pp. 15276–15288.

[66] M. Hirsch et al. A Stochastic Model for Electron Multiplication Charge-Coupled Devices – From Theory to Practice. *PLOS ONE* **8**,1 (Jan. 2013), pp. 1–13.

[67] J. Widengren, U. Mets, and R. Rigler. Fluorescence correlation spectroscopy of triplet states in solution: a theoretical and experimental study. *J. Phys. Chem.* **99**,36 (1995), pp. 13368–13379.

[68] R. Rigler et al. Fluorescence correlation spectroscopy with high count rate and low background: analysis of translational diffusion. *Eur. Biophys. J.* **22**,3 (1993), pp. 169–175.

[69] M. Weissman, H. Schindler, and G. Feher. Determination of molecular weights by fluctuation spectroscopy: application to DNA. *Proc. Natl. Acad. Sci. U.S.A.* **73**,8 (1976), pp. 2776–2780.

[70] S. Saffarian and E. L. Elson. Statistical analysis of fluorescence correlation spectroscopy: the standard deviation and bias. *Biophys. J.* **84**,3 (2003), pp. 2030–2042.

[71] S. Sehayek. Refinements and extensions of correlation techniques applied to fluorescence microscopy. MA thesis. McGill University, 2016.

[72] B. Hebert, S. Costantino, and P. W. Wiseman. Spatiotemporal image correlation spectroscopy (STICS) theory, verification, and application to protein velocity mapping in living CHO cells. *Biophys. J.* **88**,5 (2005), pp. 3601–3614.

[73] D. L. Kolin, D. Ronis, and P. W. Wiseman. k-Space Image Correlation Spectroscopy: A Method for Accurate Transport Measurements Independent of Fluorophore Photophysics. *Biophys. J.* **91**,8 (2006), pp. 3061–3075.

[74] S. Semrau and T. Schmidt. Particle Image Correlation Spectroscopy (PICS): Retrieving Nanometer-Scale Correlations from High-Density Single-Molecule Position Data. *Biophys. J.* **92**,2 (2007), pp. 613–621.

[75] M. A. Digman et al. Measuring Fast Dynamics in Solutions and Cells with a Laser Scanning Microscope. *Biophys. J.* **89**,2 (2005), pp. 1317–1327.

[76] I. Gregor, D. Patra, and J. Enderlein. Optical Saturation in Fluorescence Correlation Spectroscopy under Continuous-Wave and Pulsed Excitation. *ChemPhysChem* **6**,1 (2005), pp. 164–170.

[77] B. Berne and R. Pecora. Dynamic Light Scattering: With Applications to Chemistry, Biology, and Physics. In: Dover Books on Physics Series. Dover Publications, 2000. Chap. 5.8.

[78] N. Durisic et al. Detection and Correction of Blinking Bias in Image Correlation Transport Measurements of Quantum Dot Tagged Macromolecules. *Biophys. J.* **93**,4 (2007), pp. 1338–1346.

[79] S. F. Gibson and F. Lanni. Experimental test of an analytical model of aberration in an oil-immersion objective lens used in three-dimensional light microscopy. *J. Opt. Soc. Am. A* **9**,1 (Jan. 1992), pp. 154–166.

[80] S. A. McKinney, C. Joo, and T. Ha. Analysis of Single-Molecule FRET Trajectories Using Hidden Markov Modeling. *Biophys. J.* **91**,5 (2006), pp. 1941–1951.

[81] C. M. Brown et al. Raster image correlation spectroscopy (RICS) for measuring fast protein dynamics and concentrations with a commercial laser scanning confocal microscope. *J. Microsc.* **229**,1 (2008), pp. 78–91.

[82] S. Manley et al. High-density mapping of single-molecule trajectories with photoactivated localization microscopy. *Nat. Methods* **5**,2 (2008), pp. 155–157.

[83] I. Sgouralis et al. A Bayesian Nonparametric Approach to Single Molecule Förster Resonance Energy Transfer. *J. Phys. Chem. B* **123**,3 (2019), pp. 675–688.

[84] S. Jazani et al. An alternative framework for fluorescence correlation spectroscopy. *Nat. Commun.* **10**,1 (2019), pp. 1–10.

[85] A. Sharonov and R. M. Hochstrasser. Wide-field subdiffraction imaging by accumulated binding of diffusing probes. *Proc. Natl. Acad. Sci. U.S.A.* **103**,50 (2006), pp. 18911–18916.

[86] R. Jungmann et al. Single-Molecule Kinetics and Super-Resolution Microscopy by Fluorescence Imaging of Transient Binding on DNA Origami. *Nano Lett.* **10**,11 (2010), pp. 4756–4761.

[87] C. Oi et al. LIVE-PAINT allows super-resolution microscopy inside living cells using reversible peptide-protein interactions. *Commun. Biol.* **3**,1 (2020), pp. 1–10.

[88] D. S. Banks and C. Fradin. Anomalous Diffusion of Proteins Due to Molecular Crowding. *Biophys. J.* **89**,5 (2005), pp. 2960–2971.

[89] B. Berne and R. Pecora. Dynamic Light Scattering: With Applications to Chemistry, Biology, and Physics. In: Dover Books on Physics Series. Dover Publications, 2000. Chap. 5.4.

[90] I. Blikstad and L. Carlsson. On the dynamics of the microfilament system in HeLa cells. *J. Cell Biol.* **93**,1 (Apr. 1982), pp. 122–128.

[91] S. Boyle et al. Quantum Dot Fluorescence Characterizes the Nanoscale Organization of T Cell Receptors for Antigen. *Biophys. J.* **101**,11 (2011), pp. L57–L59.

[92] H. B. Brandão et al. Measuring ligand–receptor binding kinetics and dynamics using k-space image correlation spectroscopy. *Methods* **66**,2 (2014), pp. 273–282.

[93] S. Bretschneider, C. Eggeling, and S. W. Hell. Breaking the Diffraction Barrier in Fluorescence Microscopy by Optical Shelving. *Phys. Rev. Lett.* **98**, (21 May 2007), p. 218103.

[94] C. Chatfield. *The analysis of time series: an introduction*. 6th. Florida, US: CRC Press, 2004.

[95] R. A. Colyer et al. High-throughput FCS using an LCOS spatial light modulator and an 8 × 1 SPAD array. *Biomed. Opt. Express* **1**,5 (Dec. 2010), pp. 1408–1431.

[96] E. M. Conroy et al. Self-Quenching, Dimerization, and Homo-FRET in Hetero-FRET Assemblies with Quantum Dot Donors and Multiple Dye Acceptors. *J. Phys. Chem. C* **120**,31 (2016), pp. 17817–17828.

[97] G. Cosa et al. Secondary Structure and Secondary Structure Dynamics of DNA Hairpins Complexed with HIV-1 NC Protein. *Biophys. J.* **87**,4 (2004), pp. 2759–2767.

[98] G. T. Dempsey et al. Evaluation of fluorophores for optimal performance in localization-based super-resolution imaging. *Nat. Methods* **8**,12 (2011), p. 1027.

[99] R. M. Dickson et al. On/off blinking and switching behaviour of single molecules of green fluorescent protein. *Nature* **388**,6640 (1997), p. 355.

[100] M. A. Digman et al. Mapping the Number of Molecules and Brightness in the Laser Scanning Microscope. *Biophys. J.* **94**,6 (2008), pp. 2320–2332.

[101] G. Donnert, C. Eggeling, and S. W. Hell. Major signal increase in fluorescence microscopy through dark-state relaxation. *Nat. Methods* **4**,1 (2007), pp. 81–86.

[102] S. Doose et al. Comparison of Photophysical and Colloidal Properties of Biocompatible Semiconductor Nanocrystals Using Fluorescence Correlation Spectroscopy. *Anal. Chem.* **77**,7 (2005), pp. 2235–2242.

[103] L. Kisley et al. Characterization of Porous Materials by Fluorescence Correlation Spectroscopy Super-resolution Optical Fluctuation Imaging. *ACS Nano* **9**,9 (2015), pp. 9158–9166.

[104] A. Gasilina et al. The ArfGAP ASAP1 Controls Actin Stress Fiber Organization via Its N-BAR Domain. *iScience* **22**, (2019), pp. 166–180.

[105] Y. Gidi et al. Efficient One-Step PEG-Silane Passivation of Glass Surfaces for Single-Molecule Fluorescence Studies. *ACS Appl. Mater. Interfaces* **10**,46 (2018), pp. 39505–39511.

[106] V. Glembockyte, R. Lincoln, and G. Cosa. Cy3 Photoprotection Mediated by Ni2+ for Extended Single-Molecule Imaging: Old Tricks for New Techniques. *J. Am. Chem. Soc.* **137**,3 (2015), pp. 1116–1122.

[107] V. Glembockyte, J. Lin, and G. Cosa. Improving the Photostability of Red- and Green-Emissive Single-Molecule Fluorophores via Ni2+ Mediated Excited Triplet-State Quenching. *J. Phys. Chem. B* **120**,46 (2016), pp. 11923–11929.

[108] M. Haase et al. Exponential and Power-Law Kinetics in Single-Molecule Fluorescence Intermittency. *J. Phys. Chem. B* **108**,29 (2004), pp. 10445–10450.

[109] S. Habuchi et al. Reversible single-molecule photoswitching in the GFP-like fluorescent protein Dronpa. *Proc. Natl. Acad. Sci. U.S.A.* **102**,27 (2005), pp. 9511–9516.

[110] R. Hoebe et al. Controlled light-exposure microscopy reduces photobleaching and phototoxicity in fluorescence live-cell imaging. *Nat. Biotechnol.* **25**,2 (2007), pp. 249–253.

[111] J. Houel et al. Autocorrelation Analysis for the Unbiased Determination of Power-Law Exponents in Single-Quantum-Dot Blinking. *ACS Nano* **9**,1 (2015), pp. 886–893.

[112] B. Kannan et al. Electron multiplying charge-coupled device camera based fluorescence correlation spectroscopy. *Anal. Chem.* **78**,10 (2006), pp. 3444–3451.

[113] T. Kiuchi et al. Measurements of spatiotemporal changes in G-actin concentration reveal its effect on stimulus-induced actin assembly and lamellipodium extension. *J. Cell Biol.* **193**,2 (2011), pp. 365–380.

[114] H. D. Kim et al. Mg2+-dependent conformational change of RNA studied by fluorescence correlation and FRET on immobilized single molecules. *Proc. Natl. Acad. Sci. U.S.A.* **99**,7 (2002), pp. 4284–4289.

[115] D. L. Kolin, S. Costantino, and P. W. Wiseman. Sampling effects, noise, and photobleaching in temporal image correlation spectroscopy. *Biophys. J.* **90**,2 (2006), pp. 628–639.

[116] J. W. Krieger et al. Imaging fluorescence (cross-) correlation spectroscopy in live cells and organisms. *Nature Protoc.* **10**,12 (2015), pp. 1948–1974.

[117] R. Luchowski et al. Single molecule studies of multiple-fluorophore labeled antibodies. Effect of homo-FRET on the number of photons available before photobleaching. *Curr. Pharm. Biotechnol.* **9**,5 (2008), pp. 411–420.

[118] B. Mandracchia et al. Fast and accurate sCMOS noise correction for fluorescence microscopy. *Nat. Commun.* **11**,1 (2020), pp. 1–12.

[119] D. McDonald et al. Nucleoplasmic β-actin exists in a dynamic equilibrium between low-mobility polymeric species and rapidly diffusing populations. *J. Cell. Biol.* **172**,4 (2006), pp. 541–552.

[120] J. McGrath et al. Simultaneous Measurements of Actin Filament Turnover, Filament Fraction, and Monomer Diffusion in Endothelial Cells. *Biophys. J.* **75**,4 (1998), pp. 2070–2078.

[121] P. P. Mondal, R. J. Gilbert, and P. T. C. So. Photobleaching reduced fluorescence correlation spectroscopy. *Appl. Phys. Lett.* **97**,10 (2010), p. 103704.

[122] J. Mücksch et al. Quantifying Reversible Surface Binding via Surface-Integrated Fluorescence Correlation Spectroscopy. *Nano Lett.* **18**,5 (2018), pp. 3185–3192.

[123] R. P. Nieuwenhuizen et al. Measuring image resolution in optical nanoscopy. *Nature methods* **10**,6 (2013), pp. 557–562.

[124] I. L. Novak, B. M. Slepchenko, and A. Mogilner. Quantitative analysis of G-actin transport in motile cells. *Biophys. J.* **95**,4 (2008), pp. 1627–1638.

[125] R. Schmidt et al. MINFLUX nanometer-scale 3D imaging and microsecond-range tracking on a common fluorescence microscope. *Nat. Commun.* **12**,1 (2021), pp. 1–12.

[126] P. Sengupta et al. Measuring Size Distribution in Highly Heterogeneous Systems with Fluorescence Correlation Spectroscopy. *Biophys. J.* **84**,3 (2003), pp. 1977–1984.

[127] A. P. Singh et al. The performance of 2D array detectors for light sheet based fluorescence correlation spectroscopy. *Opt. Express* **21**,7 (Apr. 2013), pp. 8652–8668.

[128] L. Song et al. Photobleaching kinetics of fluorescein in quantitative fluorescence microscopy. *Biophys. J.* **68**,6 (1995), pp. 2588–2600.

[129] C. Eggeling et al. Direct observation of the nanoscale dynamics of membrane lipids in a living cell. *Nature* **457**,7233 (2009), pp. 1159–1162.

[130] P. N. Hedde et al. Stimulated emission depletion-based raster image correlation spectroscopy reveals biomolecular dynamics in live cells. *Nat. Commun.* **4**,1 (2013), pp. 1–8.

[131] A. Honigmann et al. Scanning STED-FCS reveals spatiotemporal heterogeneity of lipid interaction in the plasma membrane of living cells. *Nat. Commun.* **5**,1 (2014), pp. 1–12.

[132] W. Wang et al. Super Temporal-Resolved Microscopy (STReM). *J. Phys. Chem. Lett.* **7**,22 (2016), pp. 4524–4529.

[133] K. Tsekouras et al. Inferring diffusion dynamics from FCS in heterogeneous nuclear environments. *Biophys. J.* **109**,1 (2015), pp. 7–17.

[134] M. Wachsmuth, W. Waldeck, and J. Langowski. Anomalous diffusion of fluorescent probes inside living cell nuclei investigated by spatially-resolved fluorescence correlation spectroscopy. *J. Mol. Biol.* **298**,4 (2000), pp. 677–689.

[135] M. Weiss et al. Anomalous Subdiffusion Is a Measure for Cytoplasmic Crowding in Living Cells. *Biophys. J.* **87**,5 (2004), pp. 3518–3524.

[136] M. Weiss, H. Hashimoto, and T. Nilsson. Anomalous Protein Diffusion in Living Cells as Seen by Fluorescence Correlation Spectroscopy. *Biophys. J.* **84**,6 (2003), pp. 4043–4052.

[137] J. Widengren and R. Rigler. Mechanisms of photobleaching investigated by fluorescence correlation spectroscopy. *Bioimaging* **4**,3 (1996), pp. 149–157.

[138] E. K. L. Yeow et al. Characterizing the Fluorescence Intermittency and Photobleaching Kinetics of Dye Molecules Immobilized on a Glass Surface. *J. Phys. Chem. A* **110**,5 (2006), pp. 1726–1734.

[139] X. Yi et al. Moments reconstruction and local dynamic range compression of high order superresolution optical fluctuation imaging. *Biomed. Opt. Express* **10**,5 (May 2019), pp. 2430–2445.

[140] W.-T. Yip et al. Classifying the Photophysical Dynamics of Single- and Multiple-Chromophoric Molecules by Single Molecule Spectroscopy. *J. Phys. Chem. A* **102**,39 (1998), pp. 7564–7575.

[141] X. Yi. Super resolution of Optical Fluctuation Imaging 2.0 (SOFI-2.0): Towards fast super resolved imaging of live cells. PhD thesis. UCLA, 2017.

[142] D. Zicha et al. Rapid Actin Transport During Cell Protrusion. *Science* **300**,5616 (2003), pp. 142–145.